Draft version January 8, 2024
Preprint typeset using LaTeX style emulateapj v. 12/16/11

THE SLUMPED MICROPORE OPTIC VADE MECUM

K. D. Kuntz[1]

Draft version January 8, 2024

ABSTRACT

This **draft** work summarizes the mathematical basis for the current slumped micropore optic (SMPO) simulator. In the process it covers most of the fundamental ideas and equations. It also contains some discussion of the implication of the SMPO mathematics upon instrument design. This document gathers together some of the useful input data as well. While SMPO are used to observe objects at infinity, they are tested with sources not at infinity (a beam line) or with the source behind the optic (the test stand). We derive the mathematics for these test configurations and sketch some of the data reduction needed to derive the parameters of the optics. Many of the SMPO applications considered thus far require sunshades with interior baffles. We consider the interaction of these baffles with the optic and the constraints they place on the instrument design.

1. TECHNICAL

Because this document is an active working document, containing the latest work on simulating and characterization, it is subject to frequent changes, some trivial, some significant. We will attempt to record the significant changes in the following change log, but small changes will not. The date of this document is given above automatically by LaTeX, and is the only version number for this work.

1.1. *Change Log*

12/11/23: Added text and figures under 2.0.

01/10/23: Began construction of the section describing the use of the test stand.

26/09/23: Corrected typo and added material to the Willingale approximation of a reverse beamline with post mask.

31/01/23: Added "Future" section to remind the author of things that remain to be done.

01/01/23: Introduced the Technical section to allow better document tracking.

1.2. *Future*

History: Need followup on round pore attempts.

Shades: Need to work shade design mathematics in.

Coatings: Requires reflectivity at Lyα to be done correctly.

Roughness: Need to understand various approximations and(?) compare.

Taper: Need to implement a reasonable model of tapered pores.

Wine Crate Optics: For M. Galeazzi.

True PSF Width: Start from Willingale.

Test Stand: Do full up model for off-center mask, for tilted optic, and for off-center optic. Expand simulation to calculate the effect of extended source spot both for central spot and for peripheral spots. This section probably requires further work with the test stand. For the next test stand run, should do a closely spaced run of Z_S with a fixed X_M to determine best throughput and to better constrain spot size.

Stand Mathematics: Calculate the trade-off between reflectivity at $\beta - \alpha$ and the reflected fraction. Reconstruct Figure 52.

[1] The Henry A. Rowland Department of Physics and Astronomy, Johns Hopkins University, 3701 San Martin Drive, Baltimore, MD, 21218; kuntz@pha.jhu.edu

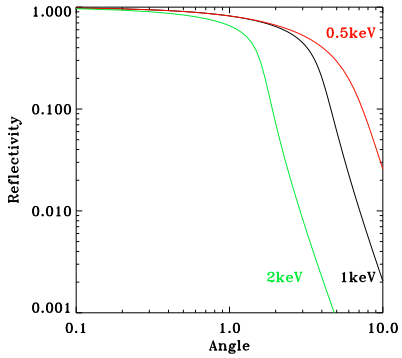

Figure 1. The reflectivity as a function of angle between the ray and the surface, for three different energies of X-rays and an Iridium surface. Note that reflectivity decreases as either the energy or angle increases.

2. INTRODUCTION

X-ray mirrors are based on grazing incidence reflections because reflectivity decreases rapidly as the angle between the ray and the surface increases, as shown in Figure 1. Traditional optics (Wolter type I) rely on a reflection from the interior of a hyperboloid of revolution followed by a reflection from the interior of a paraboloid of revolution. The two successive reflections are required in order to reduce the focal length of the optic and to reduce the coma that would be produced if there were only a single reflection. In order to build a real optic, we use a slice of the hyperboloid of revolution made perpendicular to its axis, and a slice of the paraboloid of revolution, also made perpendicular to its axis. Each mirror is a shell with a particular curvature on its inner surface. In order to increase the collecting area, we replace both the hyperboloid section and the paraboloid section with a series of nested hyperboloids (or paraboloids) where the curvature of each ring is a function of the radius of the ring. Traditionally, the spacing of the rings is such that rays reflecting from the interior of one ring will not intersect the back of the next smaller ring. As a result of this nesting, the acceptance angle is rather small, and one must be very clever to achieve a field of view (FOV) as large as a degree; most Wolter type 1 optics have much smaller FOV.

Slumped, square-pore, micro-pore optics, generally known just as SMPO or MPO are optics that sacrifice angular resolution in order to achieve a large FOV; the STORM design is for $\sim 25^\circ \times 25^\circ$, while transient telescopes aim for FOVs on the order of 5000 square degrees ($\sim \frac{1}{8}^{th}$ of the sky.) The following document aims to explore the capabilities and limitations of these optics.

2.1. *How the SMPO Work*

As shown in Figure 3, an array of flat mirrors placed perpendicular to a cylinder can focus light in one dimension. If the mirrors are perpendicular to the surface of a sphere, and a second array is placed perpendicular to both the first array and the surface of the sphere, then one can focus light in two dimensions, which allows imaging. There are a number of ways to arrange the reflectors, as shown in Figure 4. The most easily constructed manifestation of these two arrays of mirrors is to create a microchannel plate with square pores, where the interior of the pores become mirrors, and to slump that microchannel plate over a spherical surface. The result is a slumped micropore optic (SMPO, sometimes SMO).

The SMPOs to be considered here have square pores that are square-packed. This is not the optimal packing for an X-ray optic, but it is what is currently technically feasible. The SMPO is manufactured as a flat microchannel plate, and slumped over a spherical mandrel or mould[2]. In the process the individual pores are deformed from square. However, for the bulk of this work, they will be assumed to be square and aligned with the overall x-y cartesian geometry of the device.

Each pore has a width W and is divided from another by walls of thickness T, so the pitch P is $W+T$. The length of the pores is the thickness of the optic, which is L. The radius of curvature (which is assumed here to refer to the underside of the optic) is R_c. Given that the pores are square, there is a strong xy geometry imposed upon the problem. In many cases, problems are separable into the x and y dimensions. The z axis is taken to be the optical axis, with the origin at the center of curvature.

Since the SMPO is a section of a sphere, any location on the facet *can* be taken as the optical axis. This property makes many problems easy. However, it can engender a great deal of confusion. In the following work I have tried to be consistent. The **instrument axis** is through the center of the optic to the radius of curvature. A **facet axis** is through the center of a facet to the radius of curvature. The **optical axis** is through some defined point and the radius of curvature. It is sometimes useful to define the **source axis** as the vector from the radius of curvature, through the optic, in the direction of a source.

There are two ways in which SMPO are different from the nested shell mirrors used by traditional X-ray optics. First, with a few exceptions, neither the x-axis nor the y-axis of the pore is aligned to the local radius. Therefore an incident ray can not be focussed with a single reflection (again with a few exceptions). Instead, there must be a single reflection in both the x plane and in the y plane in order for the incident ray to be focussed. This concept is somewhat demonstrated in Figure 5. Second, for a traditional X-ray optic with nested mirror shells, any two adjacent mirror shells are sufficiently far apart that any ray reflecting from the inner surface of the outer shell will not intersect the outer surface of the inner shell. For a SMPO, opposite walls of the pore function as our nested mirrors. There are many incidence angles for which a ray will reflect from both of two opposing walls, and a very limited range of incidence angles for which a ray will *not* reflect from *both* of the opposing walls. Rays which are reflected from opposing walls are usually not focussed. A third difference is that traditional X-ray optics require two reflections in the same plane in order to focus without spherical aberration. Slumped micropore optics are subject to spherical aberration.

These two concepts make the SMPO focussing seem rather complicated, and it is to be admitted that the way the SMPO focusses is not entirely intuitive. In the following sections we will use a special case, where the

[2] Technically, a mandrel is cylindrical, so this is probably a mould, though Photonis seems to refer to it as a mandrel.

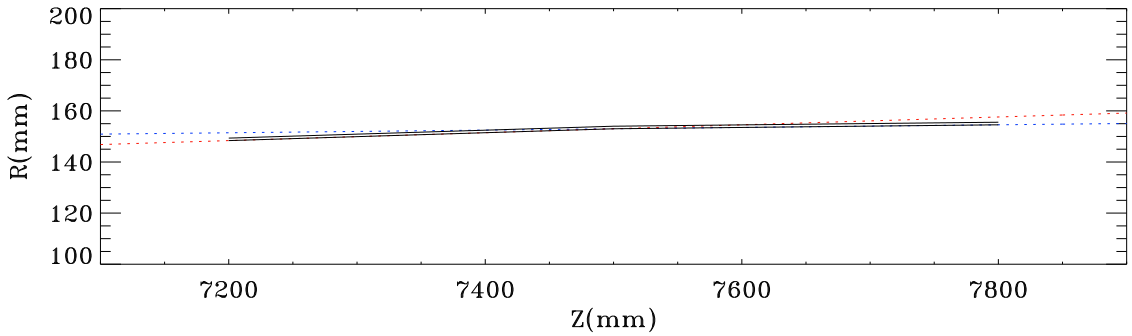

Figure 2. Wolter type 1 optics, demonstrating the nested shells, and how they restrict the angle from which photons can be accepted. This example shows the two innermost shells of an *XMM-Newton* mirror, where each shell is 600 mm long, and the shells are separated by 1 mm. The acceptance angle is $\sim 11'$. The dashed red line shows the hyperboloid of the inner shell while the dashed blue line shows the paraboloid of the inner shell. Note that the scale in the R direction is expanded by a factor of 2 in order to show the separation of the two shells.

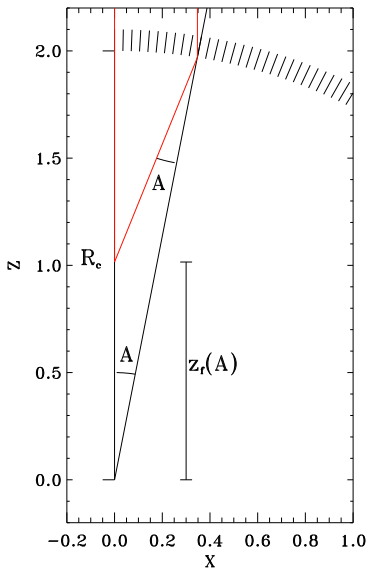

Figure 3. The fundamental geometric construction for the optic. The vertical line to the left is the optical axis. The series of short radial lines represents individual reflectors. The *red* lines are an incident rays parallel to the optical axis. The vertical bar represents the distance above the center of curvature at which the off-axis ray intersects the optical axis.

x axis of the pore is aligned with the radial vector (the vector from the instrument axis to the pore), to calculate where the focus is and how large an optic can actually focus rays parallel to the instrument axis. *Luckily,* the focussing problem is separable, so once one understands how focussing is accomplished in one dimension, the extension to two dimensions is obvious.

2.2. *The Shape of the PSF*

Figure 6 shows the point spread function as a function of the total number of reflections, that is, the total number of reflections in both the x and y dimensions. The first panel is the distribution of rays that pass through the optic undeviated. The second panel is the distribution of rays that experience a single reflection, that is, those that are focussed in one dimension but not the other. The third panel is the distribution of rays that experience two reflections. Note that this could be a reflection in x and a reflection in y, producing the (hard to see) spot in the middle, or no reflections in one dimension and two reflections in the other, producing the large square regions. Further odd numbers of reflections produce crosses while further even numbers of reflections produce arrays of square regions that are further and further from the instrument axis.

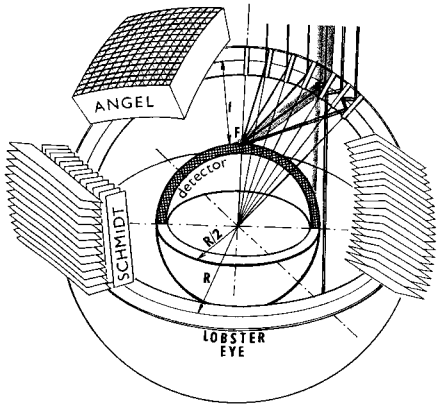

Figure 4. Demonstration of two different ways to use flat reflectors to focus X-rays. The "Angel" configuration is, essentially, the SMPO. This figure is widely found on the internet, but I have not yet tracked down its source.

The overall PSF has a very sharp core, containing $\sim$ 25% of the flux (depending upon energy). The two perpendicular arms, due to rays focused in one direction but not the other, contains $\sim$ 50% of the flux. Then there is a relatively smooth diffuse background[3] that contains $\sim$ 25%. The ratio of the core to the total throughput is referred to as the *contrast.* [OK, I may be the only one who does, but it works.] However, it should be noted that core:arm:diffuse ratio is a strong function of the reflectivity as a function of energy and the incidence angle, and thus is a strong function of the pore W/L ratio.

As can be seen in Figures 6 and 7, the PSF of the idealized devices that we simulate has a very sharp core. The fraction of the flux in the core depends upon the energy. The true core flux will also depend upon the resolution

[3] There is a broad variation in the term used for this component. Some use the term "background", but this leads to confusion with the *background* of the source of interest. I prefer the term "unfocussed" or "unfocussed component".

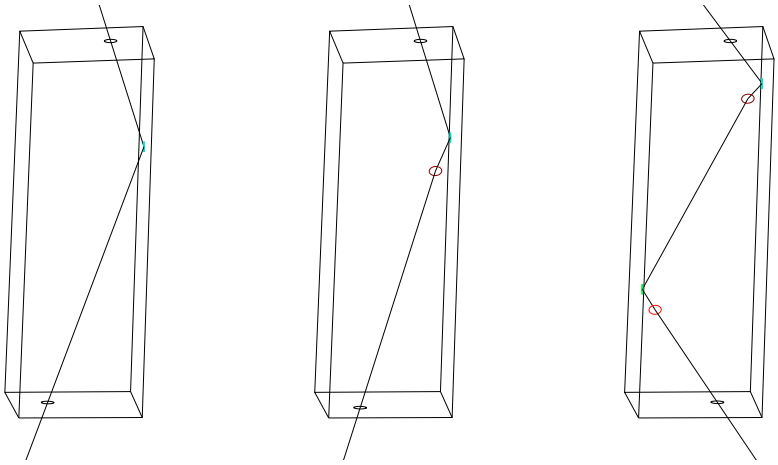

Figure 5. Possible paths for a ray passing through a pore. The pore to the left focusses the ray, while the pore to the right causes the ray to continue in the direction of incidence, but offset.

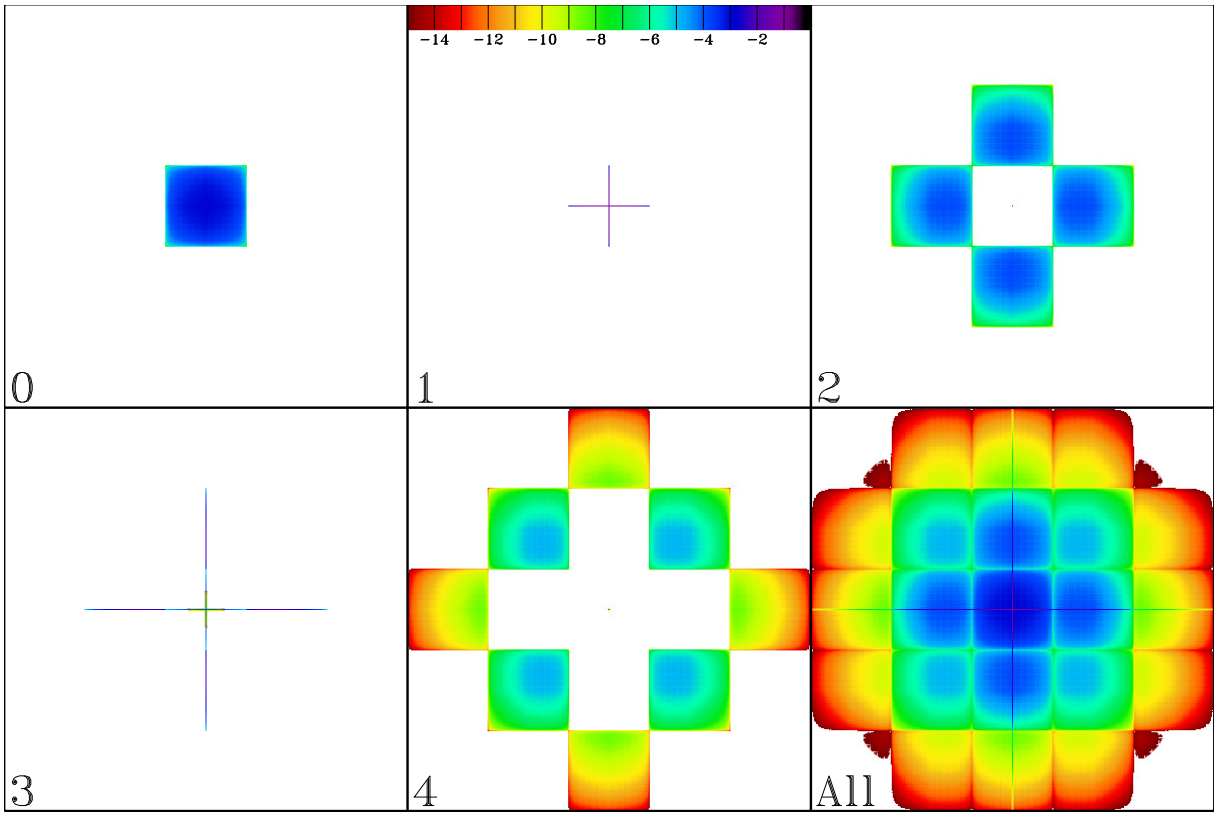

Figure 6. The PSF as a function of the number of reflections. The PSF has been normalized to unity at the center. The color scale is logarithmic. The size of the "squares" is set by the radius of curvature of the device, not the size of the device.

at which one is sampling the PSF. In the bulk of the simulations done for this work, the PSF was sampled at a resolution of 0.5 mm on the detector plane, as this is the typical resolution of an MCP detector. CCD resolution, of course, would be even finer. However, due to photon starvation, the effective resolution sought is $\sim 0.25°$. Because the core sits on a broader peak, the fraction of flux falling in the central pixel of the PSF is somewhat higher than that truly in the core. This should be kept in mind when considering the contrast of different optics.

2.3. *Instruments*

Attempting to design instruments with very large apertures/very wide fields of view using SMPO brings one face to face with reality. Individual SMPO, which we refer to as "facets", are relatively small, typically 4 cm by 4 cm. Thus the spherical optic must be constructed as a mosaic of square facets, which requires a framework to support them. That framework reduces the effective area of the instrument, and can introduce a number of errors that degrade the PSF. Even the individual facets have issues, such as surface roughness, that reduce their effective area and increase the size of their PSFs. To understand the relative importance of these different issues, we will be considering a number of notional instrument

Table 1
Instrument Parameters

Parameter	Symbol	STORM	SMILE	CuPID	LEXI	Miami
			Measurements			
Pore width	W	20 μm	40 μm	20 μm	20 μm	20 μm
Pitch	P	26 μm	52 μm	26 μm	26 μm	26 μm
Pore length	L	1 mm	1.2 mm	1mm	1 mm	1 mm
Radius of curvature	R_c	100 cm	60 cm	55 cm	75 cm	100 cm
Facet Size	F	4 cm× 4 cm	4 cm	4 cm	4 cm	4 cm
Number of Facets	N^2	100	2×16	1	9	4
			Derived Parameters			
Open Fraction		60%	60%	60%	60%	60%
W/L		0.02	0.033	0.02	0.02	0.02
Focal Length	z_f	50 cm	30 cm	27.5 cm	37.5 cm	50 cm
FOV	Max(Γ)	$\sim 11.5°$	$15.6° \times 31.2°$?	$\sim 4.1°$	$\sim 9.2°$	$\sim 4.6°$
0 Reflection Limit	Γ_0	1.14°	1.91°			
1 Reflection Limit	Γ_1	2.29°	3.81°			
2 Reflection Limit	Γ_2	3.43°	5.71°			

[a] Measured along the spherical surface of the optic.

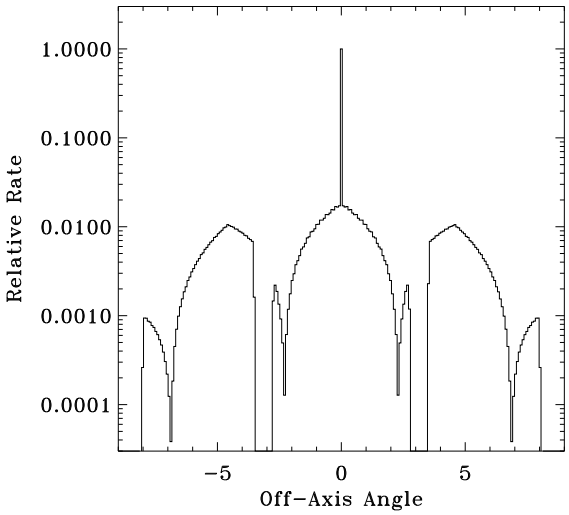

Figure 7. A cross-section of the PSF for an unbaffled 3 by 3 device. Note that the scale is logarithmic. The places where the relative rate is zero are locations of the facet support structure; the very narrow minima are due to behavior of the optic itself. The spacing of the narrow minima is set by the radius of curvature of the facets.

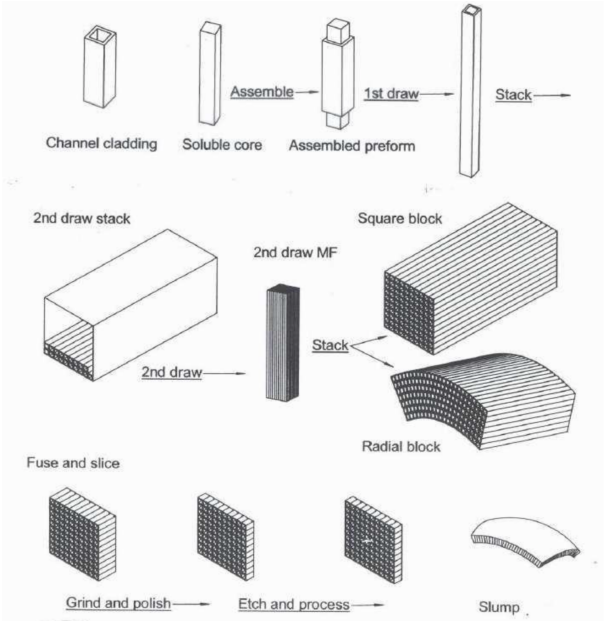

Figure 8. Partial figure taken from Mutz et al. (2007) demonstrating the manufacturing process of SMPO at Photonis. We are currently concerned only with square blocks.

designs that are listed in Table 1.

Throughout this work we will use the notional *STORM* and *LEXI* designs to demonstrate the typical magnitude of the optical distortions. The facets for these instruments are representative of the types of SMPO that can be obtained from Photonis®. As of this writing, typically available pore sizes range from 20 μm to 40 μm (see the trade study in §11.1), and radii of curvature range from 55 cm to 100 cm. The standard size is 4 cm by 4 cm, and although some discussion of making larger facets has occurred (as a result of the discussion in §11.3), it is not clear that larger facets are technically feasible for the standard manufacturing process.

2.4. *Manufacturing*

A few notes about the manufacturing process (shown schematically in Figure 8) are necessary to understand many of the issues that we will be discussing in the sections below.

Manufacturing begins with a precisely machined square tube of high index of refraction glass. This tube is something like 7 to 10 cm in diameter. Within this tube is tightly fitted a square core of soft glass that can be dissolved by acid. This tube and core assembly is then put in a furnace and drawn down to a fiber ~ 1 mm in diameter. This fiber has the same ratio of hard wall to soft core as the original assembly[4]. The fiber is cut

[4] Since all square-pore MCPs made by Photonis start with the same tube-core assembly, the wall to opening ratio, T/W is the same (so far) no matter the pore size. This may change in the future.

into uniform lengths and stacked into "multifiber bundles" of 35 by 35 fibers. The multifiber bundle is, in its turn, drawn down to a diameter of ~ 1 mm, and cut into lengths. The drawn multifibers are then stacked to form a 4 cm by 4 cm block, which is heated under pressure to make it a solid block. This block is then sliced, setting the pore length, and then polished. Each slice is then bathed in running acid for an extended period of time to remove the core glass. Finally, each slice is placed in an oven in a precisely machined concave spherical mold and, during heating, a convex spherical mold is slowly lowered onto it to force the SMPO into a spherical shell with a particular radius of curvature.

In this process there are a number of uncertainties, and there are a number of places at which defects can be introduced. It would seem that the stacking is a very delicate process, and that there are ways for individual fibers (or multifiber bundles) to become misaligned within the stack. Willingale worked on methods for determining the amount of misalignment, but that work has not been published to my knowledge. Within the final block, the interfaces between multifiber bundles typically results in some fraction of distorted pores (see Figure 9) which results in clear segmentation of the arms of the PSF.

Another potential issue is the smoothness and cleanliness of the pores. The drawing process is *expected* to produce very smooth pore walls, but we do not yet have measurements of the remaining roughness. This uncertainty enters the simulation mostly through an uncertainty in the reflectivity. Similarly, the acid washing is supposed to remove all of the core glass, but we do not know that this is truly the case; there is some suggestion from the chemistry that we might have difficulties with relict soft glass.

Finally, what actually happens during the slumping process is poorly understood, though it is clear that the shapes of the pores, particularly those near the diagonal, are deformed. The Leicester group's approach (Willingale et al. 2016) to this problem is rather different from that discussed below (§4.4). It is also clear that the slumping process is not altogether successful, as the final SMPOs can show complex deviations from spherical. Many SMPO show astigmatism, suggesting that the curvature in one direction is not quite the same as the curvature in the other. These deviations produce some of the effects described in §4.1.

2.5. *History*

SMPO were first proposed by Angel (1979) in a paper that referenced the work of the biologists Vogt (1975) and Land (1978) who had only recently realized that crustacean eyes work on the same principle, as suggested by Figure 10. Angel's contribution was not particularly welcome in a time when attention was turning from all sky surveys to high resolution investigations of individual objects (see "exchange" between Angel and Gorenstein in Hartline (1980)). Interestingly, the Schmidt configuration of flat plates (Schmidt 1975, 1981) precedes Angel's work, though Angel seems to have been unaware of it.

The first papers discussing the performance of SMPO devices appear in the late eighties/early nineties and were the product of Chapman at the University of Melbourne and Fraser at the University of Leicester. (Indeed, much of this document is encompassed in Chapman et al. (1991), though that source was not found until the Vade Mecum was nearly finished.) There was an exploration of different means of creating square pore optics (which is still an active question), such as etching silicon (Peele 1999), and there was even exploration of the use of round-pore micro-channel plates (Chapman et al. 1993).

Priedhorsky et al. (1996) seems to have been the first to propose an all-sky monitor using lobster-eye optics, though that idea was certainly in the air; I remember Nick White proposing something similar when I was first at GSFC. It would be interesting to see how many design iterations there are between Priedhorsky's and the recent MidEx round with Gamow (White!) and SIBEX.

More history here as I figure it out.

2.6. *Roadmap*

This work is primarily focussed on the creation of a simulator for such optics. Various aspects of the simulator have been motivated by optics testing (particularly at PANTER), while some have been motivated by pure curiosity. Many of those side issues are included here in order to reduce the need for others to "reinvent the wheel". This inclusion has led to a rather bulky document. I have attempted to relegate details of the side-issues to the appendices, but that has not always been possible.

Section 3 contains an overview of an idealized optic of indeterminate extent. It calculates the focal length of this device, explores the issues of spherical aberration, and sets forth the tools needed to calculate the effective area. Section 4 considers "real" optics and their defects. Some of those defects are intrinsic to the structure of the optic, such as pore deformation due to slumping. There are also, of course, extrinsic defects, or those due to accident in manufacture, such as irregularities in the radius of curvature, R_c, from one part of the optic to another. This section is not (and probably never will be entirely) complete. These issues, for the most part, degrade the PSF. Some of these issues are incorporated into the simulator, others are planned to be incorporated, and yet others may be too complex to incorporate in any meaningful manner. Section 5 considers the effect of mosaicking facets to form large aperture/wide FOV instruments, and the impact of those effects on the simulator. Section 6 considers the effect of sunshades[5]. Given that SMO instruments are intended to have wide FOVs, sunshades become much more complicated, and have a significant impact on the simulator implementation. Section 7 discusses the implementation of the simulator itself.

The second major part of the *Vade Mecum* considers SMPO testing. Sections 8 and 9 discuss the GSFC test stand for characterizing individual facets. These sections are still works in progress because the test stand itself is still a work in progress.

Finally, there is a short section on instrument design considerations. This section considers both requirements to create a monolithic optic such as used by STORM and requirements for modular wide-field designs.

[5] The philosophy for designing the sunshades is provided in a different document

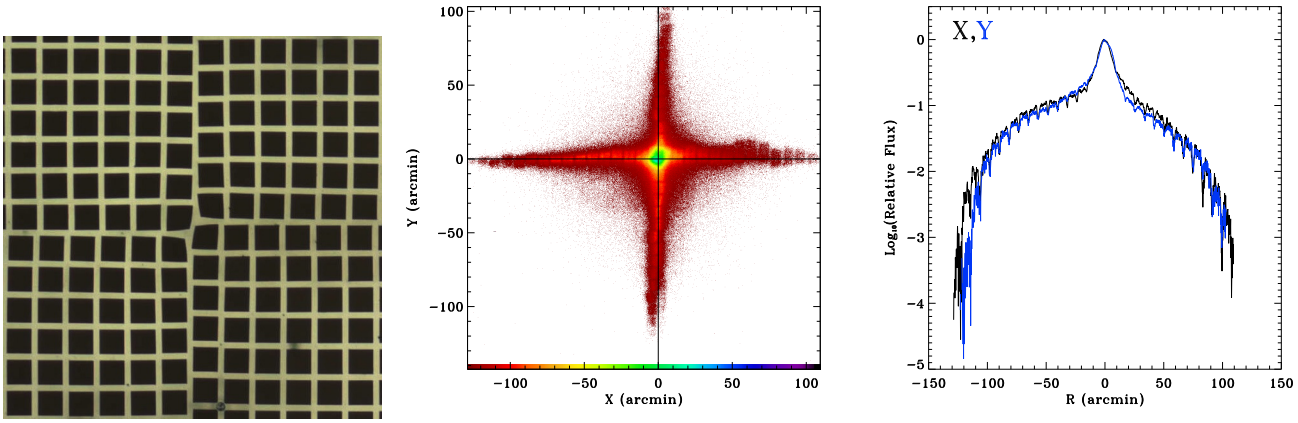

Figure 9. Left: Photomicrograph of the intersection of four micropore bundles in a finished SMPO. Photograph taken by Nick Thomas at GSFC. **Center:** The PSF of that SMPO. Image taken at PANTER. Note the periodic segmentation of the arms of the PSF which suggest the misalignment of individual multifiber bundles. **Right:** A profile of the arms showing the segmentation more clearly.

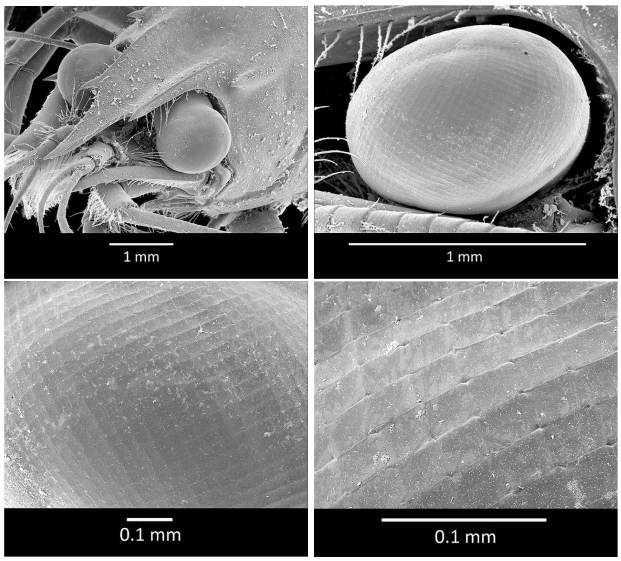

Figure 10. Photomicrographs of the eye of a lobster(?) or crayfish(?). These images were taken from a paper by Hudec et al. (2015), but I have reason to believe that the images may have been taken from an older source. Pointers to that source would be appreciated.

3. THE MATHEMATICS OF AN IDEAL SMO

This section sketches the mathematics for an *ideal* SMO, considering the focal length, the effective area, and the field of view (FOV). By ideal, we mean more than just a *perfectly manufactured* optic, we really are dealing with a somewhat *idealized* optic. We will consider less idealized optics in the following section.

3.1. *Focal Length and the Focal Surface*

3.1.1. *A First Approximation*

Figure 11 demonstrates the fundamental geometry of the micropore optic. This figure shows a cut through the optic made in the x plane of the optic. The series of short radial marks represent the pore walls a distance R_c from the origin. By construction, a ray parallel to the optical axis, striking the wall of a pore that is inclined from the optical axis by an angle A, will reflect from that surface at an angle A (just Snell's law). From the origin to the focus to the pore is an isosceles triangle, and as $A \to 0$ it can be seen that the focal length becomes $R_c/2$.

Note that, like a simple lens, a ray that strikes the optic normal to the surface of the optic will pass through the optic without deviation. Also notice that since the optic is a section of a sphere, any part of the optic can be designated the optical axis. These two rules are very useful in many calculations.

In the following discussions, it is useful to define the *source axis* as the vector from the radius of curvature, through the optic, in the direction of a source. Note that the source axis must be perpendicular to the optic where it intersects the optic, and that a ray from the source pass through the optic without deviation (assuming that the ray did not have the misfortune to hit the top of a pore wall).

3.1.2. *Aberration*

That the above demonstration that the focal length is $R_c/2$ employed a limit should have given the reader a clew that the focal length is a bit more complicated!

Consider an incoming ray that is parallel to the optical axis and strikes the optic at a distance $R_c \sin A$ from the optical axis. Since the angle of reflectance is the angle of incidence, the reflected ray forms an angle A with respect to the radius passing through through the point of incidence. The ray crosses the optical axis a distance[6]

$$z_f = \frac{R_c}{2\cos A} \tag{1}$$

above the radius of curvature. One should note that since the height of the focus above the center of curvature depends upon the initial distance of the ray from the optical axis ($R_c \sin A$); there is no single focus. This is a form of spherical aberration; its effect can be seen in the middle panel of Figure 11. One can see that as one increases the off-axis distance at which the ray strikes the optic, z_f increases, as does the distance from the optical axis where the ray intersects "the focal plane". One should also note that rays incident from an angle B from the optical axis will also be focused z_f from the center of curvature, but at an angle B from the optical axis. Thus the "focal plane", such as it is, is a spherical surface, as shown in the right-hand panel of Figure 11.

Given a source at infinity, we can determine an upper limit to the z-extent of the "focal region", and of the size of the focal spot in the detector plane, by considering the location of the "focus" for each pore, starting on-axis and moving away from it. We make the assumption that only a single ray is reflected by each pore. That ray will cross the optical axis at a distance $z_f = R_c/(2\cos A)$ from the radius of curvature. We will consider the height above the nominal $R_c/2$:

$$\Delta z_f = z_f - \frac{R_c}{2} = \frac{R_c}{2}\left(\frac{1-\cos A}{\cos A}\right) \tag{2}$$

That ray will cross the optical axis at an angle $2A$, as can be seen from Figure 11. On the detector plane, that ray will fall

$$x = R_c\left(\frac{\sin A(1-\cos A)}{\cos^2 A - \sin^2 A}\right) \tag{3}$$

from the optical axis.

At this point, one could continue towards an analytic expression for the PSF size[7] but it is far easier to simulate an optic in one dimension. Figure 12 shows the number of pores contributing to the PSF as a function of the distance from the center of the PSF. This plot was constructed by calculating $\arctan(x, R_c/2) \sim x/R_c$ for each pore, a determining how many pores could contribute to each angular bin. (By expressing the result as an angle one removes the dependence on R_c.) Note the extreme narrowness of the "PSF" due to aberration; this is far far narrower than the PSF typically measured for SMO ($\gtrsim 9$ arcminutes). **Thus, the intrinsic aberration is not a significant part of the PSF.**

3.2. *The Effective Acceptance Area*

In this section we will derive the equations that determine the *effective acceptance area*, which is the area of the optic that contributes to focussing parallel rays from a particular direction. To make the problem easy to understand, we will consider the problem in only the x direction and we will assume that the incoming rays are parallel to the optical axis. We will also assume that the pore walls are parallel; we do not currently know to what extent this assumption is true. The pore is assumed to have a width W and a length (or depth) L.

[6] Noting that the triangle is isosceles, so that the third angle is π-$2A$, the rest follows from the law of cosines.

[7] The density of rays crossing the optical axis at Δz is given by $dA/d\Delta z$:

$$dA/d\Delta z = \frac{2}{R_c}\left(\frac{\cos^2 A}{\sin A}\right). \tag{4}$$

Similarly, the density of rays striking the detector plane a distance x from the optical axis is given by dA/dx:

$$dA/dx = \frac{1}{R_c}\left(\frac{\cos^2 2A}{\cos 2A(\cos A - \cos 2A) + 2\sin A \sin 2A(1-\cos A)}\right). \tag{5}$$

At this point, one would want to evaluate

$$\int_0^N \pi x \frac{dA}{dx} dx \tag{6}$$

which is immediately problematic, even without considering the issues raised in the text that follows.

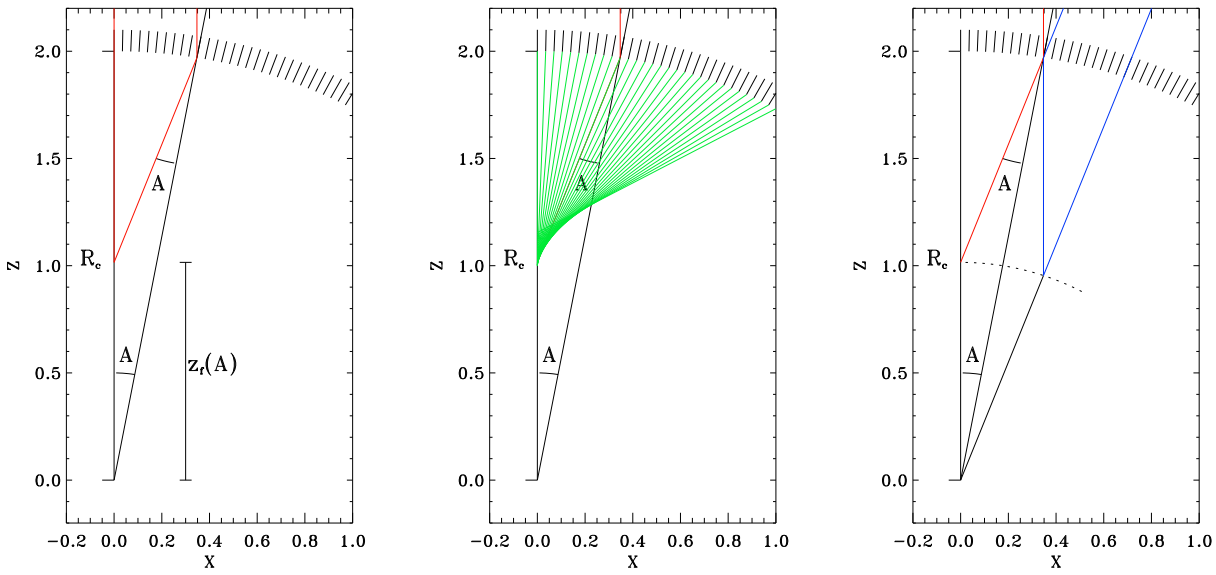

Figure 11. Left: The fundamental geometric construction for the optic. The vertical line to the left is the optical axis. The series of short radial lines represents the walls of individual pores, a cross-section of the optic. The *red* lines are an incident rays parallel to the optical axis. The vertical bar represents the distance above the center of curvature at which the off-axis ray intersects the optical axis. **Middle:** Demonstration of the lack of a single focus. Each green line is the path of a ray, parallel to the optical axis, having struck a different pore. The intersection with the optical axis was calculated for each ray using Equation 1. **Right:** Demonstration of the spherical "focal plane". The *blue* lines are two parallel rays that are incident from angle $2A$ from the optical axis. The intersection of the two rays is still z_f from the center of curvature, but at an $2A$ from the optical axis.

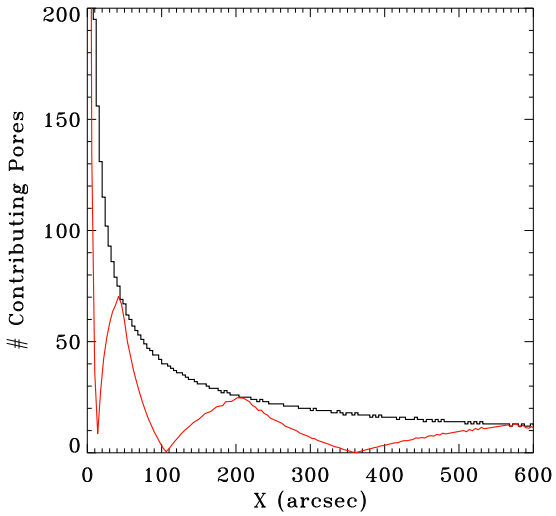

Figure 12. A simulation of one-dimensional optic with R_c=1000 mm. *Black:* The number of pores that contribute to the PSF, as a function of the distance from the center of the PSF, expressed as an angular distance. As will be seen, due to geometry alone, the contribution of pores to the focus varies with distance from the optical axis. This effect is included in the *red* curve. The reflectivity of the optic also decreases with distance from the optic axis, which would further decrease the number of rays falling far from the center of the PSF.

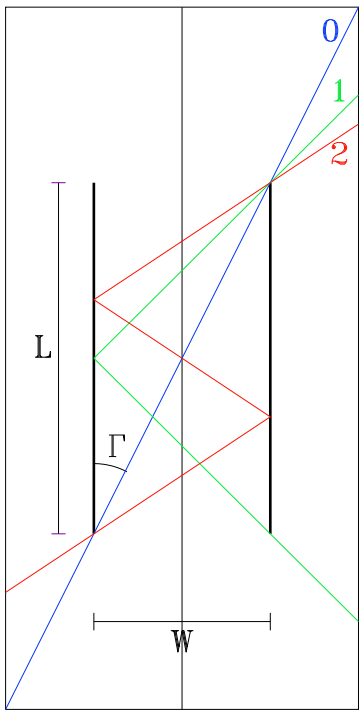

Figure 13. The cross-section of a pore, shown by the thick lines, demonstrating the limiting angle Γ at which a ray can pass through the pore with n reflections.

Figure 13 shows the cross-section of a pore with a selection of critical rays, marked 0 through 2. In order for a ray to pass through the pore without a reflection, the angle with respect to the pore axis, Γ, must be less than $\arctan(W/L)$. Not all rays at angle Γ will pass through without reflection, but we'll come back to that point shortly. To pass through with only a single reflection in a given dimension, $\Gamma < \arctan(2W/L)$. To pass through with n or fewer reflections in a given dimension,

$$\Gamma_n < \arctan((n+1)W/L). \quad (7)$$

If the pore walls are strictly radial (rather than parallel) the equations become significantly more complicated, but the results are not significantly different. For radial pore walls

$$\Gamma_1 = \arctan((2\cos\beta/\cos 2\beta)(W/L + sin\beta)) \quad (8)$$

where

$$\tan(\beta) = W/2R_c \quad (9)$$

For our instrument, the difference between Equation 7 and Equation 8 is $< 0.1\%$.

From the above, it should be apparent that rays striking near the optical axis will pass through the optic undeviated and unfocused. In order to be focussed (at least in one dimension) by a single reflection, an on-axis ray must strike the optic within $\Gamma_1 R_c$ of the optical axis. If the ray strikes slightly further from the optical axis, it will be reflected at least twice in the x dimension. A ray that is reflected twice in a given dimension will not be focussed but will leave the optic parallel to the input ray. We can generalize further; **a ray reflected an odd number of times in a given dimension will be focussed in that dimension while a ray that is reflected an even number of times in a given dimension will not be focussed in that dimension.**

Even further from the optical axis rays will be reflected thrice in the x dimension, and thus will be focussed, but the throughput will be much lower, being proportional to r^n where r is the reflectance and n is the number of reflections.

Thus, the effective acceptance area is, roughly speaking, the area over which rays can be focussed with a single reflection per dimension. For a given W and L, the *angular* size of that area is fixed to be within $\arctan(2W/L)$ of the optical axis. Thus, **increasing the size of the optic will not increase the effective area.** One can only increase the effective area by increasing the radius of curvature (which increases the physical area within the angle Γ_1 from the optical axis) or by changing the W/L ratio. The latter method will generally decrease the fraction of focussed to unfocussed light. This problem will be addressed in §11.1.

3.3. *Transmission of a Single Pore*

For a pore oriented at an angle Γ with respect to the incoming ray, the minimum number of reflections is

$$n_{min} = \text{Integer}\left[\frac{L}{W}\tan\Gamma\right]. \quad (10)$$

However, we note that a ray at a limiting angle is entering the pore at one edge. The parallel pores that enter

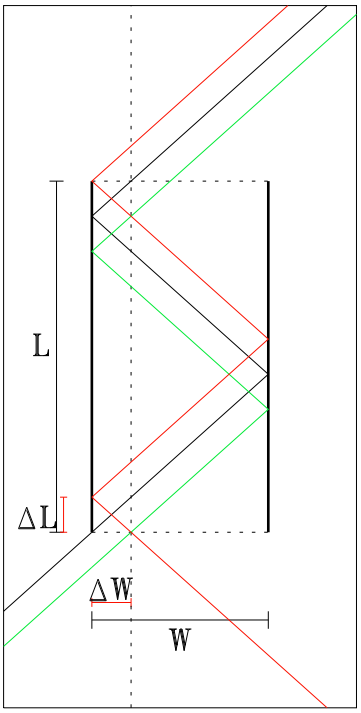

Figure 14. The cross-section of a pore, showing the construction for determining what fraction of the pore area allows n reflections and what fraction allows only $n+1$ reflections.

the center of the pore will have a different number of reflections.

Figure 14 shows the geometric construction used to determine what fraction of the pore opening allows n_{min} reflections. The figure shows an example with n_{min}=2. The black line shows the limiting ray for two reflections. If the ray enters the pore to the right of the limiting ray, the ray will have two reflections. If the ray enters to the left of the limiting ray, it will experience three reflections. That is, of the rays entering the pore, some must be reflected n_{min} times in order to exit, while the remainder must be reflected n_{min}+1 times in order to exit the pore. Assuming a uniform density of rays entering the pore, we can calculate the fraction of rays being reflected either n_{min} or n_{min}+1 times.

Continuing to use Figure 14, if

$$\Delta L = L - \frac{n_{min} W}{\tan\Gamma} \tag{11}$$

then

$$\Delta W = \Delta L \tan\Gamma \tag{12}$$

and thus the fraction of the pore opening for which rays at angle Γ experience $n_{min}+1$ reflections is $f_{min} = \Delta W/W$ while that fraction for with those rays experience n_{min} reflections is $f_{max} = 1 - \Delta W/W$.

Combining all of the lines of above equations we find that

$$f_{min} = \frac{L\tan\Gamma}{W} - \text{Integer}\left[\frac{L\tan\Gamma}{W}\right] \tag{13}$$

$$f_{max} = 1 - \left(\frac{L\tan\Gamma}{W} - \text{Integer}\left[\frac{L\tan\Gamma}{W}\right]\right) \tag{14}$$

Thus, if the reflectivity of the pore walls for an incidence angle Γ is $r(\Gamma)$, then the throughput of a single pore is

$$f_{min} r^{n_{min}} + f_{max} r^{(n_{min}+1)} \tag{15}$$

which is just the fraction of rays (or photons) entering the pore that actually exit it. Note that one term in this equation represents rays that are focused while the other term represents rays that are not focussed, but fall elsewhere on the detector. Thus, simulation of the optic actually requires two calculations; the first is the calculating the throughput, the second is calculating where the rays strike the detector.

If one desires the throughput of the entire optic, that is, the effective area, then one must sum over all of the pores. This summation introduces another factor, the projection of the pore opening. A pore that is aligned to the incoming rays has an opening of W. A pore that is at an angle Γ to the ray has an effective pore opening of only $W\cos\Gamma$. There is no simple expression for the total effective area because the reflectivity is a function of the angle of incidence. However, consideration of the figure in Appendix B suggests that one might actually be able to come fairly close with an analytic expression for the reflectivity as a function of the angle of incidence.

Assuming that the optic always has a radius greater than Γ_3, the effective area should scale as R_c^2, just because the number of pores within Γ_3 increases as R_c^2 . In this case the ratio of the area within Γ_i to the area within Γ_{i+1} does not change, so there are no second-order effects.

3.4. *Effective Area Redux*

It is useful to consider the throughput of pores as a function of off-axis angle Γ. From Figure 15 it is clear that the bulk of the contribution to the focused rays comes from pores where the ray was reflected (in the a single dimension) only once. That contribution is negligible on the axis. The fraction of rays focused increases with angle from the instrument axis, peaking at Γ_0 and declining to Γ_1. (OK, this statement ignores one significant condition, which will be discussed in §5.1.) There is also a contribution to the focus from rays that were reflected thrice (Γ_1 to Γ_3), but there is negligible contribution from higher numbers of reflections. The data used for this demonstration, a Nickel surface reflecting 0.55 keV photons, is typical. At higher energies, the triple reflection contribution is further reduced. Conversely, if the reflectance remained high at higher angles, of course, there would be more significant contributions from higher numbers of reflections.

Thus, depending somewhat on the L/W and the R_c, the bulk of the focussing for a source on the instrument axis will actually be done near the edges of the SMO facet. This fact has significant ramifications for both design and testing, and will be explore further in §§5, 9, and 11.

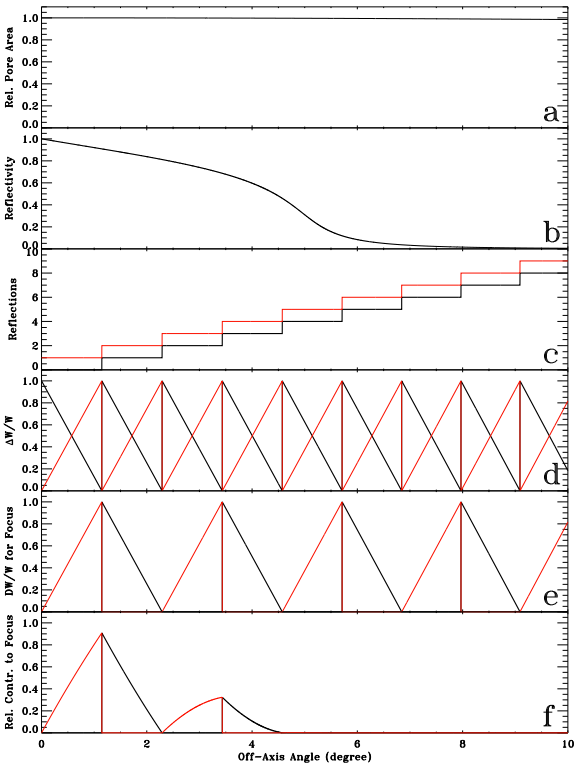

Figure 15. The contribution to the focus as a function of distance from the optical axis. These plots have been calculated for a one-dimensional optic where the incoming rays are parallel to the optical axis. **a)** The projected area of the pore, a, as seen by the incoming rays. **b)** The reflectivity, r, of the pore wall as a function of the angle of incidence. This demonstration used Nickel with no surface roughness for a photon energy of 0.55 keV. **c)** The minimum number of reflections, n_{min}, in black, and the maximum number of reflections, n_{min}+1, in red. **d)** The fraction of the pore area allowing n_{min} reflections (1-$\Delta W/W$), in black, and the fraction allowing n_{min}+1, $\Delta W/W$, in red. **e)** The same as the previous panel, but only including rays that are focussed. **f)** The relative contribution to the focus, $ar^{n_{min}}(1-\Delta W/W)$, in black, and $ar^{(n_{min}+1)}\Delta W/W$ in red.

Note that it is the angular size of the region for which $n_{min} = 0$ that sets the size of the "squares" in the PSF. The minima in the PSF there are due to those photons being removed from the unfocussed component, and being fully or partially focussed. This also means that if the shadows of your support structures falls at the location of the minima in the PSF, then you may have serious problems with throughput (for a single facet instrument) of with strong variation in the response.

3.5. *The FOV*

A decent approximation is that size of the FOV, as characterized as the angular size of the region where the vignetting function[8] is greater than 0.5, is

$$\mathrm{Max}(\Gamma) = 2R_o/R_c. \qquad (16)$$

where R_o is the radius of the optic measured perpendicular to the optical axis. This is merely the application of a simple geometric idea; the edge of the optic defines the maximum angle at which a ray can pass through a pore without reflection. At that angle, half of the effective acceptance area is off the optic, and thus the vignetting function should be ~ 0.5 at that point.

[8] By vignetting function we mean the effective area as a function of angle from the instrument axis, normalized to the greatest effective area at that energy. Thus the vignetting function has a maximum of unity.

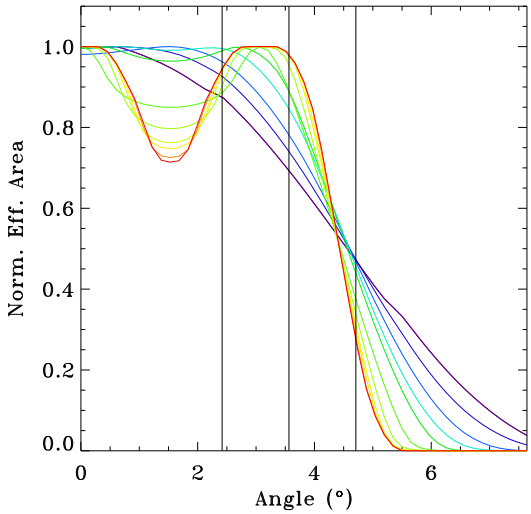

Figure 16. The vignetting function for the LEXI optic. The different colors are for different energies from low (0.1 keV, purple) through 0.3, 0.5, 0.7, 1.0, 1.5, 2.0, 2.5, 3.0, and 4.0 keV to high (5.0 keV, red). The thick vertical bar marks R_o/R_C, $R_o/R_C - \Gamma_1$, and $R_o/R_C - \Gamma_2$ for this device.

Figure 16 shows the vignetting function for a LEXI style optic with 3×3 40 mm facets and a focal length of 730 mm. The vignetting function was calculated at a number of energies from 0.1 keV to 5.0 keV. We note that at high energies, the vignetting function is very narrow, with a dip half-way between the edge and the center. Since the bulk of the photons at high energies are not focussed, the dip is the shadow of the support structure. At lower energies more of the photons are focussed. The dip appears at the center because the support structure is shadowing the region where the bulk of the on-axis focussing is done. There are increasing tails to large angles as the energy decreases; the angle of incidence can be larger at lower energies. We see that the above approximation for the size of the FOV is roughly good for lower energies, where more of the light is focussed.

For many applications, one is interested in the angular size of the region over which the vignetting function is relatively flat. This angular size is a function of the size of the optic and effective acceptance area for single reflection. As seen above in Figure 15, the area within Γ_1 makes the greatest contribution to the PSF. Thus, we can *very* roughly state that the edge of the essentially unvignetted FOV will be an angle somewhat greater than Γ_1 and less than Γ_0 in from R_o/R_c, or that the FOV has a width of

$$2(R_o/R_c - \Gamma_1 < \mathrm{Max}(\Gamma)_v < 2(R_o/R_c - \Gamma_0). \qquad (17)$$

Although we have not explored parameter space thoroughly, we find that the above equation is a good approximation for the region with a vignetting function > 0.9 for optics that are larger than $\sim 3\Gamma_0$.

This calculation also points out that any reasonable optic should have $R_o \gtrsim 2R_c\Gamma_1$; any smaller and you are not using the optic at it's maximum efficiency.

3.6. *Detector Size*

It seems otiose to note that since the focal surface is roughly $R_C/2$ from the optic, the detector needs to be at least half the linear size of the optic. However, a source $2R_O/R_C$ from the optical axis still has half the effective area as a source on the optical axis, so it behooves us to make the detector larger than $R_C/2$ if at all possible.

3.7. *A Few More Musings*

M. Galeazzi has inquired about radial pores, that is, pores whose walls are not parallel, but are strictly perpendicular to the surface of the sphere. We assume that walls are at an angle $\epsilon/2$ to the pore axis (at an angle ϵ with respect to one another), and that a ray comes in at an angle δ with respect to the pore axis, so that it strikes the interior wall at an angle $\Gamma_1 = \delta + \epsilon/2$. Looking at the first triangle formed by the left wall, the normal to the right wall, and the ray after the first reflection, it is clear that $\Gamma_2 = \Gamma_1 + \epsilon$ and that for each successive reflection

$$\Gamma_N = \Gamma_1 + (N-1)\epsilon. \tag{18}$$

This means that each successive reflection becomes more normal to the surface. For infinite reflectivity and a very long pore, the ray will reverse and return through the top of the pore! More to the point, reflectivity decreases strongly as the rays become more normal to the surface, suggesting that tapered pores will produce even less three-reflection throughput than parallel pores.

Typically, we only need to worry about, at most, three reflections in a given dimension. In that case, the difference between the parallel case and the radial case is 3ϵ. For a 20 μm pore in a 1000 mm radius of curvature facet, $\epsilon \sim 4\farcs12$, while for a 750 mm radius of curvature facet, $\epsilon \sim 5\farcs5$. Thus, this issue is not important for current devices. *However it should be noted that the larger the pores or the shorter the focal length, the more significant this effect will be.*

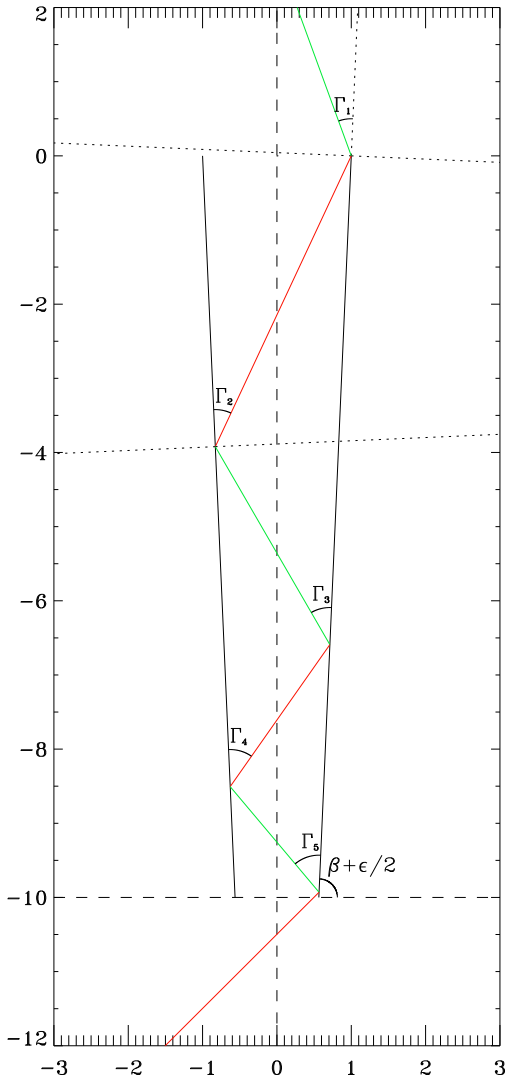

Figure 17. Rough draft for a plot demonstrating the effects of a "radial pore", one whose walls are not parallel, but are strictly perpendicular to the sphere. Each reflection becomes more normal than the previous one.

4. MATHMATICS OF A REAL SMO

This section explores a few of the issues of a single real SMO; it is by no means an exhaustive list. We explore three large scale issues, the radius of curvature, the bias, and the intrinsic deformation due to the slumping of the optic. In the future, we will consider the random misalignments of individual pores, which Willingale has found to be a significant factor in the degradation of the PSF.

4.1. *Radius of Curvature*

Errors in the radius of curvature are errors in focal length; your optic will be out of focus. Remember that the part of the optic that is near the source axis does not contribute significantly to the focussed light; the bulk of the contribution comes from the region to either side of the source axis where n_{min} changes from 1 to 2. Thus, since the focused rays are coming from opposite sides of the source axis, those rays meet (and cross) at the focus. If the focal plane is not at the focus, those two bundles with strike the focal plane at different locations. Thus, an out of focus optic's response to a point source is the standard cross, but with both arms doubled, as seen in Figure 18. Note that the doubled arms are strictly parallel.

Of course, the radius of curvature need not be constant over the entire facet. Consider the case of an optic with a constant R_{c_x} and a R_{c_y} that varies linearly with x. The example in Figure **??** set $R_{c_x} = R_{c_y}$ at the center of the device, with R_{c_y} increasing from the left side of the device to the right. The figure shows the PSF for an on-axis source. Again we see the doubling of the arms, but the distance between the arms depends upon the local radius of curvature. However, in this case, the change in R_{c_y} is ± 4 cm, which much larger than the errors typically seen in facets.

The above case is rather trivial. One can also consider the case where the curvature, R_{c_y}, is a function of y. Figure 20 shows the PSF for an on-axis source where the radius of curvature at $(y = 0)$ is roughly 6% longer than it is at the upper and lower edges. Since the R_{c_y} is changing over the range of y which is primarily responsible for focussing in that direction, the two parallel arms are significantly blurred. It should also be noted that the width of those arms will change strongly with the y location of the source.

4.2. *Bias and Misalignment*

The *bias* is the extent to which the pores are not perpendicular to the surface of the SMO facet before slumping. We have assumed that a uniform bias produces a constant $(\Delta\alpha_x, \Delta\alpha_y)$ in the tilt of all of the pore walls. The result is to shift the location of the center of the PSF by $(2\Delta\alpha_x, 2\Delta\alpha_y)$. This is shown in the first panel of Figure 21. Given the manufacturing process, it is not at all impossible for the bias to change from one segment of the facet to the next[9]. The second panel of Figure 21 shows the PSF of an on-axis source if the bias changed from $-\Delta\alpha_y$ to $+\Delta\alpha_y$ as one moves from left to right. *The two arms are no longer perpendicular.*

[9] See the manufacturing note in the introduction.

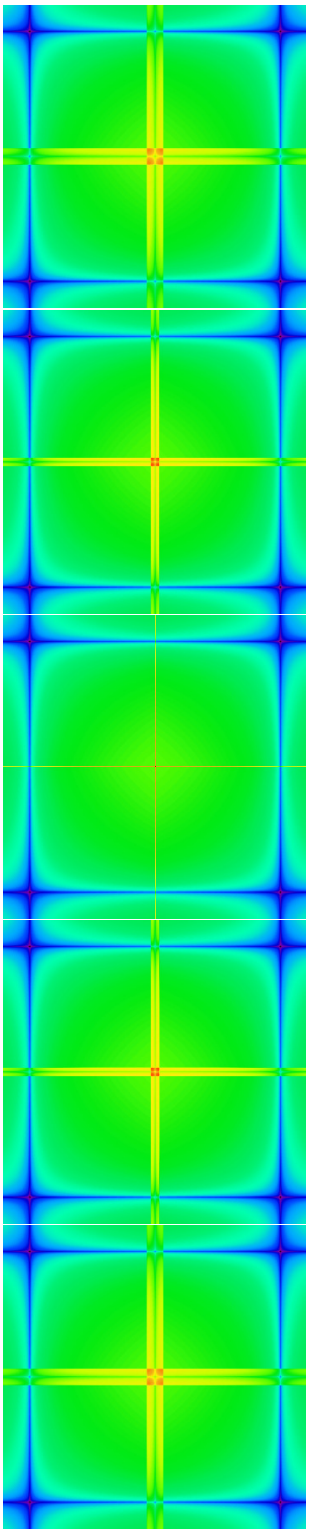

Figure 18. The PSF as the focal plane is moved through the focus. In each case the PSF is formed by a single 4 cm by 4 cm facet with R_c= 75cm, when the source is on the instrument axis. All simulated images are logarithmically stretched to show the fainter structure of the PSF. From top to bottom the images are for -2.0 cm, -1.0 cm, 0.0cm, 1.0 cm, and 2.0 cm, where a positive number indicates that the detector is further from the optic.

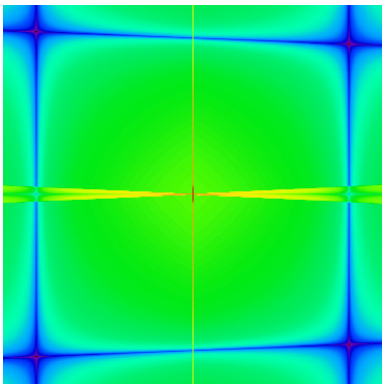

Figure 19. The PSF of a source on the instrument axis for an optic where the radius of curvature in the y direction, R_{c_y} changes smoothly as a function of x. At the center, $R_{c_x} = R_{c_y} = 75$ cm. At the left edge the R_{c_y} is 4 cm longer than at the center, and at the right edge the R_{c_y} is 4 cm shorter than at the center.

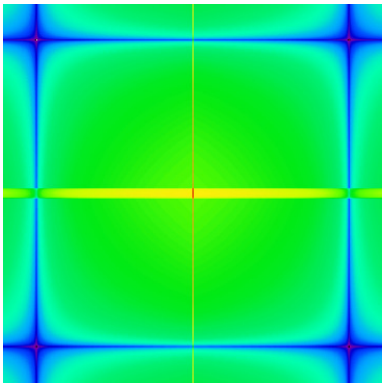

Figure 20. The PSF of a source on the instrument axis for an optic where the radius of curvature in the y direction, R_{c_y}, changes smoothly as a function of y. In this case the radius of curvature at the center of the facet is longer than it is at the upper and lower edges of the facet.

4.3. *Rotation*

Given that SMO are not axisymmetric, one might be understandably worried about rotation, either of individual pores, or of the SMO as a whole. Consider, in a very simplified two-dimensional way, the interaction of a single ray with a single pore. Figure 22 (top) shows the interaction of a ray with a single wall. If the wall is rotated by α, the output ray moves by 2α in the same sense or direction as α. Figure 22 (bottom) constructs the path of a ray being reflected by two perpendicular walls; the output ray is antiparallel to the input ray. This is true, independent of the rotation of the pore by α. With these exemplars, we can easily understand Willingale's rule: rotation of a facet by α does not change the location of the focus, but rotates the PSF by α.

4.4. *Slumping & Pore Deformation*

Although we do not know exactly how the slices are slumped[10], we can reasonably assume that the process can be modeled by allowing the flat slice to slump over a spherical mold. For this exercise we ignore the issue of the thickness of the slice, and how slumping suggests that

[10] This statement is a bit misleading. Photonis has explained the procedure by which they slump the facets. What is not understood is what the glass is actually doing during this process.

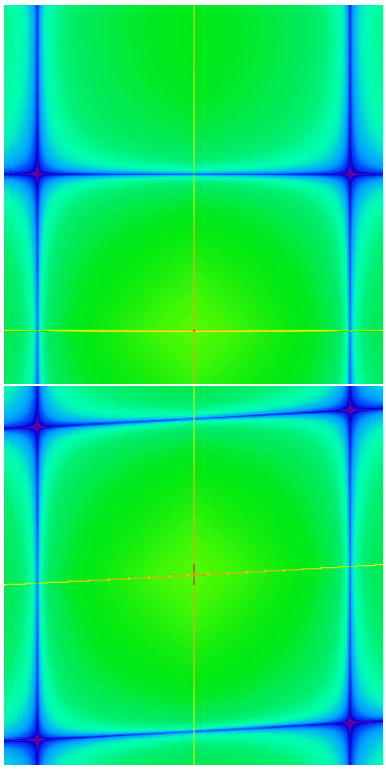

Figure 21. The effects of pore bias on the PSF of a source on the instrument axis. **Top:** A uniform $\Delta\alpha_y$ of XX'. **Bottom:** The $\Delta\alpha_y$ changes smoothly with x.

the part of the pore walls near the upper surface much stretch compared to the part near the lower surface.

Figure 23 demonstrates the issue in a rather schematic way. The thin plate with a radius of D is placed on a spherical mold. We assume that the lower surface of the plate does not stretch during slumping and conforms smoothly to the mold. If the radius of curvature of the mold is R, after slumping the edge of the thin plate will now be a distance $D' = R_c \sin(D/R_c)$ from the instrument axis. Thus, the pores falling on a circle of radius D from the instrument axis must now form a circle of radius $D' < D$. (See Figure 24. The slumping thus ought to produce a compressional force perpendicular to the local vector towards the facet axis.

4.4.1. *A Possible Mathematical Description*

We will further assume that there is no stretching or compressing of the pore walls along their lengths, but we will assume that the pore walls can pivot like hinges where they intersect. Since the glass is slumped while hot, the "no stretching" assumption may not be reasonable. By these assumptions, the pores on the x and y axes of the optic will not be altered as the compressional force is along the lengths of the pore walls. At an angle $\pi/4$ from the x or y axes, the compressional force must exerted on diagonally opposed corners and one would expect the square pore to become diamond shaped, with the longer axis aligned with the local radius to the facet axis. One might also expect that pores along the $\pi/4$ vector to be offset outwards as a result of the elongation of pores on the same vector at smaller radii. Overall, one *might* expect a pin-cushion-like distortion in the arrangement of pores.

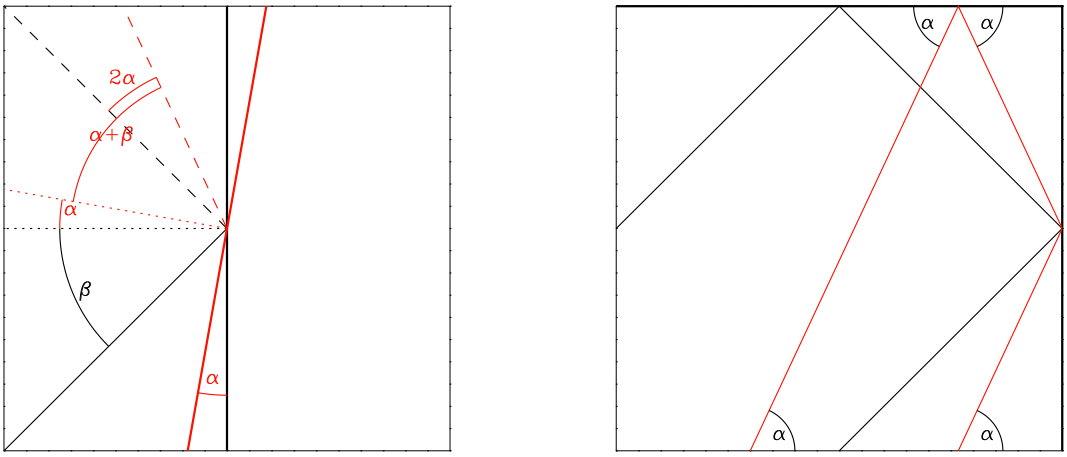

Figure 22. A demonstration of the effect of rotating a pore. *Top:* For a single reflection, rotation of the wall by α results in a rotation of the output beam by 2α. *Bottom:* For a double reflection from perpendicular walls, the rotation of the pore by δ causes no rotation of the output ray. Here, for clarity, I show a rotated beam rather than the equivalent rotated box. For both figures the thick lines are the reflective surfaces.

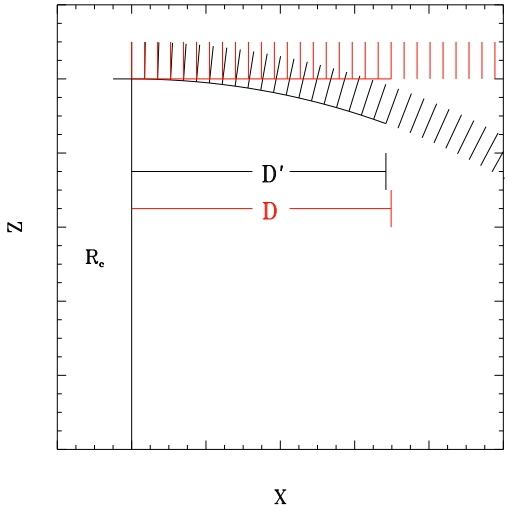

Figure 23. A cross-section of the optic before and after slumping. A point a distance D from the instrument axis of the unslumped optic will be a distance $D' < D$ after slumping.

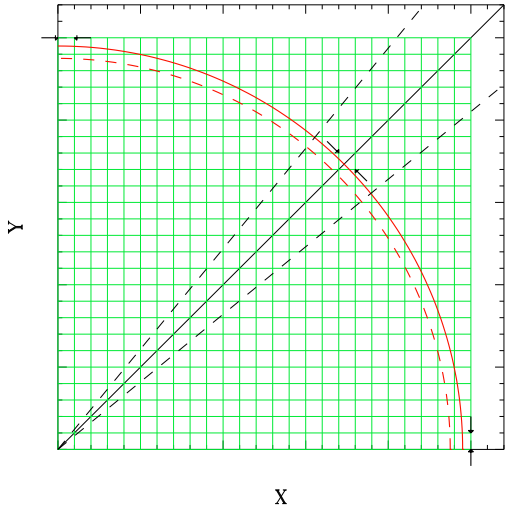

Figure 24. A demonstration of the ways pores may be distorted due to slumping. The *solid red* line shows the radius D before slumping while the *dashed red* line shows the location of that radius after slumping. The *green* lines show the grid before slumping while the arrows show the direction of the forces on each pore. The *dashed* lines show $\pi/8 \pm !pi/32$.

One might develop a scheme in which the compression of a given pore is proportional to the projection of the compressional force onto the pore diagonal, but it is certainly not clear whether this is how the grid behaves. Willingale states that this problem was given to an expert in finite element analysis and has been solved. While an independent solution is found on this side of the Atlantic, we can propose some simple analyses to understand the magnitude of the issue.

With a modicum of care for round-off errors, one can implement a numerical solution assuming an infinitely thin slumped plate. We assume that the walls do not change their lengths, but are free to pivot at their intersections. If we fix the location of wall intersections along the x and y axes of the optic, we can then sequentially solve for the location of all of the other wall intersections.

The derivation is given in the appendices. Problems with numerical accuracy can be decreased if one requires the solutions to be symmetric about the $\pi/4$ radius. The amount of deformation as a function of location for the upper right quadrant of the optic is shown in 25. The amount of deformation of a pore is measured as the difference between the slumped pore diagonal and the original pore diagonal. Here we measure the more radial of the two diagonals so that the distortion increases towards the $\pi/4$ radius and towards greater radii. As is shown in the appendices, this analytic solution has the functional forms expected from the simple compression along the circle. The deformation as a function of azimuth has the

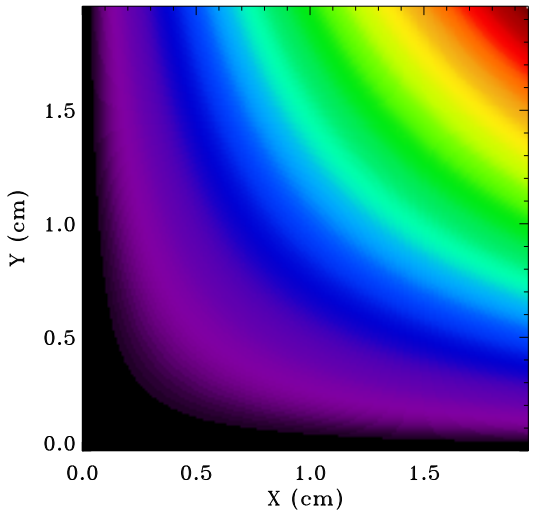

Figure 25. The pore compression as a function of location for the upper right quadrant for the $\sin(2\phi)$ model. The color scale runs from insignificant deformation (black), to maximum deformation (red).

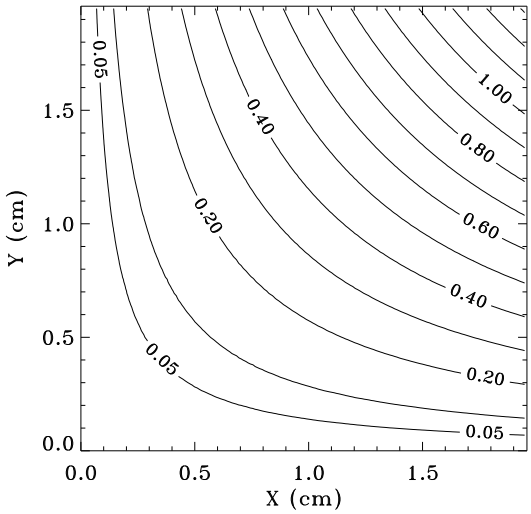

Figure 26. The angle between two adjacent sides of the pore as a function of location expressed as the difference from perpendicular, in arcminutes.

form

$$\sin(2\phi) \tag{19}$$

while the deformation along the $\pi/4$ radius has the form

$$1 - \frac{R_c}{D}\sin\left(\frac{D}{R_c}\right). \tag{20}$$

This later quantity is proportional to relative compression at a particular radius $(D - D')/D$. However, the scaling of these functional forms to fit the analytic solution is not obvious. By fitting these functional forms to the calculated deformation we find that the deformation, d is given precisely by

$$1.5\sin(2\phi)\left(1 - \frac{R_c}{D}\sin\left(\frac{D}{R_c}\right)\right). \tag{21}$$

4.4.2. *Deformation of a Single Pixel*

Of interest is the extent to which the walls of the pore are no longer perpendicular. This can be calculated from the analytic model using the dot product of adjacent walls. The difference between the measured angle and $\pi/2$ is shown in Figure 26 as a function of location[11]. For the bulk of the optic, the difference is less than an arcminute. Consider just a single reflection from a single wall. If the wall is rotated an arcminute, the beam originally with undeviated in the $\hat{y}$ direction will no suffer a $2'.0$ deviation in the $\hat{y}$ direction. A $2'.0$ rotation of the beam, for the STORM configuration, is equivalent to a ~ 0.03 cm movement in the detector plane, which is much smaller than our detector pixels. For SMILE type detectors, with 108 μm effective pixels, this movement is ~ 2.6 effective pixels. SVOM has 75 μm pixels so this would mean a motion of 4 detector pixels. Thus, the deformation could be important for those instruments, while negligible for STORM.

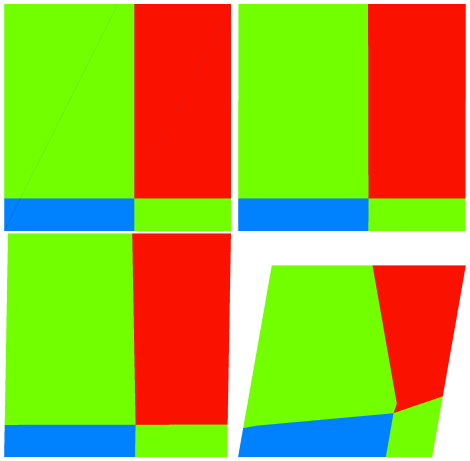

Figure 27. The regions of the pore producing one (blue), two (green), or three (red) reflections. *Top left:* no deformation, *top right:* a tenth of a degree deformation, *bottom left:* one degree deformation, and *bottom right:* ten degrees of deformation.

However, the effect of deformation is not quite so straight forward, since we are typically dealing with multiple reflections from non-perpendicular walls. As shown in §3, some fraction of the pore area will lead to f_{min} reflections while the remainder will lead to f_{max} bounces. For a square pore the two dimensions are separable. This is not so for a deformed pore. Figure 27 shows the relative areas for each of the possible number of reflections as the pore is progressively deformed. The relative areas for a tenth of a degree deformation are less than a half percent different from the un-deformed case.

[11] One must be careful about how one measures this angle. The angle cited in the text was measured, in essence, in the plane tangent to the sphere at the location of the pore. Vectors describing two adjacent walls were constructed from the calculated wall intersections, and the angle taken from the arccosine of the dot product of those vectors. If, instead, one were to measure the angle as projected onto the plane perpendicular to the optical axis, one would find the angle changes by a fraction of an arcsecond! For the D/R_c ratios encountered with STORM, the elongation of the pore in the radial direction is roughly compensated by the $\cos(D'/R_c)$ effect of the projection. The change in this projected angle is comparable to noise in the numerical accuracy.

5. SMO MOSAICS

Given their typical size (4 cm by 4 cm), single SMOs are not particularly useful. Instead, one must mosaic them together in order to increase throughput[12] and field-of-view. There are a number of issues involved with mosaicking. One will need to support the facets, and any support structure will produce shadows on the detector plane. Since the individual SMO are square, mosaicking them onto the surface of a sphere is not trivial. Mosaicking also introduces yet more ways to degrade the image quality. We will consider two of them; the frame/facet mismatch (where the radius of curvature of the facets does not match the radius of curvature of the frame in which they sit) and the misalignment of facets.

5.1. *Support Structures*

It is useful to consider the throughput of pores as a function of off-axis angle Γ. From Figure 15 it is clear that the bulk of the contribution to the focused rays comes from pores where the ray was reflected (in the a single dimension) only once. That contribution is zero on the optical axis, peaks at Γ_0, and declines to Γ_1 There is also a minor contribution from rays that were reflected thrice (Γ_1 to Γ_3), but there is negligible contribution from higher numbers of reflections.

Consider a facet centered on the optical axis. For the LEXI optic, the edge of the center facet is 1.°528 off-axis, while Γ_0=1.°146. Thus, the region contributing most to the focussing of an on-axis source is mostly on that facet. For the proposed STORM optic, however, the edge of the facet is 1.°146 from the optical axis, placing the support structure right where the contribution to focussing is at its greatest. Thus, STORM optic would be a very poor instrument for imaging a source on the optical axis. The STORM situation is shown (roughly) in Figure 28.

Consider the difference between placing the optical axis in the center of the facet (centered, middle panel of Figure 28) and placing it at the crossing of the supports (crossed, bottom panel of Figure 28). In the crossed image, the obscuration removes primarily the low Γ rays, which are not strongly focussed, while the obscuration in the centered image falls right on the source of the greatest contribution to the focussed image. If the support structure period is twice the angular scale of the peak contribution (as it is with STORM) then one maximizes the amplitude of the variation in the throughput and (I believe, still have to check) maximizes the decrease of throughput per area obscured.

Figure 29 shows the vignetting functions for a LEXI-style instrument as a function of energy, for the total transmitted flux, as well as for the fully, partially, and non-focussed rays. As pointed out for a previous figure, at low energies the vignetting function has a dip at the optical axis due to partial obscuration of the peak focussing area by the support structure. At higher energies, the dip is due to the actual shadow of the support structure.

The fully focussed fraction typically falls with energy as the reflectivity for a given incidence falls with energy.

[12] This statement may seem as if I am repudiating the rule that increasing the size of the optic does not increase the effective area. However, for many typical R_C, the effective acceptance area is larger than the typical device size.

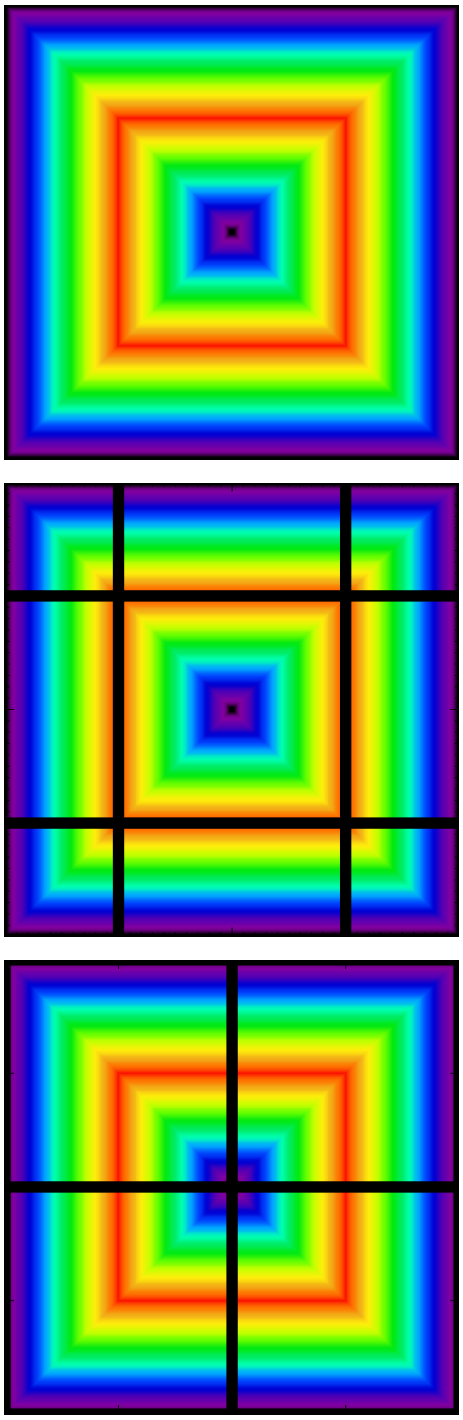

Figure 28. *Top:* A map of the relative contribution to the focussing as a function of position on the optic. *Middle:* The same map showing the location of the area shadowed by the support structure when a facet is centered on the optical axis. *Bottom:* The same map showing the location of the area shadowed by the support structure when the support structure crossing is centered on the optical axis.

Here we see a slight increase from the very lowest energy (0.1 keV) to ∼1 keV due to the fact (?) that at the very lowest energies three reflection focussing becomes more likely, and the device is not wide enough to include all of the area for which three reflection focussing is possible.

The partially focussed fraction holds a slight surprise. At the very highest energies considered here, the shadow

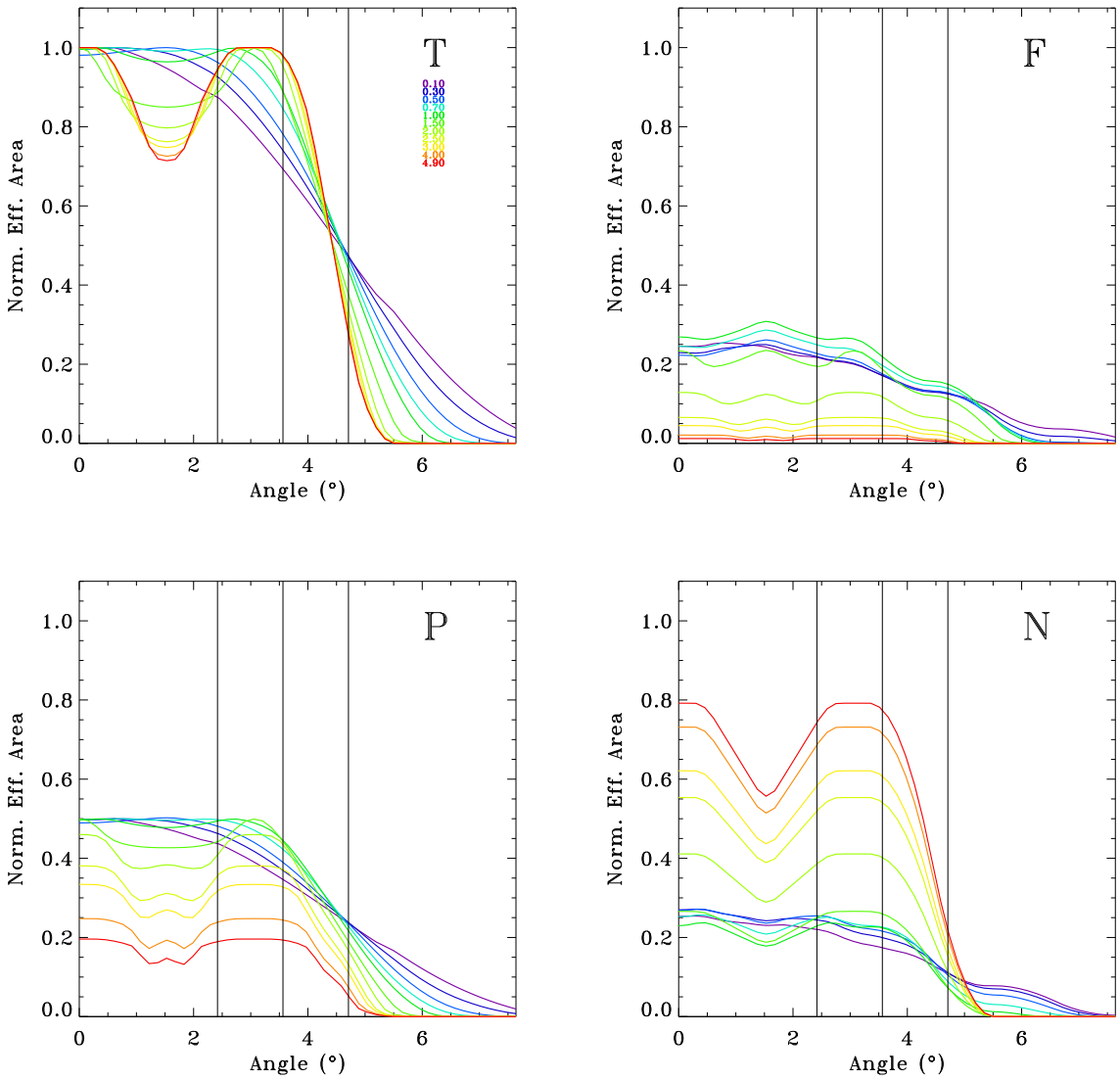

Figure 29. The vignetting function as a function of energy for the total transmitted flux (T), fully focussed flux (F), partially focussed flux (P), and non-focussed flux (N). In each case, the curve has been divided by the maximum of the total transmitted flux curve for that energy. The energies are given in the legend.

of the support structure shows a slight peak at its center. Note also how flat much of the vignetting function is. This is due to the fact that the reflectivity at this energy has fallen to zero for an incident angle of Γ_0. Thus, the peak of the reflectivity is angle smaller (perhaps much smaller) than Γ_0 from the optical axis. At the highest energy shown here, the peak reflectivity is slightly further from the optical axis as the width of the support structure. Again we note that the fraction of partially focussed light decreases strongly with energy.

The non-focussed fraction shows the expected behavior. At higher energies, the SMPO acts mostly as a collimator. At the lowest energies two-reflection (in a single dimension) rays become more likely, and the non-central squares of the PSF become more prominent.

One other useful concept to explore with these vignetting functions is the fraction of focussed light compare to the non-focussed light. Figure 30 shows this quantity as a function of off-axis angle. At both low and high energies the ratio is nearly flat. At moderate energies (∼0.7-1.5 keV) the fully focussed fraction can vary strongly, being much greater where the support structure minimizes the non-focussed flux. Reducing the focussed component compared to the unfocussed component at the centers of facets increases the point source detection threshold and will make structures in the diffuse emission more difficult to detect. This lack of detectability will be periodic across the FOV.

5.2. *Tiling Geometry*

Thus far we have been treating the optic as a single monolithic structure. There is, alas, a limit on the size of a single SMO. Thus larger optics must be made by tiling or mosaicking together individual SMOs, or facets, to attain the required size. How does one tile the square facets onto a spherical surface? In the following, we are going to explore close-packing the facets, ignoring the need for supports and such. We assume that the optic is $2N$ facets wide, and facets have a width F. (Clearly, N

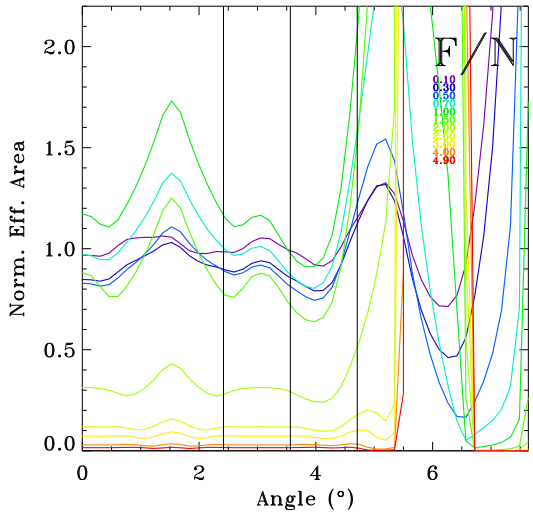

Figure 30. The fully focussed flux divided by the non focussed flux as a function of off-axis angle.

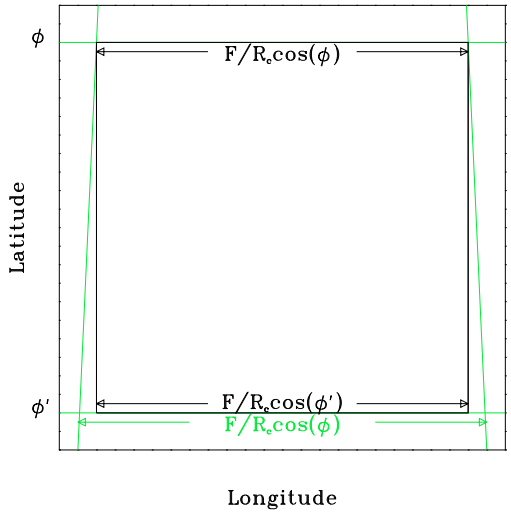

Figure 31. Demonstration of how a square facet sits into the latitude/longitude grid. All quantities are angles.

could be integral or half-integral. We've opted for this formulation to make some of the derivations easier in the following.)

When looking at a sphere, lines of constant latitude are, in fact and in deed, parallel. Thus, let us begin by assuming a pole in the $\hat{y}$ direction and tiling facets along a line of constant latitude, ϕ, that is supposed to be the outer limit of the optic in the $+\hat{y}$ direction. Clearly, $\phi = NF/R_c$ and we want to place the facets so that their upper edge is along the latitude NF/R_c. This is equivalent to placing the facets so that a vertical line through the middle of the facet is aligned with a line of constant longitude (for a pole in the $\hat{y}$ direction).

The width, in angle (that is, longitude), of a single facet whose top edge is along $\phi = NF/R_c$ will be $F/R_c \cos(NF/R_c)$. However, the equivalent width, in angle, along the bottom edge, will be $F/R_c \cos((N-1)F/R_c)$. It can be seen if the upper corners of two adjacent facets touch, their bottom corners will be separated by

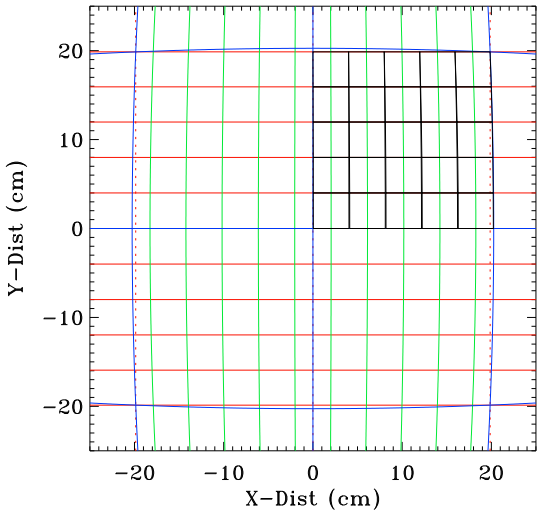

Figure 32. A projection of the optic into the xy plane. The optic has a spherical surface. The parallel *solid red* lines are lines of constant latitude if the pole were in the $\hat{y}$ direction while the *dashed red* lines are lines of constant latitude if the pole were in the $\hat{x}$ direction (fewer shown to keep the plot readable!). The *blue* lines are lines of constant longitude for the pole being in either the $\hat{x}$ or $\hat{y}$ direction. The *black* lines show the results of the first method of close-packing of the facets described in the text. The *green* lines trace the direction of the facet centers. Here we have assumed R_c=100 cm. Note that $\hat{z}$ is out of the page.

$$g = F\left(\frac{\cos\left((n-1)F/R_c\right)}{\cos\left(nF/R_c\right)} - 1\right) \tag{22}$$

in linear measure (not angle). Thus there will be a wedge shaped space between every pair of facets that is side by side, but none between the top of one row and the bottom of the next. The relative width of that wedge increases as one moves away from the equator.

There are two ways that one might think of tiling the facets. In both cases one starts at the center of the upper edge of the array of facets, moving outward from the center, and then down.

Constant Longitude Tiling: In the first case, one aligns the centers of the facets in the next row down with the longitudes of the centers of the upper most row. Thus, each column of facets is centered on a constant longitude, as shown in Figure 32. In this case, the gap between columns of facets increases strongly towards the equator. The gaps between facets for y=0 will be

$$g = F\left(\frac{1}{\cos\left(\frac{NF}{R_c}\right)} - 1\right). \tag{23}$$

For the STORM parameters and this tiling, the gaps between facets will be 0.0813 cm along $y = 0$. Depending on the details of the pore width/length ratio, the facet size, and the thickness of the support structures, the constant longitude tiling could exacerbate the periodic variation in the effective area across the FOV, as described in §**??**.

Close-Pack Tiling: In the second case, one tiles each row so that the corners furthest from the "equator" are touching while the corners closer to the equator are not.

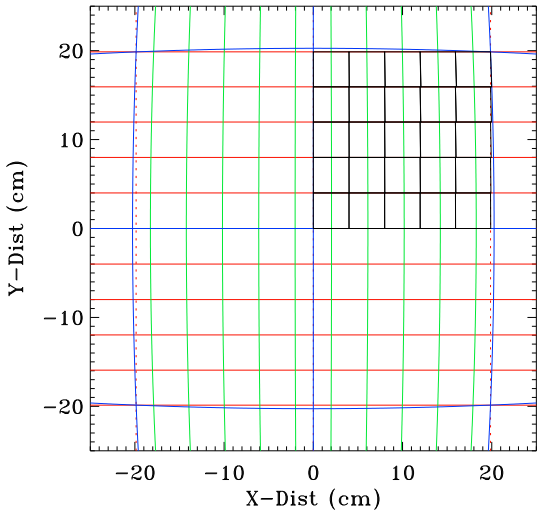

Figure 33. As for the previous figure, but showing the results of the second method of close-packing the facets.

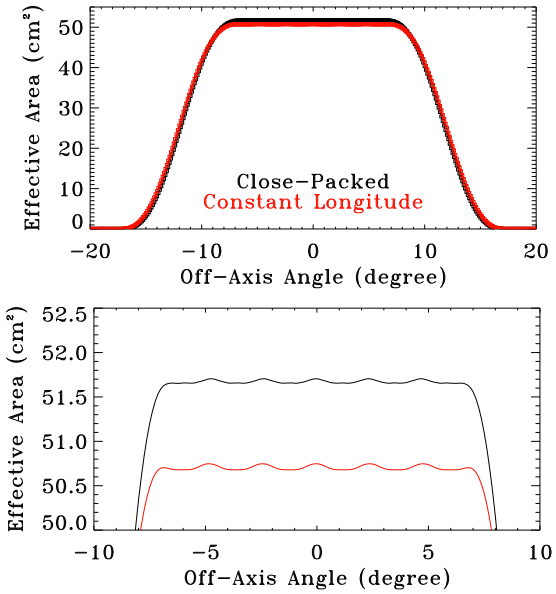

Figure 34. Vignetting curve for $\beta_y = 0$ the same device with close-pack (black) and constant-longitude (red) tiling.

In this case the gap size, g, depends upon the row number n as in Equation 22. For the STORM parameters and this tiling, the gaps between the facets will decrease from 0.0292 cm on the top row to 0.00320 cm on the row along y=0. This "saw-tooth" configuration minimizes the gaps between facets and minimizes the variation in the effective are within the FOV.

A Comparison: As discussed in another document, the Earth-shade must have a series of parallel interior fins in order to be short enough to be deployed. The fins must be perpendicular to the surface of the optic in order to minimize the shadowing by it of the optic. For mechanical stability, the base of the fin should be anchored to the optic support structure. Thus, they may either be flat and anchored to the longitudinal supports, or curved and anchored to the latitudinal supports. There are also configurations where some fins cross the centers of the facets. Since these fins can only be anchored at a limited number of locations, the feasibility of curved fins is not clear. Thus, it is worth considering the quantitative differences of the two methods.

If we assume the standard 4 cm facets, and assume a minimum 1 mm spacing between facets, then we can simulate the STORM optic for both tiling methods. The results are shown in Figure 34. We find that over the center of the FOV, the close-pack method produces an effective area that is $< 2\%$ higher than the constant-longitude method. The effective area shows a periodic variation whose amplitude is $\sim$0.07%($\sim$0.05% for the close-pack(constant-longitude) method. Thus, unless one really needs that last $\sim$1.8% improvement, the packing has little impact. This may not be the case if the minimum facet spacing is increased or the pore width/height ratio is changed.

5.3. *Frame/Facet Mismatches*[13]

The frame/facet mismatch occurs when the facet radius of curvature (R_F) is not the same as the radius of curvature of the frame in which the facets are set (R_C). In the case of LEXI, this was due to the delivered facets having a radius of curvature that was consistently shorter than the specification (730 mm versus 750 mm). Thus, even if the facets are correctly aligned so that the pore at the center of each facet is perfectly radial, the field of view will be discontinuous, in that a source falling between the two facets will produce two images, one due to each facet. At the corners, where four facets meet, one gets four images. The result can be understood from Figure 35.

Figure 35 (*top*) shows a cross-section along the x-axis of a multifacet optic. Here the radius of curvature of the frame is R_C, while the radius of curvature of the individual facets is $R_F < R_C$. The geometric construction of the frame is shown in black, while that of the individual facets is shown in red. This graphic is for an extreme case in order to make the relationships clear. The facets are more strongly curved than the frame, and their origins of curvature are a distance ΔR from the frame origin of curvature. Note as well that the area of the sky subtended by each facet is $\alpha' > \alpha$, the area of the sky subtended by a facet with R_F=R_C. Thus, a source which is at an angle $\alpha/2$ from the instrument axis (the z-axis in this diagram) is "seen" by both facets, but the light is focussed to different points by the two facets. This focussing is shown in the bottom panel of Figure 35. Here, the color coding indicates the relative contribution of each ray to the focus; blue-purple indicates a small contribution, while red indicates a large contribution[14].

To understand the implications of this configuration, we have to work through the mathematics. The black dashed line in the top panel of Figure 35 is a chord span-

[13] This work was done while at PANTER doing work with LEXI. Much of this work is due to Vadim Burwitz, for whom mosaicked SMO instruments are now familiar. My work here is mostly putting that work into my existing formalism.

[14] For the reader who may have jumped directly to this section, see Section 3.4 for an explication.

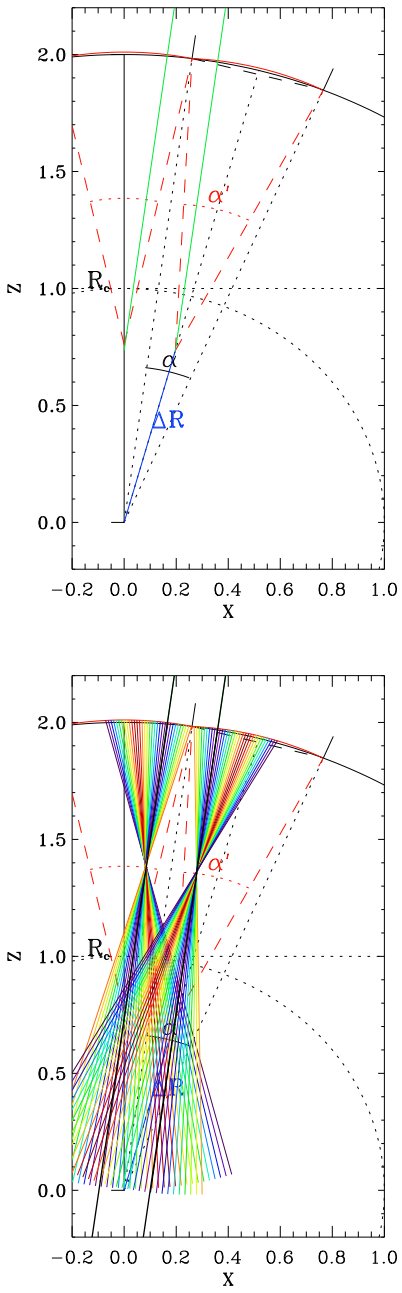

Figure 35. Cross-section of an optic with a frame/facet mismatch. The extent of the mismatch has been exaggerated in order to make all of the relevant geometry visible. *Top:* The diagram shows the central facet and one side facet. The frame and its measurements are shown in black. The **dashed** black line is a chord stretching from one side of the side facet to the other. The **dotted** black straight line is the nominal detector plane, while the **dotted** black curve is the focal surface. The facets, which have a shorter radius of curvature are shown in red. Their centers of curvature are at A and B, both a distance ΔR from the center of curvature of the frame. *Bottom:* The same as the previous panel, but showing the focussed rays from a source located $\alpha/2$ from the instrument axis. The color coding is *roughly* the relative weight of each ray coming to the focus; blue having low weight and red having high weight.

ning a single facet. The length of the chord is

$$x = 2R_C \sin \alpha/2 = 2R_F \sin \alpha'/2 \tag{24}$$

From the construction one can determine that

$$\Delta R = \left(R_C^2 - \frac{x^2}{4}\right)^{\frac{1}{2}} - \left(R_F^2 - \frac{x^2}{4}\right)^{\frac{1}{2}} \tag{25}$$

This is simply a statement that ΔR is given by the distance from the frame origin of curvature to the chord minus the distance from the facet origin of curvature to the chord. For R_C=750 mm and R_F=730 mm (the case for LEXI) ΔR=20.000077 mm.

Now we consider the light coming from a source at an angle $\alpha/2$ from the instrument axis, which is in the direction of the junction of the two facets. The two green (heavy black) lines in the top (bottom) panel of Figure 35 indicate the undeflected ray from that direction for both facets. The intersection of this ray with the focal surface (shown as the dotted red curves) indicates the places that the source is focused by the two different facets. There is not a nice way of representing the distance between these points. (One can calculate the (x, z) location of the origins of curvature, and the the locations of the foci with respect to those positions, but that does not produce a terribly nice formula.) For the LEXI case the distance between the foci is 1.093 mm, or 10.″01 (roughly the size of the PSF), but those spots are significantly above the designed detector plane.

What we see from Figure 35 is that if you follow the bundle of the most heavily weighted rays, the ray bundles from the two facets do converge at some distance below the individual foci where, of course, both bundles have diverged significantly. One can estimate where that convergence will be; the peak of the weighting will occur Γ_0 closer to the center of the facet axis than $\alpha/2$. This leads to a messy formula for the distance of that convergence from the origin of the frame curvature:

$$R'' = \frac{C \sin\left(\Gamma_0 - \arcsin\left(\Delta R \sin\left(\alpha/2\right)/C\right)\right)}{\sin \Gamma_0} \tag{26}$$

where

$$C = \left(\Delta R^2 + \left(\frac{R_F}{2}^2\right) + R_F \Delta R \cos\left(\alpha/2\right)\right)^{\frac{1}{2}} \tag{27}$$

For LEXI, the convergence of the most strongly weighted bundles is 357.5 mm from the origin of curvature for the frame or 392.5 mm from the optic. This is slightly more that we measured at PANTER (see Figure 36) but, given our rather simple assumptions about which part of the bundle is important and the fact that the LEXI facets have some intrinsic misalignment, the agreement isn't too bad.

5.4. *Misalignment vs. Mismatch*

The frame/facet mismatch produces one focus spot per facet. Similarly, the misalignment of facets will produce one focus spot per facet. Can one distinguish between frame/facet mismatch and a misalignment? Consideration of Figure 35 suggests that we *might* see a difference between the two cases since the focal lengths are different.

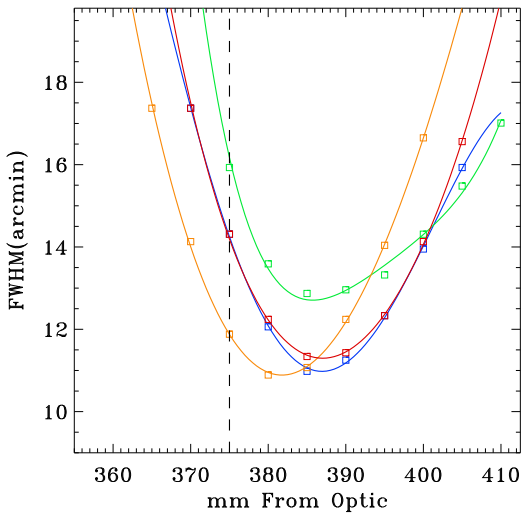

Figure 36. The size of the PSF as a function of optic-detector separation for beams towards the corners of the central facet of LEXI. The data (boxes) and fits are shown for each of the four corners.

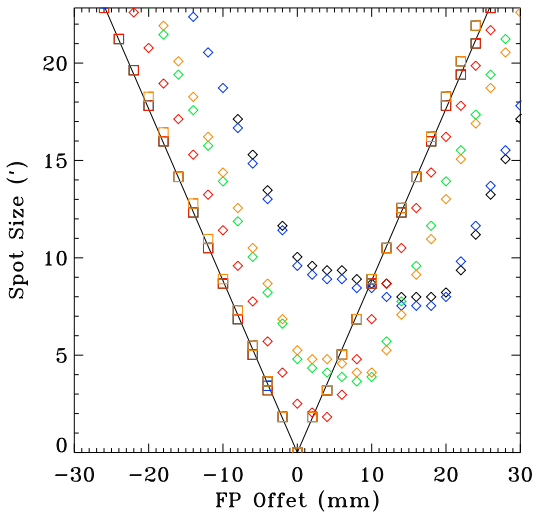

Figure 37. Spot size as a function of focal plane distance when the optical axis is placed at the boundary of two facets. The solid line shows the expected behavior for a properly aligned optic. The spot size perpendicular to the axis of the two facets is plotted as boxes. The spot size along the axis of the two facets is plotted as diamonds. *Black:* Two facets having R_F=730 mm in a frame with R_C=750 mm. *Blue:* Two facets having R_F=R_C=750 mm where one facet has been misaligned by 4.′58 along the axis linking the two facets. The angle is away from the other facet. *Green:* The same as the previous case but with a misalignment of 2.′29. *Red:* The same as the previous but with a misalignment of 1.′15. *Orange:* See text.

We consider two adjacent facets, and misalignment *only* along the axis between the two facets. (Misalignment in the perpendicular direction would be immediately obvious.) We simulated[15] two facets with R_F=730 mm set in a frame with R_C=750 mm. We measured the angular distance between the two spots in the frame's focal plane, 4.′58. We then simulated two facets with R_F=750, but misalignment of 4.′58. We simulated the image in a series of focal planes with distances both shorter and longer than the ideal facet focus. This means that for the frame/facet mismatch series is centered 365 mm while the misalignment series is centered on 375 mm. For each focal plane distance we measured the "spot size" both along the axis linking the facets and axis perpendicular to that. Given that the "spot" is likely to be two spots, we defined the spot size along a given axis, to be the size of the interval containing greater than 15% of the peak flux.

The above test is to see if one can distinguish between the two cases when the spot separation in the design focal plane is the same. We find that there is no significant difference in the spot size as a function of focal distance between the frame/facet mismatch and the facet misalignment. Close examination of the cross section of the spots show that there *are* differences, the subspots for the mismatch contain more flux than the subspots for the misalignment for intrafocal distances, and the reverse is true for extrafocal distances. However these differences are likely to be too small to be detected with real devices.

In practice, one might be dealing with both phenomena simultaneously. In Figure 35, the red curve is a simulation where the facets have R_F=730 mm and are set in a frame with R_C=750 mm, and the side facet is misaligned by 2.′29, putting it's focus closer to that of the other facet. You can see that configuration is very similar to that with no frame/facet mismatch, and only a 2.′29 misalignment away from the other facet.

Lessons learned: Make sure that you measure the radius of curvature for each optic before you machine the frame in which they are to sit. Make sure you understand the metrology of your frame. That way the ambiguity between frame/facet mismatch and misalignment can be avoided.

5.5. *Further Considerations Concerning Mismatches & Misalignments*

Consider an on-axis source, where the optical axis passes through the center of a facet. One can determine the relative amounts of flux transmitted by that facet and the surrounding facets. Clearly, the fraction of the flux transmitted by the central facet decreases as R_C increases. It is also clear that the fraction of the flux transmitted by the central facet decreases as the energy decreases.

Figure 38 shows the fraction of the fully, partially, and non-focussed flux transmitted by the center facet, the facets sharing an edge with the central facet, and the facets diagonally adjacent to the center facet, as a function of energy. For a LEXI style optic with R_C=750 mm, at low energies only ∼40% of the focussed flux is due to the center facet; roughly the same amount is contributed by the two facets to either side and the facets above and below. Thus, over half of the flux in the core of the PSF is contributed by facets that may be misaligned with the center facet. For a STORM style optic with R_C=1000 mm, the situation is even worse, only ∼20% of the flux is from the center facet; the bulk of the flux is due to focussing by the surrounding facets. **Thus, alignment of the facets is exceptionally important at lower energies, particularly at longer R_C.**

[15] Simulations made with *PBP4* for LEXI testing at PANTER.

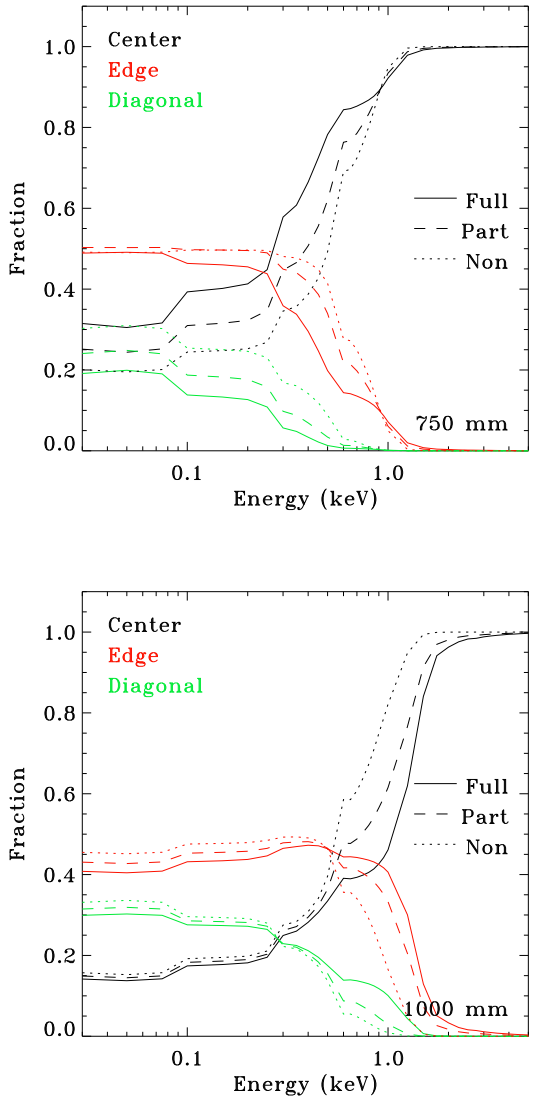

Figure 38. The fraction of the fully (*solid line*), partially (*dashed*) and non-focussed (*dotted*) flux transmitted by the central facet (*black*), the facets sharing an edge with the central facet (*red*), and the facets diagonally adjacent to the central facet (*green*). *Top:* for a R_C=750 mm optic *Bottom:* for a R_C=1000 mm optic. In both cases W/L=0.02 and the facet is 40 mm by 40 mm.

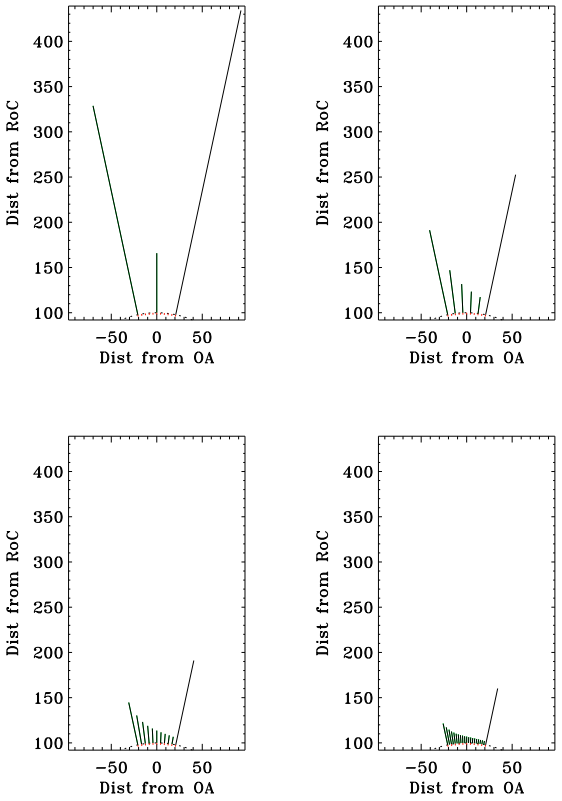

Figure 39. Increasingly reasonable designs for the STORM sunshade with internal baffles. The Earth is to the left and the Sun is to the right. In each case, the curve at the bottom of the plot is the surface of the optic.

6. SHADES & BAFFLES

There are two separate issues to be considered here, the sunshade which surrounds the optic, and the interior baffles which, at least ideally, run between rows or columns of facets[16]. We will consider primarily the baffles, as the mathematics for the sunshade are similar. For the baffles, we want the fins to be perpendicular to the local surface in order to minimize shadowing. It is anticipated that the interior baffles will need to run in only a single direction, which is perpendicular to the Earth-Sun line.

Figure 39 shows a series of designs for the STORM sunshade with interior baffles. This sunshade was designed for staring at the nose of the magnetosheath when the Earth is 6.5° from the optical axis and the Sun is 56.5° from the optical axis. For many applications, running baffles only along the facet boundaries is insufficient to produce a short enough sunshade. Baffle fins for LEXI have to be spaced at $\frac{1}{3}$ facet intervals in order for the sunshade to be short enough, while STORM could cope with baffle fins spaced at $\frac{1}{2}$ facet intervals. Thus, concerns about the interaction of tiling and the baffle fins are, to some extent, otiose.

6.0.1. *Throughput*

[16] The calculation of the lengths of the sunshade and baffles are not covered here but is in a separate document. We will assume here that there are no reflections from the baffles.

Calculating the reduction in throughput is really the point of simulation. However, some though experiments can provide some useful understanding. First, remember that the baffles run in only one direction, so the problem can be worked in a single dimension. We will consider two situations; one where the optical axis in on a baffle fin, and a second where the optical axis is intermediate between two fins. In both cases the R_C of the optic and the angular separation of the fins is kept constant. Given that only a limited area contributes to the focussing, and given that the baffle fins are perpendicular to the surface of the optic, we expect expect the amount of shadowing to non-negligible, but small.

Our example in Figure 40 is the R_C∼1000 mm STORM optic, where we've chosen a representative length (100 mm) for the baffle fins. The curve at the bottom of each plot is the surface of the optic, and we have shown either two or three baffle fins. The dashed red lines are parallel to the optical axis; the parts of the optic between the dashed red lines and the nearest fin are shadowed. The blue lines mark the location Γ_0 where fraction of singly reflected rays peak. We can see that a source parallel to a baffle fin is focused primarily by the part of the optic that is near the shadow cast by the next baffle fin. However, it is a relatively small area that is being shadowed. The situation is even better for a source half-way in between two fins. Here the amount of the optic that is shadowed is smaller, and the region being shadowed contributes less to the focussing of the source.

We thus expect the baffle fins to introduce a periodic variation in the effective area. Since longer fins shadow more area, we expect the overall vignetting function to be asymmetric. Figure 41 shows how the vignetting function changes as the number of fins is increased for the STORM optic. It should be noted that the way that one describes the loss of effective area is important. For example, one would cite very different numbers if one were considering only a source on-axis, an extended region surrounding optical axis, or one is considering the overall effective area of the instrument.

6.0.2. *Simulator Implementation*

We wish to determine the shadow cast on the optic by the baffle fins given a uniform light source in the direction $\vec{B} = [b_x, b_y, b_z]$. It is assumed that the baffle fin is planer, tilted with respect to the optical axis by an angle θ at x=0, and that the top edge of the baffle fin is defined by some function $f(y)$. The simplest solution is to calculate for a pore at a the location $[a_x, a_y, a_z]$, whether a ray starting at that location and pointing towards the light source intersects the fin above or below its outer edge. That is, we solve:

$$\vec{A} + L\vec{B} = [x\cos\theta, 0, z\sin theta] \tag{28}$$

or

$$L = \frac{a_x\cos\theta - a_z\sin\theta}{b_z\sin\theta - b_x\cos\theta}. \tag{29}$$

The point of intersection is then $[a_x + Lb_x, a_y + db_y, a_z + db_z] = \vec{I}$, and one can determine if the pore is shadowed

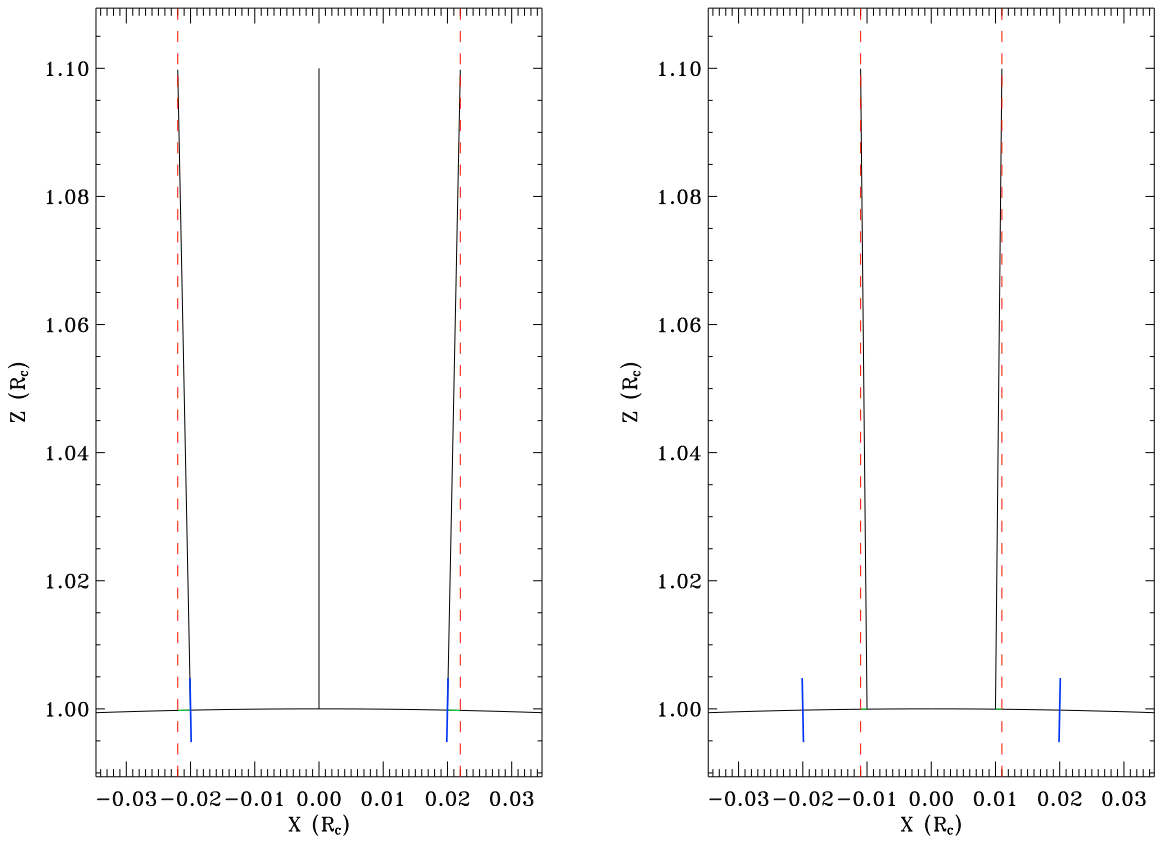

Figure 40. Demonstrating the two extremes of shadows cast by baffle fins. The curve at the bottom is the surface of optic. The *blue lines* mark the location where the fraction of singly reflected rays peak. *Top:* A fin is pointed directly towards the source. *Bottom:* The source direction is halfway between two fins.

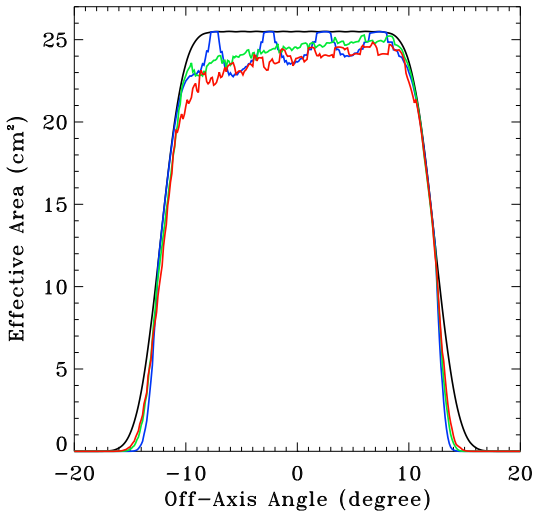

Figure 41. Demonstrating the two extremes of shadows cast by baffle fins. The curve at the bottom is the surface of optic. The *blue lines* mark the location where the fraction of singly reflected rays peak. *Top:* A fin is pointed directly towards the source. *Bottom:* The source direction is halfway between two fins.

if

$$\sqrt{I_x^2 + I_y^2 + I_z^2} > R_C \text{ and}$$
$$\sqrt{I_x^2 + I_z^2} < f(I_y) \tag{30}$$

We have generally assumed that the top edge of the baffle fin is straight. This means that the fin is longer at large $|y|$ than it is in the middle of the optic. One could well image employing baffle fins whose top edge has a constant distance from the optic radius of curvature. There is more work to be done here to understand to what design is optimal. Thus, only the straight edged baffle fins have been implemented thus far.

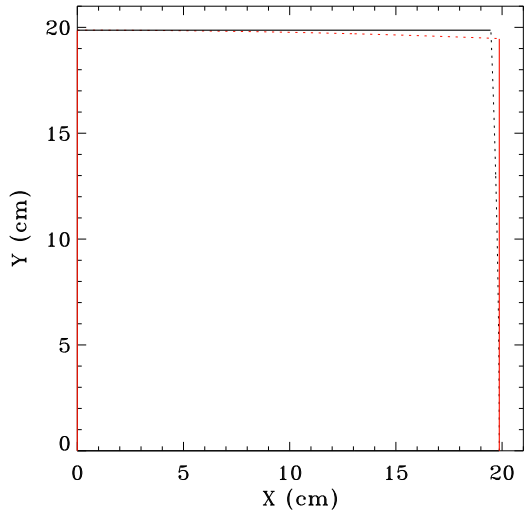

Figure 42. A pointless(?) demonstration of the incommutable nature of rotations. The solid black line traces an $\hat{x}$ rotation by ϕ followed by a $\hat{y}$ rotation by ϕ as projected into the xy plane. The solid red line traces an $\hat{y}$ rotation by ϕ followed by a $\hat{x}$ rotation by ϕ as projected into the xy plane. Here $\phi = 11\overset{\circ}{.}46$, which is the size of the upper quadrant of the STORM optics in the absence of support structures and the like. The dashed lines are lines of constant longitude for the poles in the direction of $\hat{x}$ and $\hat{y}$.

7. SMPO SIMULATOR IMPLEMENTATION

The calculation is done on a facet-by-facet basis, and for a given facet it is done on a pore-by-pore basis. In the current implementation the ray exiting the pore is assumed to exit the center of the pore, a simplification that may cause problems when attempting to model higher angular resolution optics. Most of the following is just thinking in text.

There is the fundamental problem that a $\hat{x}$ rotation by ϕ followed by a $\hat{y}$ rotation by θ is not the same as a $\hat{y}$ rotation by θ followed by a $\hat{x}$ rotation by ϕ. Thus we must set a convention for the order. It seems most natural to set the longitude to be in the $\hat{x}$ direction and latitude in the $\hat{y}$ direction.

7.1. *Algorithm*

7.1.1. *Calculate the location and rotation of the facet*

Presumably, we can denote each facet by the longitude and latitude of its center, and we can assume that the $\hat{y}$ axis of the facet is a line of constant longitude. We assume the maximal packing of square facets, with indices $ii = 0$ to N in the $\hat{x}$ direction and $jj = 0$ to N in the $\hat{y}$ direction. The facet centers will have latitudes

$$\psi_{mid} = \left(\frac{N}{2} - 0.5 + ii\right)\frac{F}{R_c}. \tag{31}$$

Their longitudes ϕ are set by the closest possible packing at the latitude

$$\psi_{ext} = \psi_{mid}(1 + 0.5\frac{\psi_{mid}}{|\psi_{mid}|}) \tag{32}$$

and thus the longitudes of the middle of the facets are

$$\phi_{mid} = \left(\frac{N}{2} - 0.5 + jj\right)\frac{F}{R_c\cos(\phi_{ext})}. \tag{33}$$

And then

$$x_{mid} = R_c\sin(\phi_{mid})\cos(\psi_{mid}), \tag{34}$$
$$y_{mid} = R_c\sin(\psi_{mid}), \tag{35}$$
$$z_{mid} = R_c\cos(\phi_{mid}).\cos(\psi_{mid}) \tag{36}$$

The rotation of the facet, for an ideal instrument, is taken care of by requiring that the $\hat{y}$ axis of the facet be aligned with line of longitude running through the center of the facet. We should probably include the capability of adjusting the rotation in order to take installation tolerances into consideration.

7.1.2. *Calculate the location and rotation of the pore*

The location of the corners of the pores is given by the mesh algorithm/code described in Appendix D. Since the deformations are relatively small, we may (or may not) ignore the effect of the deformation on the fraction of the pore with n versus $n+1$ reflections. However, we want to capture the effect of the deformation on the location that the reflected beam intersects the detector plane. To do so, we will need the location of the pore, $[x, y, z]$, the magnitude of the acute angle of the pore walls, γ, and the overall rotation of the pore, η.

7.1.3. *Calculate the shadowing by the support structure, the shades, and the fins*

Once the array of the individual pores in a facet is set up, a *shadow_mask* is created to determine which pores will not be exposed to light, or are otherwise blocked.

The pores sitting on the support structure will not transmit. In the old implementation, the gap between facets has been added to the size of the facet, but blocked out. It is not clear how this is (to be) handled in the new implementation.

The pores sitting directly underneath a fin should be blocked out. In the current implementation, the fin is assumed to be 1 mm wide.

Pores can be shaded by the fins. This depends upon the direction of the light source. The calculation of this is sketched in the previous section.

7.1.4. *Calculate the fractions in each output beam*

For each pore, one knows that angle from the optical axis in both the x and the y direction, (Γ_x, Γ_y). Thus one can calculate

$$n_{min}(x,y) = \text{Int}\left[\frac{L}{W}\tan(\Gamma_x, \Gamma_y)\right] \tag{37}$$

and the fraction of light suffering (n_{min}, n_{max}) reflections in a single direction is

$$f_{min} = \frac{L}{W}\tan\Gamma_i - \text{Int}\left[\frac{L}{W}\tan(\Gamma_x, \Gamma_y)\right]$$
$$f_{min+1} = 1 - f_{min} \tag{38}$$

Thus, for every pore there are precisely four possibilities[17]

$$\begin{matrix} f_{x,min}f_{y,min} & f_{x,min+1}f_{y,min} \\ f_{x,min}f_{y,min+1} & f_{x,min+1}f_{y,min+1} \end{matrix} \tag{39}$$

[17] This is true for a square pore, but not for non-square pores. We have not yet begun to fight that battle.

7.1.5. *Calculate the landing spot of each beam*

For each of those possibilities, one must determine the landing spot on the detector of that ray. This problem can be divided into the two dimensions. If, for a given dimension, n is even, then the output ray has the same direction as the input ray, and we conveniently ignore the fact that the output ray will be slightly offset from the input ray. If, for a given dimension, n is odd, then the input ray of angle β with respect to the optical axis will exit at an angle $\gamma = 0 - (\beta + 2\alpha)$ with respect to the optical axis.

The ray then lands on the detector a distance

$$\begin{aligned} \Delta X &= (Z_{pore} - Z_{det}) \tan \gamma_x \\ \Delta Y &= (Z_{pore} - Z_{det}) \tan \gamma_y \end{aligned} \tag{40}$$

from the optical axis in that dimension.

Thus, it is relatively trivial to vary to height of the focal plane in order to understand what happens when the instrument is out of focus. We have not implemented a curved focal plane as no curved detectors are yet available.

Note that to imitate the effect of bias or facet misalignment, one can simply modify (α_x, α_y), perhaps as a function of position. If one had a function for the pore or pore bundle misalignment, then that distribution could also be incorporated at this point.

The one thing that can not be easily implemented in this scheme is the effects of pores that are not square. Sufficient thought on this problem has simply not yet occurred.

7.2. *Post Simulation*

Often, the whole point of the simulation of an instrument is to produce a simulation of an observation with that instrument. For each location on the sky, you need the flux from the sky, the instrumental effective area in that direction, and the instrumental PSF in that direction. Each location on the sky can be thought of as projecting its PSF onto the detector. This means that the count rate in a pixel of the detector is the sum, over all locations in the sky, of the product of the sky flux at that location and the appropriate element of the PSF at the location. This *would* be a convolution *if* the PSF did not vary with location. The variation of the PSF with location makes image construction more complicated.

In order to make the exposition as simple as possible, consider the problem in one dimension. Let us assume that the detector pixels, i, are spaced uniformly, and that we have calculated the PSF for each pixel, and that the PSF has been calculated at the same grid spacing as the detector pixels. An example, showing the PSF for every tenth pixel, is shown in the lower panel of Figure 43. Note that each physical detector pixel corresponds to a particular angle from the optical axis. (In the above mentioned figure, the x-axis is linear in pixel number, and non-linear in angle.) The output image is the sum of these PSFs, weighted by the brightness of the sky in the direction of the PSF center. That formulation considers the output image to be the sum of the projections from each part of the sky. Conversely, the flux in detector pixel i is

$$\sum_{j=-\infty}^{j=\infty} PSF_{i+j}(-j) I_{i+j} \tag{41}$$

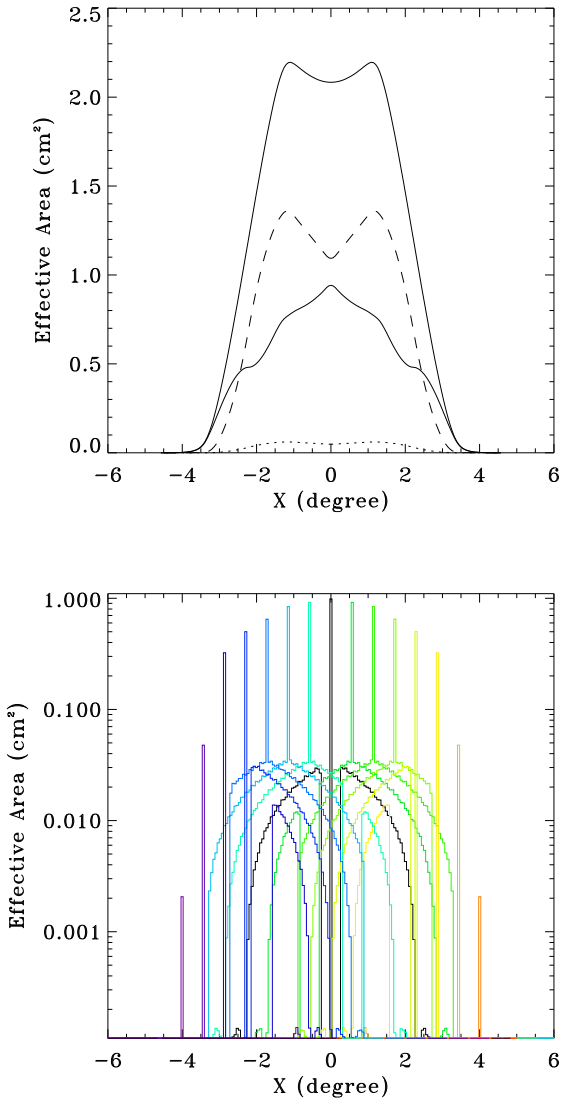

Figure 43. The vignetting functions and PSFs for the one-dimensional demonstration of image construction. **Top:** The *upper solid curve* is the total vignetting function. The remaining curves show the vignetting for each of the PSF components, *dotted* is the unfocussed photons, *dashed* is the partially focussed photons, and *solid* is the fully focussed photons. **Bottom:** The PSF at the location of every tenth pixel. The on-axis PSF is shown in black. Note the logarithmic scale.

where $PSF_{i+j}(i-j)$ is the PSF for a location an angle $i+j$ from the optical axis evaluated at an angle $-j$ from its center, and I_{i+j} is the input sky flux an angle $i+j$ from the optical axis. However, since the simulator produces the PSFs, gridded in the detector coordinates, it is usually most simple to think of the output image as the sky weighted sum of the PSF [18].

Since the PSF changes with location, one needs a very large number of PSFs is required to correctly simulate an output image. For an ideal SMPO, the PSF does not change with location. (ignoring the effects of the

[18] I cheated when creating these PSFs. They are *not* the PSF from a true one-dimensional detector. Instead, the PSFs used below are just the central strip from a two-dimensional PSF, which means that the fully focussed photons are over represented.

deformation of the pores in the corners of the facets, etc..) However, the support structures and, more importantly, the edges of the optic, do change the PSF as a function of position. The question becomes whether one can use a combination of the on-axis PSF and the map of the effective area (otherwise called the vignetting function) to *approximately* simulate an output image.

We note that the PSF consists of a strong central peak, and much lower, though quite broad wings. The strength of the central peak compared to the wings suggests that the output image is probably not sensitive to the details of the wings. (Such suggestions are often wrong!) We can try replacing the correct PSF with a shifted copy of the on-axis PSF, scaled by the vignetting function. We'll call this a "constant PSF approximation".

Figure 44 shows output images where the input image had a uniform surface brightness with a single "point source". In one case this source has been placed in the center of the FOV, while in the other it was placed at the edge of the FOV. The black curve is the correct simulation where the correct PSF has been used for every point. The red curve is a simulation where the on-axis PSF was shifted and scaled by the local vignetting function. The red curve is good at the center of the FOV, but gets the overall vignetting incorrect. Note that this method does not get the point source correct when it is no longer in the center of the FOV, though it does better than the next several methods.

Since we have approximated the PSF with a constant shape, but variable normalization, one might wonder if a convolution might work; convolve the input with the on-axis PSF, and then multiply the result by the vignetting function. This method is shown by the purple curve (which is usually the same as the blue curve). It gets the vignetting mostly correct (it would have to!) but it gets the point source strength substantially incorrect. Can I explain this?

One might attribute the error in our first approximation to the fact that the relative strengths of the core, the arms, and the unfocussed components vary with off-axis angle. We have applied the constant PSF approximation to each of these components separately. The result is the green line. It does better than convolution for the point source, but gets the vignetting even more badly incorrect. Finally, one could attempt to do the convolution, but for the three components separately, but that produces nearly the same result as using convolution on the total PSF, as one might expect.

Having found that nothing really works as well as using the location specific PSF, let us note that the problems occur when the local vignetting function is not flat. So if we created a SMPO with an extended flat FOV, then most of these issues would not arise until we got to the edge of the FOV. However, if one is interested in building up the FOV from modules, creating the observation simulation remains somewhat problematic.

7.3. *Accelerating Executions*

One of the wisest decisions made for PBP was to allow the user to set the step between pores. That is, does one want to calculate every single pore? Or is every other pore, every fourth pore, or every eighth pore sufficient? Table 2 list the execution time for simulations of a single R_C=1000 mm face for 18 different energies, as run on my current laptop. As expected, the execution time increases at almost the same rate as the increase in the number of pores calculated. The fractional uncertainties increase with step size, and are larger for fully focussed rays than partially focussed rays or unfocussed rays. It appears that a step size of 4 provides reasonable accuracy while still decreasing processing time.

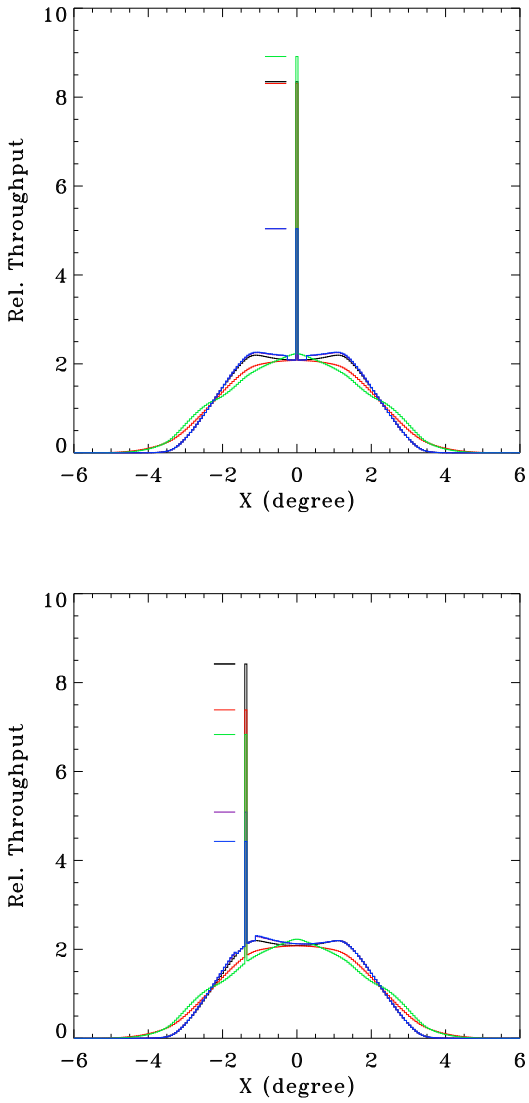

Figure 44. Demonstration, using a one dimensional optic and detector, of the limitations of approximating the true PSF by a single PSF and the vignetting function. **Left:** The output for a flat input with a source at the center. *Black:* the correct image *Red:* image created from the vignetting scaled on-axis PSF *Purple:* image created by convolving the on-axis PSF with the image and then multiplying by the vignetting function *Green:* image created from the vignetting scaled on-axis PSF, but done on a component by component basis (unfocussed, partially focussed, and fully focussed) and then summed *Blue:* the convolution method done on a component by component basis. Tick marks have been placed at the peak of the point source for each method. **Lower Right:** Same as the previous, but for an input image with an off-center source.

7.4. *Input Parameters*

All versions require one to set:

- R_C

Table 2
Relative Execution Times[a]

Version	Step	Time (sec)	ΔE.A.[b]
PBP3	8	8	5.41e-3
PBP3	4	28	9.38e-5
PBP3	2	108	8.62e-5
PBP3	1	419	-
PBP3b[c]	8	9	9.03e-4,5.93e-3,1.15e-2
PBP3b[c]	4	30	1.81e-5,3.83e-5,3.85e-3
PBP3b[c]	2	109	3.42e-6,5.98e-6,3.16e-3
PBP3b	1	431	-,-,-
PBP4	8		
PBP4	4		
PBP4	2		
PBP4	1		

[a] For a single 40 mm by 40 mm facet and 18 energies.
[b] The value given is the maximum absolute value of the difference between the total transmitted flux calculated with a given step size and that calculated for a step size of 1, divided by that calculated for a step size of 1. (So, the fractional error.)
[c] For PBP3b, the PSF image is separated into unfocussed, partially focussed, and fully focussed images. The uncertainties are for each image, in this order.

- Pore width (W), pore length (L), and pore wall thickness.
- Size of the facet. If there is a gap between facets, the width of that gap must be added to the facet size.
- The width of the gap between facets and the amount of the facet resting on the support.
- The number of facets in x and y.
- Whether each facet is open or closed. (Closed are facets that are blanked off.)
- The vector of energies to be calculated.
- The name of the file containing the reflectivity information.
- The function that creates a mask to map which pores are blocked or shadowed.
- The parameters describing the sunshade baffle locations and sizes.
- The height of the detector above the nominal $R_C/2$.
- The pixel size of the detector. The program will ensure that the output array is big enough to include all rays transmitted by the optic.
- The detector mask function; essentially the function that sets the region to be "active" or "blocked".
- The angles from the optical axis of the source (β_x, β_y).
- The step size between calculated pores.

7.5. *Versions*

PBP3: This is the basic version of the software.

PBP3B: PBP3 but with the PSF image split into three planes: non-focussed rays (0), partially focussed rays (1), and fully focussed rays. This may be an evolutionary dead-end.

PBP3A: PBP3 but with the PSF image split into planes, each plane containing only rays having had a total of n reflections. This version of the code no longer exists, but could be resurrected.

PBP4: PBP4 requires the following further paramters to be set

- Maps of the bias angles in x and y for each facet.
- Maps of the misalignment angles in x and y for each facet.

PBP5: PBP5 is experimental. It introduces a "distortion map" that should contain the information about the change in bias across a single facet.

7.6. *Data Structures*

For the instrument as a whole, there are a number of arrays that describe the properties of each facet. For a facet, there are a number of arrays that describe the properties of each pore. As the program handles more complex issues, the number of arrays increase (and the processing time increases!)

The facet arrays for PBP3:

- open_map: contains a 1 for every populated facet and a 0 for every blanked-off facet.
- alpha_x_cen_map: contains the off-axis angle in x at the center of each facet.
- alpha_y_cen_map: contains the off-axis angle in y at the center of each facet.

The facet arrays for PBP4:

- open_map: contains a 1 for every populated facet and a 0 for every blanked-off facet.
- alpha_x_cen_map: contains the off-axis angle in x at the center of each facet.
- alpha_y_cen_map: contains the off-axis angle in y at the center of each facet.
- bias_x_map: contains bias angle in x. Positive values are
- bias_y_map: contains the bias angle in y. Positive values are
- misa_x_map: contains the misalignment angle in x. Positive values are
- misa_y_map: contains the misalignment angle in y. Positive values are

The pore arrays for PBP3. In this version the pores are all assumed to be square. Thus:

- shadow_mask: each elements contains a code for a single pore.

  - 1: the pore is open
  - -1: the pore is blocked by the support structure
  - -2: the pore is blocked by an internal baffle (i.e., the baffle is effectively on the optic at that pore).
  - -3: the pore is in the shadow cast by the external shade or an internal baffle
  - -4: the pore is blocked by the external frame

The pore arrays for PBP4 are as for PBP3. The pore arrays for PBP5 will be more extensive as they will attempt to capture the slumping deformation. There will probably be pore arrays describing

- the x and y location of the corner of the pore closest to the center of the facet. This is to adequately characterize the movement of the pore due to the deformation.
- the angle between the walls of the corner of the pore closest to the center of the facet. This should always be an acute angle.

I hope to convert these into an array that describes the *changes* in the $\hat{x}$ and $\hat{y}$ location of the output ray's intersection with the focal plane. It remains to be seen how this should be best accomplished.

8. SMPO TESTING CONFIGURATIONS

8.1. *Introduction*

There are three possible MPO test configurations, which are shown in Figure 45. The first configuration (A) is a traditional beamline where the source is sufficiently far from the optic that the divergence of the beam is relatively small, and the detector is placed at the focus of the optic. This configuration requires long beamlines and, typically large chambers that require an extended time to be evacuated to the required pressure for X-ray testing. The second configuration (B) is the reverse of the beamline configuration, where the source is placed at or near the focus of the optic, and the detector is placed in the collimated beam. This can be accomplished with a chamber that is only somewhat larger than the radius of curvature of the optic. Such a chamber can be evacuated relatively quickly, and thus is ideal for the quick testing of individual facets. Further, the entire test rig is relatively compact and portable. This is true perhaps more in theory than in current practice. Finally, there is the "double-reversed" configuration (C), where the source is placed only a short distance in front of the optic, and the detector is placed at or near the focus. This configuration has not be explored in the same detail as the other two. This section of the *vade mecum* will consider the mathematics of reversed- and double-reversed beamlines, as the optics of the beam line are relatively well understood.

There are three things that we want to determine from testing an SMPO optic. 1.) We want to determine, if possible, the true radius of curvature, R_C. 2.) We want to determine the open fraction, the throughput of fully focussed rays, and the throughput of partially focussed rays. 3.) We want to measure the size of the point spread function (PSF). While all of these can be accomplished in a beam line with the beam illuminating the whole optic, none of these can be accomplished for the reverse beamline and double reverse beamline configurations if the illuminating beam fills the optic. For the reverse and double reverse beamline configurations, all three measurements may be accomplished with an appropriate mask. At minimum, the mask must have a hole on the optical axis (the "central" hole) and a hole off axis (the "peripheral" hole). Measuring the location of the off-axis spot compared to the on-axis spot allows one to determine the radius of curvature, R_C. The size of the spots allow a measure of the PSF. The relative count rates of the spots allow a measure of the throughput[19].

The following subsections will (when they are complete) derive the equations for determining the radius of curvature (R_C) when the mask and optic is a known distance Z_S from the source and a known distance Z_D from the detector. It is assumed that the optic has a half-width of X_F so that the distance from the optical axis to a corner, where the optic rests on the mask or reference plane is $X_F\sqrt{2}$. There are two pin-holes in the mask: one on the optical axis, and the other at a distance $X_M\sqrt{2}$ from the center along the diagonal. We should choose X_M so that, when the source is in the fo-

[19] This statement is true in theory. However, the uncertainties is the current test set-up make the PSF and throughput measurements difficult.

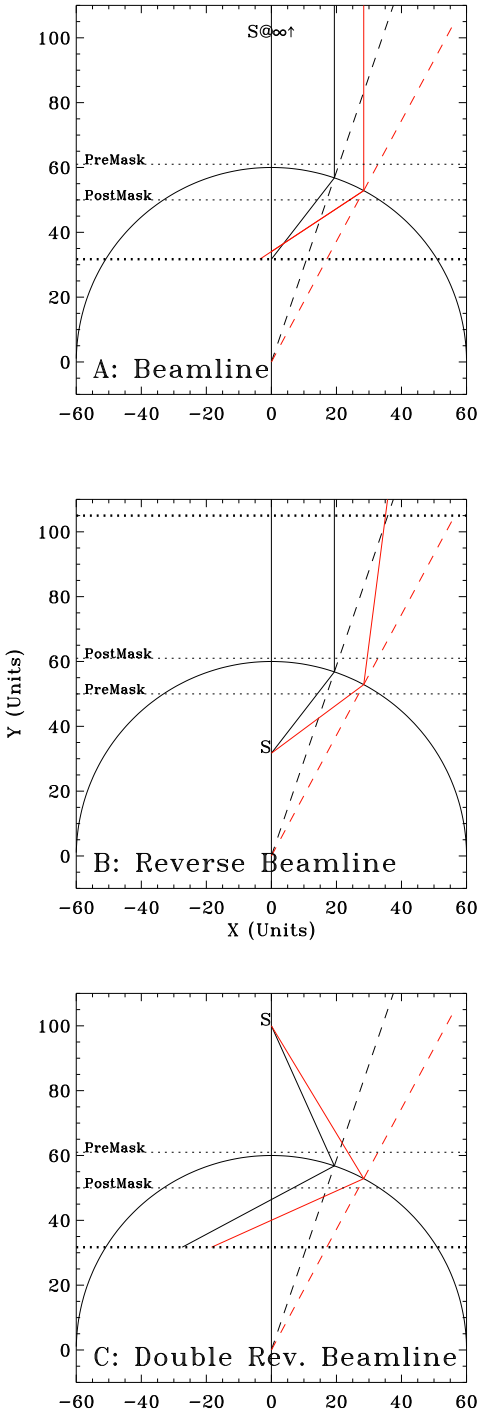

Figure 45. Three possible testing configurations for an MPO. In all cases the solid curve is the optic, the thick dotted line shows the detector plane, the thin dotted lines are possible mask locations, and the solid line are rays. The dashed lines are radii perpendicular to the surface of the optic. S is the location of the source. A: The standard beamline configuration, with a source at "near infinity" and the detector plane at the focus. B: The reverse beamline configuration, with the source at the focus. C: The "double reverse beamline" has the configuration as a beamline, but with a source close to the optic. In all cases a mask can be introduced either between the source and the optic (a premask) or between the optic and the detector (a postmask).

Table 3
Reverse Beamline - Premask Variables

Symbol[a]	Explanation
E	distance from mask to optic on the optical axis
F	focal length
$F\prime$	$R_c - F$
G	distance from source to center of curvature
L	length of an individual pore = thickness of the optic
R_c	Radius of curvature
W	width of an individual pore
X_D	off-axis beam spot on the detector
X_F	radius of the facet
X_M	distance from the optical axis of pin-hole in mask
Z_D	distance from the mask to the detector
Z_S	distance from the mask to the source
α	angle from OA of reflecting pore wall
β	angle from OA of ray from source

[a] Quantities in red are those that are either known or measured directly.

cus, all rays passing through the hole will, upon striking the optic, experience a single reflection in each dimension. However, we may not have that option as we need to ensure that the X-rays from the peripheral spots are reflected onto the detector, and detectors are typically not very large. Thus, in the following derivation, X_M is assumed to be known, but not assumed to have any special value. Finally, it is assumed that one can measure the distance at the detector, between the centers of the spots produced by the two pin-holes, $X_D\sqrt{2}$.

Typically, given the radius of curvature of the facet, the Z_S, and Z_D, one would calculate what X_M is required to fit the peripheral spot onto the detector. Using a mask with that X_M, we would then measure X_D and, with Z_S and Z_D, would calculate R_C. The following derivations will demonstrate how to derive R_C from X_D given all of the other parameters. In most cases there are no closed solutions and we must rely on numerical methods.

For both the reversed beamline and double-reversed beamline configurations one can, in principle, place a mask in the beam either before it strikes the optic, a "premask", or after striking the optic, a "postmask". It is not always apparent which placement is best for determining the radius of curvature, R_C. For both of these configurations the location of the mask makes a large difference in the complexity of the mathematics, but changes the X_D-R_C relation in only a small way, so long as the mask is relatively close to the optic. Thus, we have four different configurations to consider.

8.2. *Reverse Beamline Configuration Testing with Premask*

In this configuration the source is placed at or near the focus of the optic on the concave side of the optic, while the detector is placed on the opposite side of the optic. The detector is thus on the side of the optic where the rays are quasi-parallel. It is assumed that the corners of the concave side of the optic rest upon a mask.

Figure 46 demonstrates the general geometry of the pre-mask reverse beamline configuration as a cross section through the optical axis and one of the principle axes of the optic. The black lines demonstrate the geometry for a perfect optic for which the source is at the focus, while the red and green curves show two other optics with shorter radii of curvatures, mounted in the same configuration. That is, each of the optics is resting on the mask in the corners. The horizontal dotted line marked "MASK" represents the mask upon which the optic rests, and is the fundamental reference surface. The dashed vertical line shows the distance from the optical axis to the corner of the optic, while the dotted vertical line shows the distance from the optical axis to the edge of the facet.

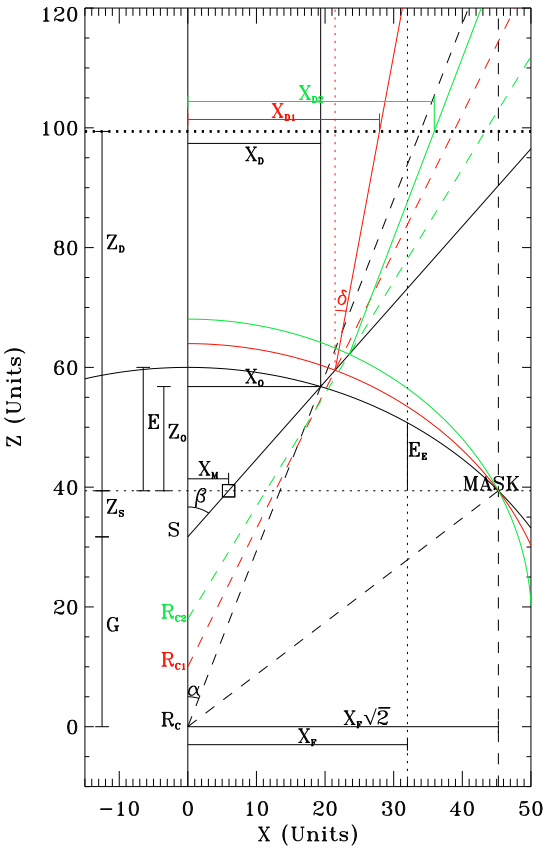

Figure 46. Reverse beamline configuration geometry for a pre-reflection mask. The detector plane is shown by a heavy dotted line. The black curve is the location of the optic for a radius of curvature, R_C, centered at the origin. The source is at S, which is the focus for this optic. The mask is at the level of the *horizontal dotted line* marked "MASK"; the other horizontal dotted line shows the level of the corners of the optic. A ray from the source passes through the pin-hole (X_M from the optical axis) and strikes the optic a distance X_O from the optical axis, and is reflected towards the detector. The *red* and *green* curves show two other possible optics for which S is not at the focus, and the resulting optical paths due to a ray through the pin-hole. The *dotted vertical black line* denotes the edge of the optic. In order to make a readable figure, these dimensions do not correspond to any real optics.

Some Geometry: At the center of each side, the optic will not rest on the mask, but will be elevated a distance E_E. We can define the quantity E which is the distance between the top of the mask and the bottom of the optic on the optical axis. From the construction in Figure 46 (we have fudged this a bit to reduce the number of figures) we see that

$$E = R_C - \sqrt{R_C^2 - 2X_F^2} \tag{42}$$

This means at the center line (in either direction), the bottom of the optic will rest a distance E_e above the

mask where

$$E_E = \sqrt{R_C^2 - X_F^2} - \sqrt{R_C^2 - 2X_F^2} \tag{43}$$

Neither of these quantities are easily mensurable, and neither enter the calculations here, but these are useful quantities for laying out the geometry.

Solving for R_C: A ray originating at S at an angle β from the optical axis will strike the optic at the "reflection point", a distance X_O from the optical axis. Ignoring, for the moment, the practical issue of whether that ray actually strikes a reflective surface (as opposed to passing through the optic without striking it, or being blocked by the walls) that reflective surface is at an angle α to the optical axis. The angle between the ray and the reflective surface is $\beta - \alpha$. The reflected ray will be at an angle

$$\delta = 2\alpha - \beta \tag{44}$$

with respect to the optical axis.

Once the Z_D, Z_S, and X_M (and thus β) are set, determining X_D from a given R_C and α is straight forward:

$$\frac{X_D - X_O}{Z_D - Z_O} = \tan\delta = \tan(2\alpha - \beta) \tag{45}$$

However, what we need to do is determine R_C from X_D without any knowledge of X_O, Z_O, or α.

To put it formally, the problem is solved with the following constraints. First, the optic is a section of a sphere. Second, one point on that sphere is where the corner of the facet touches the mask. Third, the second point on that sphere is along the line defined by the source location (Z_S) and the pin-hole in the mask (X_M). Fourth, the relation between α, β, and δ. Finally, the location where the output ray strikes the detector. In practice, we first use the constraints to derive a relationship between Z_O, G, and the other measured quantities. Second, we derive X_D as a function of G. Finally, we used the measured X_D to select the correct G, and from that we derive R_C.

The constraints placed by the two points on the spherical surface of the optic can be expressed as

$$\begin{aligned} R_C^2 &= (Z_S + G)^2 + 2X_F^2 \quad \text{(corner)} \\ &= (Z_S + G + Z_O)^2 + X_O^2 \quad \text{(refl. pnt.)} \\ &= (Z_S + G + Z_O)^2 + (Z_S + Z_O)^2 \tan^2\beta \end{aligned} \tag{46}$$

where the third line is a re-expression of the second line, replacing X_O. Setting these two expressions for R_C equal to one another and rearranging the terms leads to

$$\begin{aligned} 0 &= aZ_O^2 + bZ_O + c \quad \text{where} \\ a &= (1 + \tan^2\beta) \\ b &= 2[Z_S(1 + \tan^2\beta) + G] \\ c &= Z_S^2 \tan^2\beta - 2X_F^2 \end{aligned} \tag{47}$$

which may be solved for Z_O as a function of G. The result is a complete mess, so I'll not reproduce it here. Although there are two roots, only the positive branch is needed. Note, once you have $Z_0(G)$ then

$$X_O(G) = [Z_O(G) + Z_S]\tan\beta] = \frac{(Z_O + Z_S)X_M}{Z_S}. \tag{48}$$

Table 4
Reverse Beamline Premask Errors

Param	True Value (mm)	Delta Value[a] (mm)	Delta X_D
Z_S	330.0	+1.0	1.12%
Z_D	$Z_T - (Z_S + Z_M)$	+1.0	0.09%
X_F	20.0	+1.0	0.06%
X_M	10.0	+0.1	1.00%

[a] Change in the parameters value which produces the change in X_D in the following column. All parameters are varied independently, not simultaneously.

We now derive X_D as a function of G. First, we note that α as a function of G is

$$\alpha(G) = \arctan\left[\frac{(Z_S + Z_O(G))\tan\beta}{G + Z_S + Z_O(G)}\right]. \tag{49}$$

Therefore

$$X_D(G) = X_O(G) + [Z_D - Z_O(G)]\tan(2\alpha(G) - \beta) \tag{50}$$

which is nothing more than a derangement of Equation 45. Then, given the true X_D one can determine what G could produce that value using some kind of root finder. Having selected the correct value of G we can then find that

$$R_C = \sqrt{(G + Z_S)^2 + 2X_F^2} \tag{51}$$

The Uncertainty in R_C: It is not yet clear what limits there are on the precision with which we can determine R_C. We can set up the test rig to have Z_S and Z_D to some uncertainty σ_S and σ_D, which very well may be anticorrelated. Seemingly, the facet size, X_F will also have an uncertainty σ_F. The X_M can be precisely set, though not particularly to the optimal value for the actual R_C.

To understand the uncertainties I have used values from the current test rig. I assumed that $Z_D + Z_S$ is set to 989.887 mm (using the current numbers from Nick Thomas). Then, assuming that R_C truly is 75.0 cm we can

1. Calculate β from X_M.
2. Calculate Y_S, a, $b = f(G)$, and c from β, Z_S, X_F, and G, where we can use $\vec{G}$, a list of likely values.
3. Calculate, successively, Z_O, α, X_D, and R_C. We have to be careful of the order in which we calculate quantities to ensure that we are we do not introduce any assumptions about focussing.)

Using the values for Z_S, Z_D, X_M, and X_F, from Table 4 we can determine the percentage error in X_D given a reasonable input error in each of the input parameters (separately). The values are given in Table 4 and shown in Figure 47, which demonstrates both the overall relation between R_C and X_D and the uncertainties introduced by each parameter. As might have been expected, errors in X_M and Z_S are the most significant. The error introduced by Z_D is much smaller.

Setting X_M: As noted above, one desires to place the peripheral hole far enough from the center that there are a high fraction of reflected photons, but not so far

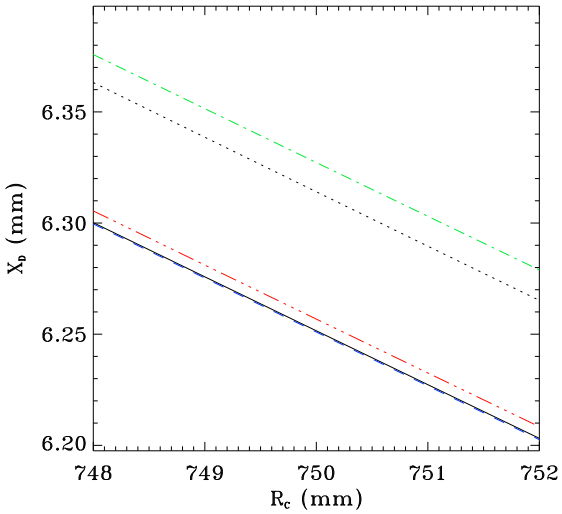

Figure 47. A plot of X_D as a function of R_C for a 750 mm radius of curvature optic. *Blue dashed line:* an error of 1 mm in Z_D (which is nearly indistinguishable from the true X_D-R_C function) *Green dot-dashed line:* an error of 1 mm in Z_S, *Red dot-dashed line:* an error of 1 mm in X_F, *Dotted line:* an error of 0.1 mm in X_M.

out that the reflected spots falls off of the detector. This construction does not provide an easy way of determining X_M, see §8.4 for a reasonable method.

Measuring Throughput: Measuring the throughput requires a simulation of the test rig.This can not be done with the current PBP, but a special implementation of PBP for this configuration is in the works.

Table 5
Reverse Beamline - Postmask Variables

Symbol[a]	Explanation
E	distance from reference surface to optic on the OA
F	focal length
$F\prime$	$R_c - F$
G	distance from source to center of curvature
L	length of an individual pore = thickness of the optic
R_c	Radius of curvature
W	width of an individual pore
X_D	off-axis beam spot on the detector
X_F	radius of the facet
X_M	distance from the optical axis of pin-hole in mask
Z_D	distance from the mask to the detector
Z_M	distance from the mask to the reference plane
Z_S	distance from the mask to the source
α	angle from OA of reflecting pore wall
β	angle from OA of ray from source

[a] Quantities in red are those that are either known or measured directly.

8.3. *Reverse Beamline Configuration Testing with Postmask*

In this configuration the source is placed at or near the focus of the optic on the concave side of the optic, while the detector is placed on the opposite side of the optic. The detector is thus on the side of the optic where the rays are quasi-parallel. It is assumed that the mask is placed nearly on the convex side of the optic. The location of the corners of the facet is an important reference surface.

Figure 48 demonstrates the general geometry of the post-mask reverse beamline configuration as a cross section through the optical axis and one of the principle axes of the optic. The black lines demonstrate the geometry for a perfect optic for which the source is at the focus, while the red and green curves show two other optics with shorter radii of curvatures, mounted in the same configuration. That is, each of the optics is resting on the reference surface in the corners. The reference surface is shown as a horizontal dotted line marked "REF". In all cases, the upper surface of the mask, the horizontal dotted line marked "MASK", is a distance Z_M above the reference surface. The dashed vertical line shows the distance from the optical axis to the corner of the optic, while the dotted vertical line shows the distance from the optical axis to the edge of the facet.

Solving for R_C: As for the previous case, we work from a series of constraints. First, the optic is a section of a sphere. Second, one point on that sphere is where the corner of the facet touches the reference plane, which is at a precisely known distance from the mask. Third, the second point on the sphere is along a line defined by the spot illuminated on the detector and the pin-hole in the mask. Finally, the relation between α, β, δ, and X_D.

The first constraint gives us

$$X_O = R_C \sin\alpha \tag{52}$$
$$Z_O = R_C \cos\alpha. \tag{53}$$

The second constraint gives us

$$R_C = \sqrt{(G+Z_S)^2 + 2X_F^2} \quad \text{or} \quad G = \sqrt{R_C^2 - 2X_F^2} - Z_S. \tag{54}$$

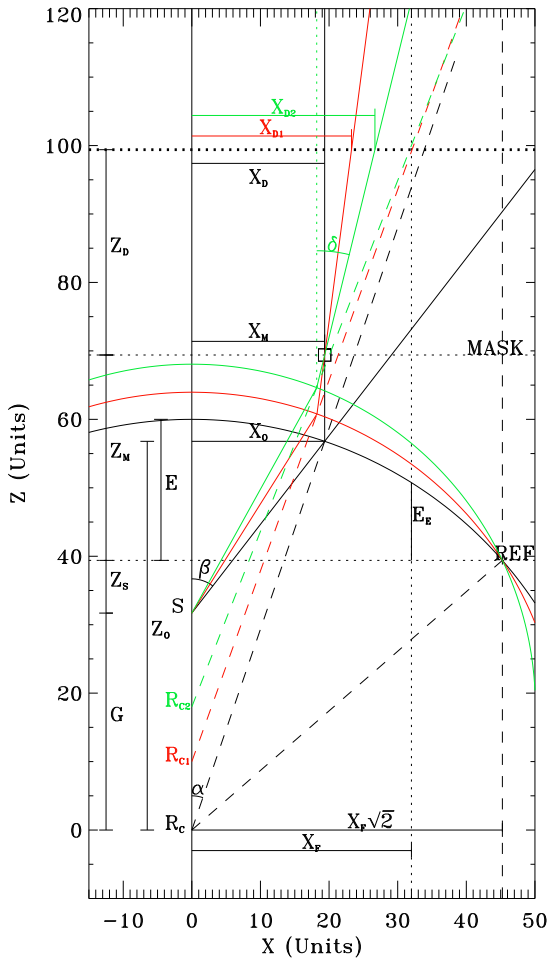

Figure 48. Reverse beamline configuration geometry with a post-reflection mask. The detector plane is shown by a heavy dotted line. The black curve is the location of the optic for a radius of curvature, R_C, centered at the origin. The source is at S, which is the focus for this optic. The mask is at the level of the *horizontal dotted line* marked "MASK"; the horizontal dotted line marked "REF" is the reference surface upon which rest the corners of the optic. A ray from the source strikes the optic a distance X_O from the optical axis, and is reflected through the pin-hole in the mask a distance X_M from the optical axis, and towards the detector. The *red* and *green* curves show two other possible optics for which S is not at the focus, and the resulting optical paths due to a ray through the pin-hole. The *dotted vertical black line* denotes the edge of the optic. In order to make a readable figure, these dimensions do not correspond to any real optics.

The third constraint provides

$$\frac{X_D - X_M}{Z_D} = \tan\delta \tag{55}$$
$$\frac{X_M - X_O}{Z_M + Z_S + G - Z_O} = \tan\delta \tag{56}$$

directly from the construction in Figure 48, with help from Figure 49. Note that the left-hand side of the first line is composed solely of measured quantities, meaning that $\tan\delta$ is known from measured quantities. We further know that

$$\delta = 2\alpha - \beta \tag{57}$$

from Equation 44. Finally, we also know, from the law

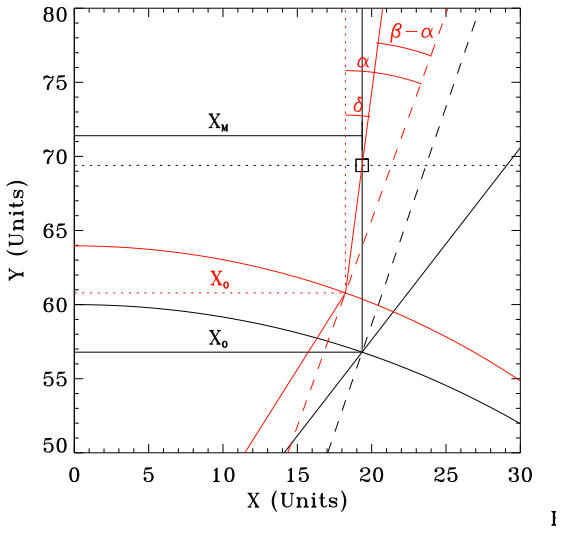

Figure 49. A detail from the previous figure from around the reflection point.

of sines that

$$\frac{\sin(\beta-\alpha)}{G} = \frac{\sin\beta}{R_C} \tag{58}$$

from which one can isolate β in the law of sines,

$$\tan\beta = \frac{\sin\alpha}{\cos\alpha - G/R_C}. \tag{59}$$

There is clearly a relation between α, β, and G/R_C . However, unlike the reverse beamline configuration with a premask, where β is fixed, here α, β, and δ all change as R_C changes. Keeping the source at the same location with respect to the reference plane, as R_C increases, α decreases by a small amount, and β increases (though, admittedly, by an almost imperceptible amount), all keeping the output ray in the pin-hole at X_M. This difference, it appears, means that there is no analytic solution, only a numerical one.

Thus, the algorithm for determining X_D from the measured values (X_M, X_F, Z_S, Z_M, Z_D), stands as follows.

1. Set a guess of R_C.
2. Calculate $G = \sqrt{R_C^2 - 2X_F^2} - Y_S$.
3. For a range of α' calculate $\beta(\alpha')$ using the law of sines. I have found it adequate for $\alpha' = \arctan(X_M/R_C) \pm 5°$, but the step size needs to be $\sim 10^{-5\circ}$.
4. Calculate $\delta(\alpha')$ from $2\alpha' - \beta(\alpha')$.
5. Calculate $X_O(\alpha') = \sin\alpha'$ and $Y_O(\alpha') = \cos\alpha'$.
6. Calculate $\tan\delta'(\alpha') = \frac{X_M - X_O(\alpha')}{Y_M + Y_S + G - Y_O(\alpha')}$.
7. Determine which $\delta'(\alpha')$ equals the $\delta(\alpha')$. This essentially is finding a δ with is consistent with both Equation 55 and Equation 56.

To elucidate, for a given value of R_C, we must find the α (and thus X_O) for which the angle δ of the ray coming off of the pore interior is the same as the δ require to get the ray from X_O through X_M. Once we determine that α we can calculate the X_D.

Table 6
Reverse Beamline Postmask Errors

Param	True Value[a] (mm)	Delta Value (mm)	Delta X_D
Z_S	330.0	+1.0	1.12%
Z_D	$Z_T - (Z_S + Z_M)$	+1.0	0.09%
Z_M	1.5	+1.0	0.03%
X_F	20.0	+1.0	0.06%
X_M	10.0	+0.1	1.00%

[a] Quantities in red are those that are either known or measured directly.

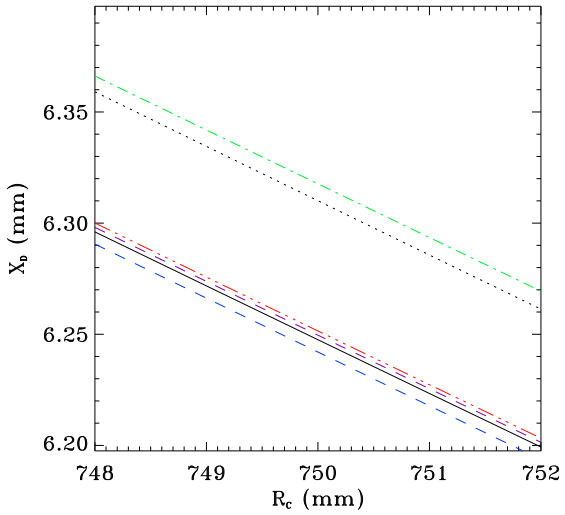

Figure 50. A plot of X_D as a function of R_C for a 750 mm radius of curvature optic. *Blue dashed line:* an error of 1 mm in Z_D (which is nearly indistinguishable from the true X_D-R_C function) *Green dot-dashed line:* an error of 1 mm in Z_S, *Purple dashed line:* an error of 1 mm in Z_M, *Red dot-dashed line:* an error of 1 mm in X_F, *Dotted line:* an error of 0.1 mm in X_M.

This method works quite well. There are, however, a number of issues that have been ignored: the source will have a finite extent (~200μm radius), and the optic has a finite thickness.

The Uncertainty in R_C: As in the previous section, we have calculated X_D from R_C under the assumption that: R_C=750.0 mm and Z_T=989.887 mm and the parameters given in Table 11. We then solved for X_D given an increment in each input parameter separately. The percentage change of X_D is given in the table, while the results can also be seen in Figure 50. Note that the errors are not significantly different than those found for the premask case.

Measuring Throughput: Measuring the throughput requires a simulation of the test rig.This can not be done with the current PBP, but a special implementation of PBP for this configuration is in the works.

Table 7
Reverse Beamline - Willingale Variables

Symbol[a]	Explanation
G	distance from source to center of curvature
L	length of an individual pore = thickness of the optic
R_c	Radius of curvature
W	width of an individual pore
X_D	off-axis beam spot on the detector
X_M	distance from the optical axis of pin-hole in mask
Z_D	distance from the mask to the detector
Z_S	distance from the mask to the source
α	angle from OA of reflecting pore wall
β	angle from OA of ray from source

[a] Quantities in red are those that are either known or measured directly.

8.4. *Reverse Beamline Configuration - Willingale Approximation*

Willingale has a very different solution to the problem of the reverse beamline that, once one has lovingly and carefully laid out the problem as exactingly as possible, seems too simple to work. His configuration is shown in Figure 51. The optic is approximated as flat and coincident with the mask. The inclination of the pores from the optical axis is still given by $\arctan(X/R_C)$.

Solving for R_C: From construction we find that

$$X_D = X_M + Z_D \tan\delta \tag{60}$$

where $\delta = 2\alpha - \beta$. We can then use a series of small angle approximations to solve for X_D given S and R_C:

$$\begin{aligned}\tan\delta &= \tan(2\alpha-\beta)\\ &\sim \tan 2\alpha - \tan\beta\\ &\sim 2\tan\alpha - \tan\beta.\end{aligned} \tag{61}$$

where

$$\begin{aligned}\tan\alpha &= \frac{X_M}{R_C}\\ \tan\beta &= \frac{X_M}{Z_S}\end{aligned} \tag{62}$$

From this we find that

$$X_D = X_M\left[1 + Z_D\frac{2Z_S - R_C}{R_C Z_S}\right]. \tag{63}$$

This can be further manipulated to yield

$$R_C = \frac{2Z_S}{1-\frac{Z_S}{Z_D}(1-\frac{X_D}{X_M})} \tag{64}$$

Setting X_M: Note that Equation 63 provides an easy way to determine where the peripheral hole should be, given R_C, Y_S, and desired X_D.

Uncertainty: How good is this approximation? One would expect that, for long focal length optics, such an approximation might be adequate. For a typical 4 cm by 4 cm facet with R_C=75 cm, the center of the optic is a whole 0.02667 cm above the reference plane, which is small compared to the other relevant quantities. Thus the assumption of a *flat* optic is not unreasonable. For the premask configuration, the co-extant of the mask and the optic is also reasonable. It may be less reasonable for the postmask configuration given that, for that configuration, the mask may be placed some distance away from the optic.

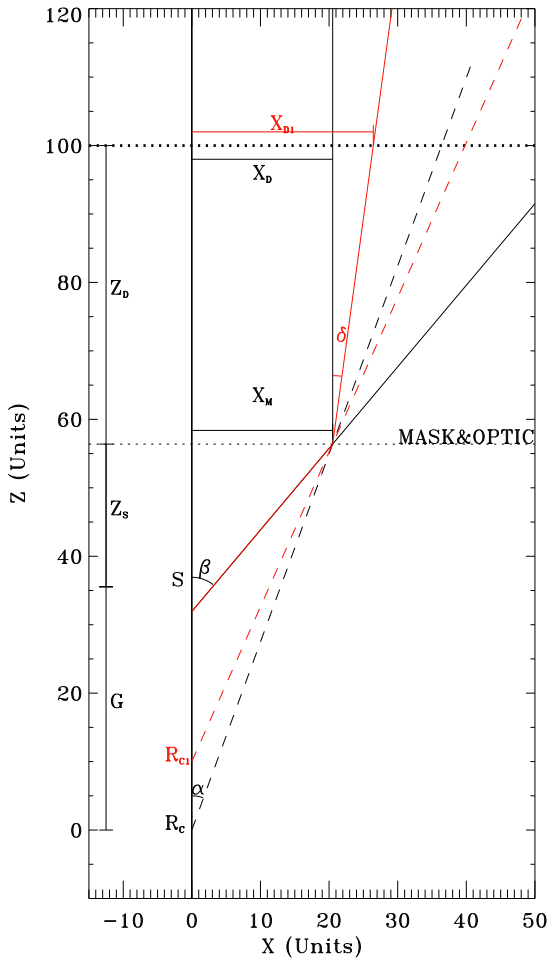

Figure 51. Reverse beamline configuration geometry with a mask as formulated by Willingale. The detector plane is shown by a heavy dotted line. The dotted line is the optic and the mask, both of which are assumed to be flat. Thus, there is no difference between a premask and a postmask configuration. The inclination of pores to the optical axis is given by α. The source is at S, which is the focus for this optic. When in focus, a ray from the source strikes the optic a distance X_O from the optical axis, and is reflected through the pin-hole in the mask a distance X_M=X_O from the optical axis, and towards the detector. The *red* is the construction for another possible optic for which S is not at the focus.

Nick Thomas points out that a pore, 20μm across, as seen from the source, 37.5 cm away, subtends 5.3×10^{-5} radian. For typical values of alpha ($\sim 1\overset{\circ}{.}5$), the approximation $\tan(\beta-\alpha) \sim \tan\beta - \tan\alpha$ introduces an error of 3.6×10^{-5}, which is smaller than the extent of a pore. He also points out that the source size is $\sim$400μm, with will subtend an angle of 1.06×10^{-3} radian, which is far bigger than the error introduced by the small angle approximation.

Comparison to Complex Calculations: I ran the complex method (Kuntz) and the simple method (Willingale) for the same pre-mask and post-mask configurations. In all cases I calculated X_D for a $\pm$10 mm range around the true R_C=750 mm. For both configurations, X_D was calculated from R_C in the manners described in the previous two sections.

For the premask configuration, the Z_S for the Will-

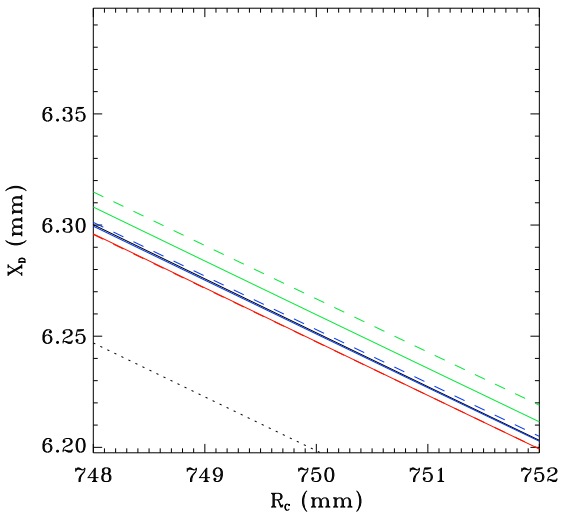

Figure 52. A plot of X_D as a function of R_C for a 750 mm radius of curvature optic. *Black solid line:* The relation derived from the complex premask calculation. *Black dotted line:* The relation derived from the Willingale calculation. *Red solid line:* The relation derived from the complex postmask calculation for Z_M=1.5 mm. *Red dashed line:* The relation derived from the Willingale calculation for Z_M=1.5 mm. *Blue solid line:* The relation derived from the complex postmask calculation for Z_M=2.5 mm. *Blue dashed line:* The relation derived from the Willingale calculation for Z_M=2.5 mm *Green solid line:* The relation derived from the complex postmask calculation for Z_M=5.0 mm *Green dashed line:* The relation derived from the Willingale calculation for Z_M=5.0 mm.

Table 8
Reverse Beamline Willingale Errors

Test	K-W[a] (mm)	(K-W)/K[a] (%)
Premask	0.053	0.8
Postmask Z_M=1.5 mm	0.00012	0.002
Postmask Z_M=2.5 mm	-0.0020	0.03
Postmask Z_M=5.0 mm	-0.0071	0.11

[a] K-W is the X_D calculated by the complex methods above minus the X_D calculated by the Willingale method.

ingale calculation was taken to be the same Z_S used in the more complex calculation of §8.2. However, for the postmask configuration, one must be more careful about the Z_S used in the Willingale calculation, the $Z_S + E$ used in the more complex calculation should be used. (We did try using $Z_S + Z_M$, but it produced a much larger descrepency between the complex and Willingale calculations.) The results are shown in Figure 8.4 and in Table 8.

The difference between the premask calculation and the Willingale calculation is significant, on the order of 4 13.5 μm pixels (for the current detector) which, in principle, should be noticeable. The difference between the postmask calculation and the Willingale calculation is quite small for small Z_M, and increases as X_M increases. For all of the postmask cases, the differences are fractions of a pixel.

We should also note that there is a difference in X_D depending upon whether the mask is behind or in front of the optic. That difference is unlikely to pose design restrictions.

8.4.1. *Setting Up X_M*

In the two previous sections, it has been noted that, ideally, one would want to set X_M so that it samples the part of the facet having a high fraction of singly reflected rays. (Since it is on a diagonal, that criterion is sufficient for both dimensions.) As usual

$$\frac{W}{L} = \tan(\beta - \alpha) \tag{65}$$

Assuming a radius of curvature R_C, and a source a distance Z_S from the optic, then, using the small angle approximation that $\tan(\beta - \alpha) \sim \tan\beta - \tan\alpha$ we find

$$\frac{W}{L} = \tan(\beta - \alpha) \sim \left[\frac{X_M}{Z_S} - \frac{X_M}{R_C}\right]. \tag{66}$$

From this we find that

$$X_M \sim \left[\frac{W}{L}\right] \frac{R_C Z_S}{R_C - Z_S} \tag{67}$$

However, as a practical matter, those reflected rays may not fall onto the detector that is being used. Further, note that one can change either X_M or Z_S in order to get the peripheral spots to land on the detector. This means that there is a certain amount of freedom of choice here. However, it is best to consider the throughput of each combination of X_M and Z_S that puts the peripheral spots onto the detector, and chose the best combination in order to produce the brightest possible peripheral spots.

Since $Z_D + Z_S$ is usually fixed to some constant Z_{tot}, we can, from Equation 63 find that

$$X_M = \frac{X_D}{\left[1 + (Z_{tot} - Z_S)\frac{2Z_S - R_C}{R_C Z_S}\right]}. \tag{68}$$

One can combine the previous two equations and rearrange terms to find that Z_S can be found by the quadratic equation where

$$a = -2W/L \tag{69}$$
$$b = 2W/L(R_c + Z_{tot}) - X_D \tag{70}$$
$$c = -R_C(Z_{tot}W/L + X_D) \tag{71}$$

which is rather an ungainly equation. Figure 8.4.1 shows the functional forms of our equations for X_M for the LEXI test stand operations in 2021. Note that by setting $\tan(\beta - \alpha)$ to the W/L for the particular device, we effectively remove any consideration of the change in reflectivity with angle. However, there is a trade-off between the efficiency of reflectivity at $\beta - \alpha$ with the reflected fraction.

8.4.2. *The Trade-Off*

This section was lifted from the LEXI test stand report. It needs to be re-done in order to ensure that the results are correct, and to put the results into a more useful form.

As described above, the distance from the source to the optic/mask assembly is set by the distance between the peripheral holes in the mask, and is set to maximize

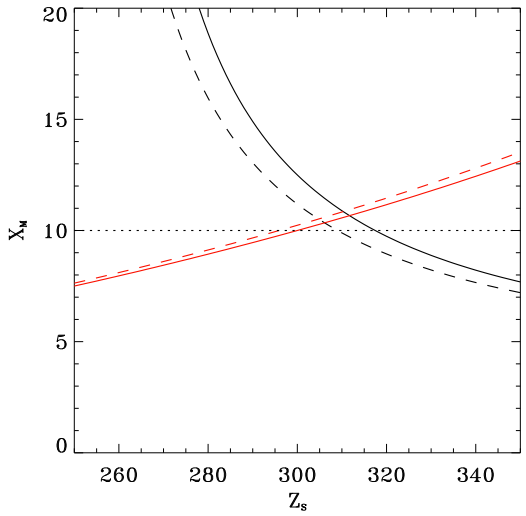

Figure 53. The relation between X_M and X_S given a fixed X_D, from Equation 68, (black) and from Equation 67 (red), which optimizes the focused fraction in the peripheral holes. The solid lines are for $R_C = 750$ mm while the dashed lines are for $R_C = 725$ mm. The dotted line shows the X_M that was actually used. The value of Z_{tot}=989.9 mm and the experimental $X_D \sim 6.75$ mm. For $R_C = 750$ mm we get the best X_M, Z_S at 10.7 mm, 311.7 mm while for $R_C = 725$ mm we get 10.5 mm, 304.7 mm.

the fraction of focused rays passing through the peripheral holes. However, it should be noted that the this maximization is based on geometric criteria only. We now consider how the brightness of the peripheral spots change with a change in the source-to-optic distance.

By construction, we set the distance from the optical axis to the peripheral hole so that the angle of incidence of a ray with the pore wall, Γ, at the center of the peripheral hole is given by $\Gamma = \arctan(W/L)$ which maximizes the number of rays with a single reflection in each dimension. Thus, for a peripheral hole, the side closest to the axis will have $n_{min} = 0$ and f_{min} small and declining towards the center, at the center n_{min} changes from 0 to 1 and f_{min} changes from 0 to 1, and f_{min} declines towards the opposite side.

To understand the effect of changing the source distance, Z_S on the output peripheral spot, I created a square grid of pores. For each pore I calculated angle from the optical axis in the x dimension, α_x and in the y dimension, α_y using the Willingale small angle approximation: $\alpha \sim \tan\alpha = X_M/R_c$. Similarly, I calculated the angles β_x and β_y for the source, and from them the angle of incidence in both dimensions: Γ_x and Γ_y. From the above formulae I calculated fraction of rays entering a pore that are reflected a single time in each dimension. Figure 54 shows the focussed fraction as a function of the source distance. (Note that this plot does not include the reduction by the open fraction which is ~ 0.6.) Note that the focussed fraction is a slightly assymmetric function with the focussed fraction being slightly higher at $Z_S + \Delta$ than it is at $Z_S - \Delta$. Moving the source by 10 mm from Z_S reduces the focused fraction by $\sim 7.5\%$.

However, this is not the primary effect. The *reflectivity* is a strong function of the incidence angle Γ. To determine the throughput, one must multiply by the reflectivity for the reflection in x and by the reflectivity for the reflection in y. Since the reflectivity decreases as the incidence angle increases, as Z_S decreases, Γ increases, the reflectivity falls, as does the throughput. Thus the peak of the throughput function is at greater Z_S than the peak of the focused fraction function, and the throughput function is far more asymmetric than the focused fraction function.

We should also note that the peak of the peripheral spot need not represent the output angle at the center of the hole, as it is the throughput weighted average of the output angle over the entire hole.

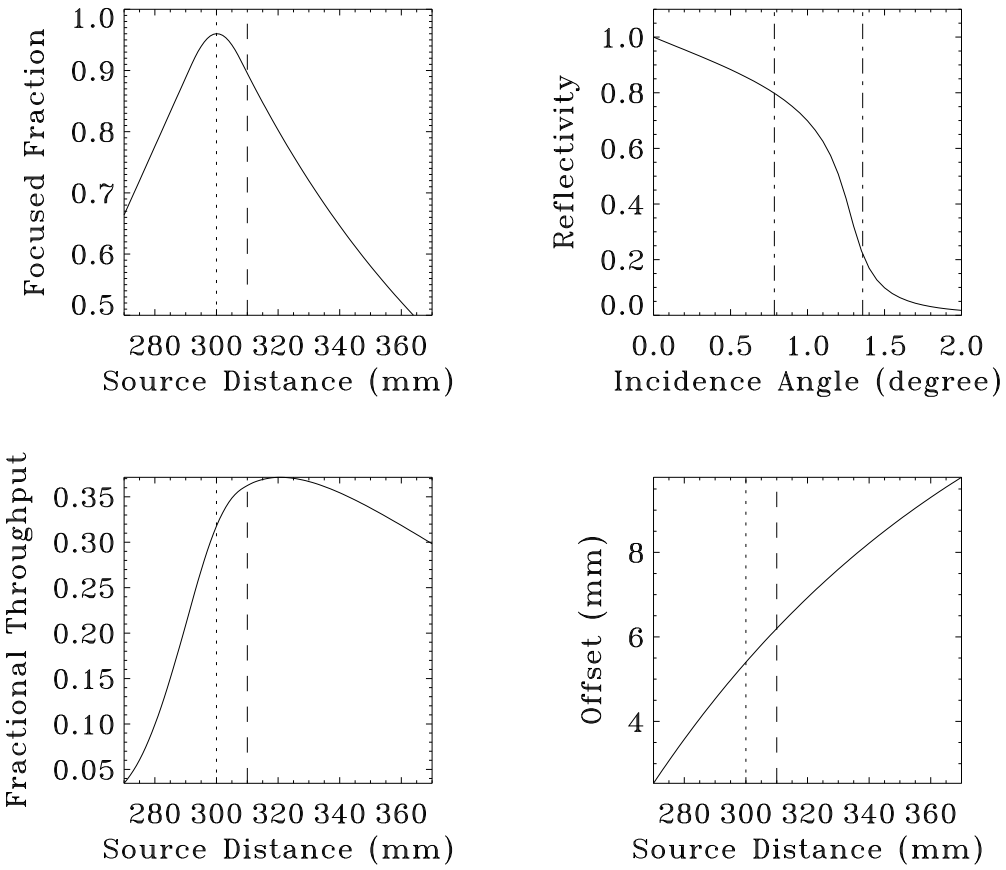

Figure 54. *Top Left:* The focused fraction for a peripheral hole as a function of the distance from the source to the optic. The dotted vertical line is the value of $\mathcal{Z}_S$ while the dashed vertical line is the value of Z_S used for the later facets. *Top Right:* The reflectivity as a function of the angle of incidence. The vertical lines mark the angles of incidence at the center of the peripheral hole for the extreme values of Z_S shown in the other panels. *Bottom Left:* The fractional throughput *not included the effect of the open area fraction* as a function of distance of the source from the optic. The open area fraction is 0.6. *Bottom Right:* The expected distance of the peripheral spot from the centerline on the detector for a R_c=750 mm optic.

Table 9
Double Reverse Beamline - Willingale Variables

Symbol[a]	Explanation
L	length of an individual pore = thickness of the optic
R_c	Radius of curvature
W	width of an individual pore
X_D	off-axis beam spot on the detector
X_M	distance from the optical axis of pin-hole in mask
Z_D	distance from the mask to the detector
Z_S	distance from the mask to the source
α	angle from OA of reflecting pore wall
γ	angle from OA of ray from source

[a] Quantities in red are those that are either known or measured directly.

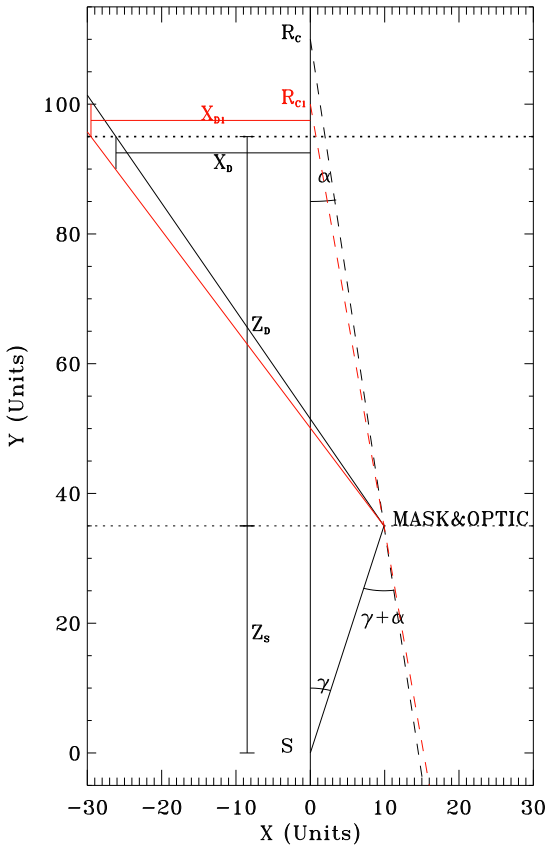

Figure 55. Double reverse beamline configuration geometry with a mask using Willingale's approximations. The detector plane is shown by a heavy dotted line. The dotted line is the optic and the mask, both of which are assumed to be flat. Thus, there is no difference between a premask and a postmask configuration. The inclination of pores to the optical axis is given by α. The source is at S. A ray from the source strikes the optic a distance X_M from the optical axis, and is reflected through the pin-hole in the mask, and towards the detector. The *red* is the construction for another possible optic with a shorter R_C placed in the same configuration.

8.5. *Double-Reverse Beamline Configuration - Willingale Approximation*

Given that Willingale's method is so effective for the reverse beamline configuration, it is useful to try the same technique for the double reverse beamline configuration. (I'm unaware of any previous attempt to do, and there may be a reason for that.) Figure 55 shows this configuration. As with the reverse beamline configuration, there is no distinction between a premask and a postmask configuration.

From Figure 55 we see that

$$X_D + X_M = Z_D \tan(2\alpha + \gamma) \tag{72}$$

Using the small angle approximation that $\tan(2\alpha+\gamma) \sim 2\tan\alpha + \tan\gamma$, we find that

$$X_D = X_M \left[Z_D \frac{2Z_S + R_C}{R_C Z_S} - 1 \right]. \tag{73}$$

As usual, the peripheral pin-hole in the mask is ideally placed to isolate the rays that have only a single reflection in each dimension. For this configuration this means that

$$\frac{W}{L} = \tan(\alpha + \gamma). \tag{74}$$

Using $\tan\alpha = X_M/R_C$, $\tan\gamma = X_M/Z_S$, and the small angle approximation we find that

$$X_M \sim \left[\frac{W}{L}\right] \frac{R_C Z_S}{R_C + Z_S}. \tag{75}$$

These equations have a pleasing symmetry with those for the reverse beamline configuration.

Comentariolus: For the current test stand, the distance from the source to the detector is 989.887 mm. The distance from the source to the optic $Y_S = 389^{+55}_{-95}$ mm, where the range is the travel of the platform. Using these numbers we can calculate that, for a R_C=750 mm, W/L=0.02 facet, the ideal X_M ranges from 4.2 mm to 5.6 mm (for Z_S ranging from 294 mm to 444mm). These are rather close to the central hole, and might require careful sizing of the central hole. The resulting X_D ranges from 13.6 mm to 9.4 mm; the half-width of the CCD is 13.8 cm. Thus, this configuration is possible; the output beam does fall onto the CCD, though for one extreme it falls close to the edge. Alignment issues may be important.

The reflection angle, $\gamma + \alpha$ for both extremes is 1.14° which is still reasonable for good throughput, but may not be ideal. Depending upon the reflectivity curve of the surface of the optic, a smaller X_M may be better for both throughput and for placing the spot closer to the center of the detector.

8.6. *Willingale vs. Willingale: Reverse Beamline vs. Double Reverse Beamline*

Using Willingale approximations for both the reverse beamline configuration and the double reverse beamline configuration allows one to make a simple direct comparison of the two configurations. We see from the above formulae that

$$X_M = \left[\frac{W}{L}\right] \left(\frac{R_C Y_S}{R_C \mp Y_S}\right) \text{ and}$$
$$X_D = X_M \left[\mp Y_D \frac{2Y_S \mp R_C}{R_C Y_S} \pm 1 \right] \tag{76}$$

Lever Arm: Given an expected R_C, how much change in X_D is there per change in R_C? For the LEXI optic with R_C=750 mm, Z_S=375 mm, and D_D=988.9 mm-Z_S, we can compare the quantity $X_D(R_C) - X_D(750)$

for the two difference configurations. This comparison, requires the optimization of X_M for both configurations.

Table 10
Double Reverse Beamline - Postmask Variables

Symbol[a]	Explanation
E	distance from the mask to optic on the OA
L	length of an individual pore = thickness of the optic
R_c	Radius of curvature
W	width of an individual pore
X_D	off-axis beam spot on the detector
X_F	radius of the facet
X_M	distance from the OA of pin-hole in mask
X_0	distance from OA of reflection point
Z_D	distance from the mask to the detector
Z_S	distance from the mask to the source
Z_0	distance above mask of reflection point
α	angle from the OA of reflecting pore wall
γ	angle from the OA of ray from source

[a] Quantities in red are those that are either known or measured directly.

8.7. *Double-Reverse Beamline Configuration Testing with Postmask*

In this configuration the source is placed on the convex side of the optic, while the detector is placed on the opposite side of the optic. Since the source rays strike the optic rather more obliquely than for the other configurations, the setup is rather more complex. It is assumed that the concave side of the optic rests upon a mask, and that the distance between the mask and the source, Z_S is known, as is the distance between the mask and the detector Z_D. Both of these quantities will be assumed to be to the top of the mask. Given X_F, the distance between the mask and the center of the optic is E as given in §8.2. It is assumed that X_M has been set.

I suspect that there may be an error in the following derivation.

Solving for R_C: From the animadversions of the previous sections, it should be no surprise that one can't simply measure X_D and calculate R_C. Indeed, one must assume an R_C (which provides E), and then use a root finder (or the equivalent) to determine the value of X_0 for which the reflected beam passes through the mask at X_M. Once that X_0 has been found, X_D follows simply.

For a given X_0':

$$\begin{aligned} Z_0' &= E - \left[R_C - \sqrt{R_C^2 - X_0'^2}\right] \\ \gamma' &= \arctan\left(\frac{X_0'}{Z_S - Z_0'}\right) \\ \alpha' &= \arcsin\left(\frac{X_0'}{R_C}\right) \\ \delta' &= \gamma' + 2\alpha' \\ X_M' &= X_0' - Z_0' \tan\delta \end{aligned} \tag{77}$$

where we have used primes to indicate test values. We must, somehow, iteratively find the X_0' for which X_M'=X_M.

Then,

$$X_D = (Z_0 + Z_D)\tan\delta - X_0. \tag{78}$$

The Uncertainty in R_C: As in previous sections, we have calculated X_D from R_C under the assumption that: R_C=750.0 mm and Z_T=989.887 mm and the parameters given in Table 11. We then solved for X_D given an increment in each input parameter separately. The percentage change of X_D is given in the table, while the results can also be seen in Figure 57.

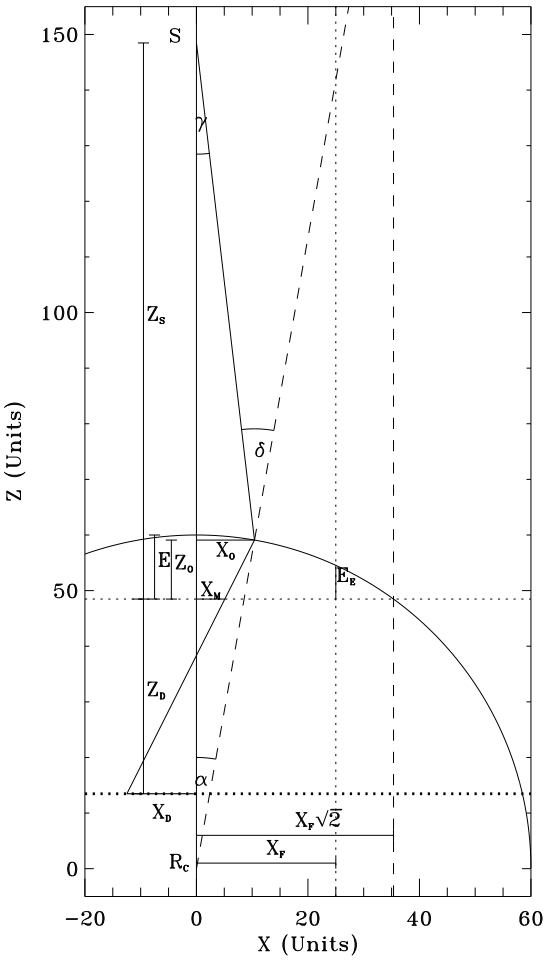

Figure 56. Double reverse beamline configuration geometry. The black curve is the location of the optic for a radius of curvature, R_C, centered at the origin. The source is at S. The mask is at the level of the *horizontal dotted line*. A ray from the source strikes the optic a distance X_O from the optical axis, and is reflected towards the detector. The *red* and *green* lines show two other possible rays from the source. The *dotted vertical black line* denotes the edge of the optic. In order to make a readable figure, these dimensions do not correspond to any real optics. In particular, the detector is likely to be placed below the point of curvature.

Table 11
Reverse Beamline Postmask Errors

Param	True Value[a] (mm)	Delta Value (mm)	Delta X_D
Z_S	330.0	+1.0	0.12%
Z_D	$Z_T - (Z_S + Z_M)$	+1.0	0.16%
X_F	20.0	+1.0	0.04%
X_M	10.0	+0.1	2.35%
Willingale		0.0	32.1%

Figure 57 has a rather odd size to put it on the same scale as the other error figures in the previous sections. While the errors due to Z_S, Z_D, and X_F are not unusual, compared to the reverse beamline configurations, the error introduced by X_M is far larger. This large offset is

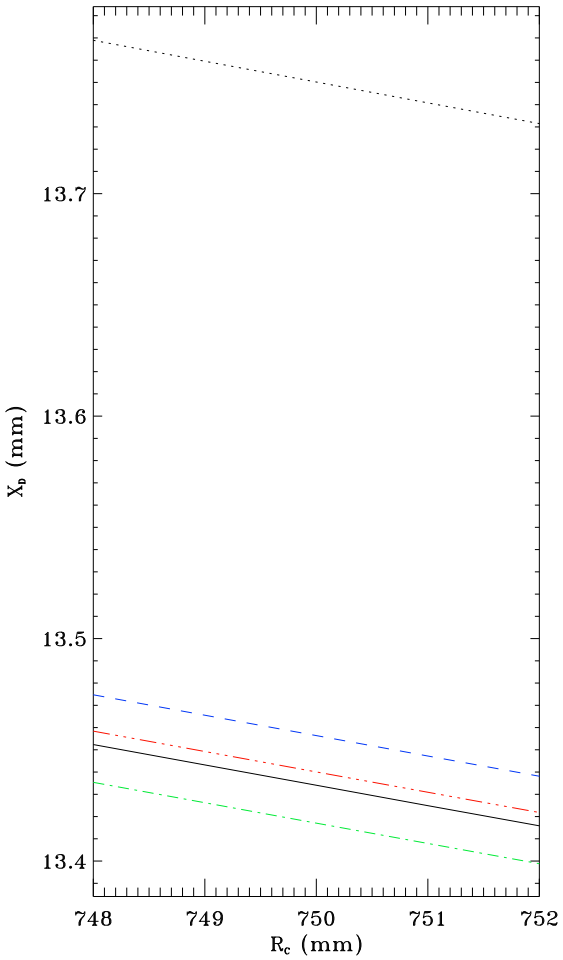

Figure 57. A plot of X_D as a function of R_C for a 750 mm radius of curvature optic. *Blue dashed line:* an error of 1 mm in Z_D, *Green dot-dashed line:* an error of 1 mm in Z_S, *Red dot-dashed line:* an error of 1 mm in X_F, *Dotted line:* an error of 0.1 mm in X_M.

likely due to the larger δ for the double-reverse beamline than found in the reverse beamline. We also note that the dX_D/dR_C is smaller for the double-reverse beamline than it is for the reverse beamline, suggesting that it's not as sensitive for measuring the R_C.

We will also note that the "Willingale approximation" (not that he's ever used this approximation for a double-reverse beamline) is not on this plot; the approximation prediction for X_D is 9.12 mm, a 32.1% error. Thus, the Willingale-style approximation should not be used for the double-reverse beamline with a postmask. As we will see in the next section, the Willingale-style approximation is fine for a double-reverse beamline with a premask. The difference is presumably due to the much larger angle between the ray and the optical axis after reflection compare to before reflection.

Summary: We conclude that the double-reverse beamline with a postmask is not a good configuration for measuring R_C due to the need for a small X_M (to get the spot on the detector), the sensitivity of the X_D to errors in X_M, and a smaller dX_D/dR_C.

Table 12
Double Reverse Beamline - Premask Variables

Symbol[a]	Explanation
E	distance from the mask to optic on the OA
L	length of an individual pore = thickness of the optic
R_c	Radius of curvature
W	width of an individual pore
X_D	off-axis beam spot on the detector
X_F	radius of the facet
X_M	distance from the OA of pin-hole in mask
X_0	distance from OA of reflection point
Z_D	distance from the reference plane to the detector
Z_S	distance from the reference plane to the source
Z_M	distance from the reference plane to the mask
Z_0	distance above mask of reflection point
α	angle from the OA of reflecting pore wall
γ	angle from the OA of ray from source

[a] Quantities in red are those that are either known or measured directly.

8.8. *Double-Reverse Beamline Configuration Testing with Premask*

In this configuration the source is placed on the convex side of the optic, while the detector is placed on the opposite side of the optic. Since the source rays strike the optic rather more obliquely than for the other configurations, the setup is rather more complex. It is assumed that the concave side of the optic rests upon a reference plane, and that the distance between the reference plane and the source, Z_S is known, as is the distance between the reference plane and the detector Z_D. The mask is placed on the source side of the optic a distance Z_M from the reference plane. Given X_F, the distance between the mask and the center of the optic is E as given in §8.2. It is assumed that X_M has been set.

Solving for R_C: As we saw with the double-reverse beamline with a postmask, one can't simply measure X_D and calculate R_C. Indeed, one must assume an R_C (which provides E), and then use a root finder (or the equivalent) to determine the value of X_0 for which the reflected beam passes through the mask at X_M. Once that X_0 has been found, X_D follows simply.

For a given R_C:

$$\tan\gamma = \left(\frac{X_M}{Z_S - Z_M}\right)$$

$$X_0 = \left(\frac{X_M(Z_S - E)}{Z_S - Z_M}\right) = (Z_S - E)\tan\gamma$$

$$Z_0 = E - \left[R_C - \sqrt{R_C^2 - X_0^2}\right]$$

$$\alpha = \arcsin\left(\frac{X_0}{R_C}\right)$$

$$\delta = \gamma + 2\alpha \tag{79}$$

$$\tag{80}$$

Then,

$$X_D = (Z_0 + Z_D)\tan\delta - X_0. \tag{81}$$

Thus, we need to use the equivalent of a root finder to determine R_C from X_D.

The Uncertainty in R_C: As in previous sections, we have calculated X_D from R_C under the assumption that: R_C=750.0 mm and Z_T=989.887 mm and the parameters given in Table 4. We then solved for X_D given an increment in each input parameter separately. The percentage change of X_D is given in the table, while the results can also be seen in Figure 59.

We note that the Willingale-style approximation is good for this configuration so long as one uses the mask

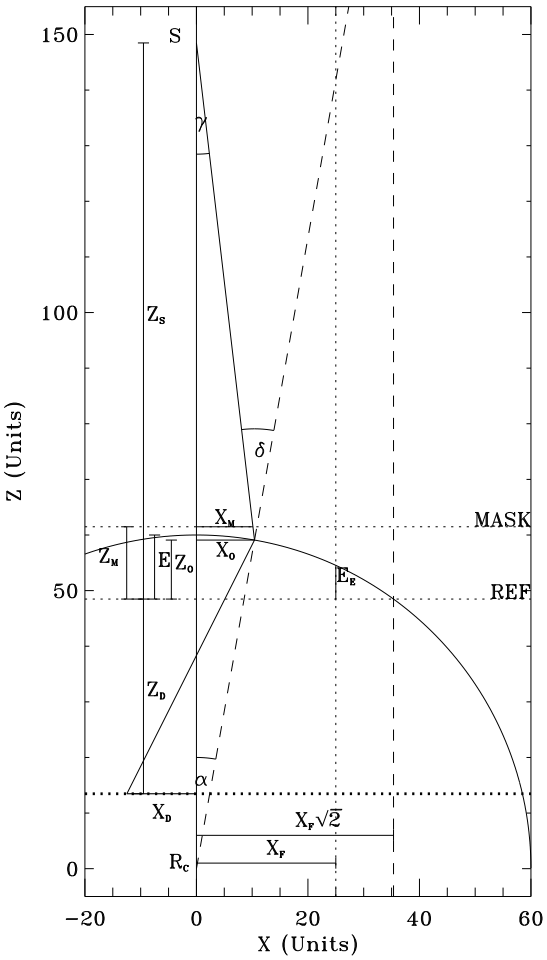

Figure 58. Double reverse beamline configuration geometry. The black curve is the location of the optic for a radius of curvature, R_C, centered at the origin. The source is at S. The mask is at the level of the *horizontal dotted line* marked "MASK" while the reference plane upon with the optic sits is the *horizontal dotted line* marked "REF". A ray from the source strikes the optic a distance X_O from the optical axis, and is reflected towards the detector. The *dotted vertical black line* denotes the edge of the optic. In order to make a readable figure, these dimensions do not correspond to any real optics. In particular, the detector is likely to be placed below the point of curvature.

Table 13
Double Reverse Beamline Premask Errors

Param	True Value[a] (mm)	Delta Value (mm)	Delta X_D
Z_S	330.0	+1.0	0.18%
Z_D	$Z_T - (Z_S + Z_M)$	+1.0	0.20%
Z_M	2.0	+1.0	0.26%
X_F	20.0	+1.0	0.009%
X_M	10.0	+0.1	2.35%
Willingale		0.0	0.2%

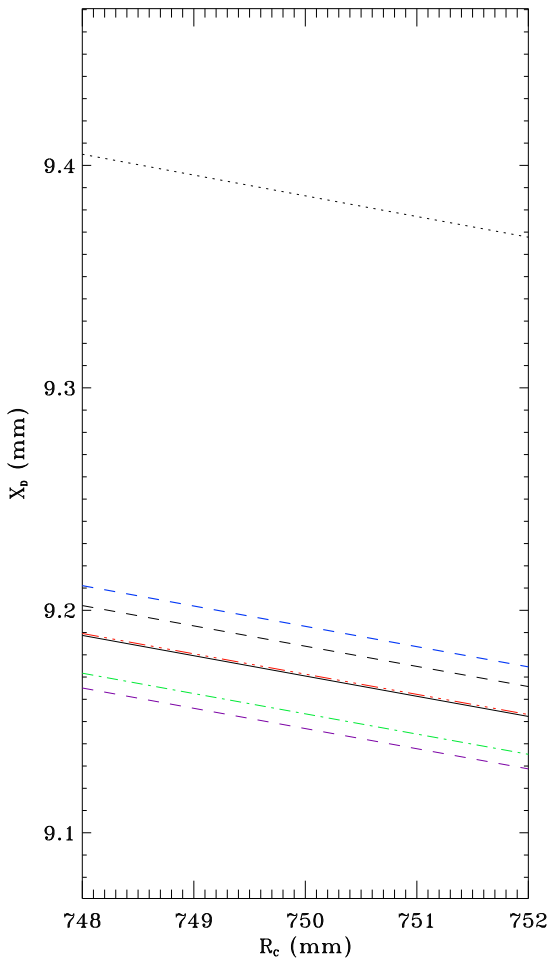

Figure 59. A plot of X_D as a function of R_C for a 750 mm radius of curvature optic. *Blue dashed line:* an error of 1 mm in Z_D, *Green dot-dashed line:* an error of 1 mm in Z_S, *Purple dashed line:* an error of 1 mm in Z_M, *Red dot-dashed line:* an error of 1 mm in X_F, *Dotted line:* an error of 0.1 mm in X_M.

plane for the calculations of Z_S and Z_D rather than the reference plane.

8.9. *Summary*

9. TEST STAND TESTING

9.1. *Current Test Stand*

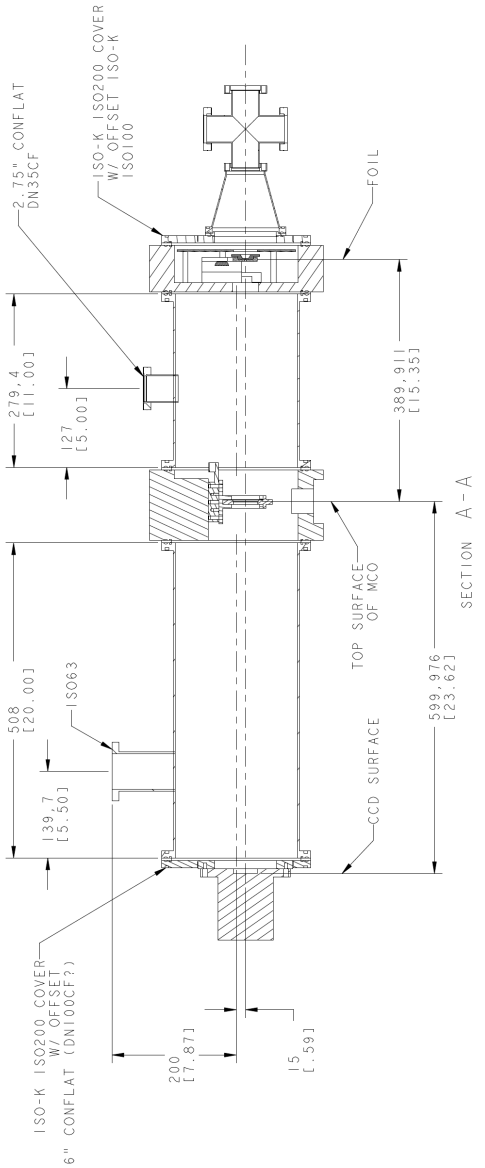

Figure 60. The drawing of the current test stand as designed by Nick Thomas in the orientation that is currently used. The source is at the top and the CCD is at the bottom. (Yes, we all think the same thing about that. Nick had his constraints and he would have done it differently if he could have.)

The current GSFC test stand is a reverse beam line configuration with a post-mask, as described in §§8.3 and 8.4 and shown in Figure 51. The physical structure of the current GSFC test stand is shown in Figure 9.1, which has the source at the top, and the detector at the bottom.

One important consideration is the size of the detector. Typical CCDs do not have formats of 4 cm by 4 cm, so we will need to set the X_M to explore the part of the detector which will be doing the bulk of the focussing, while setting the Z_S to ensure that the beams from the peripheral holes fall on the detector. Moving the source closer to the optic, moves the part of the optic that is reflecting X-rays closer to the center and makes the output beams more converging.

Table 14
LEXI Test Stand Parameters

Parameter	Symbol	Value
Optic		
Nominal radius of curvature	R_c	750 mm
Nominal pore width	W	20e-3 mm
Nominal pore length	L	1.0 mm
Mask		
Center hole radius	r_c	1.0 mm
Peripheral hole radius	r_p	0.5 mm
Peripheral hole distance from axis	X_M	10 mm
Stand		
Distance from source to detector	Z_{tot}	989.887 mm
Distance from optic to source	Z_S	310 mm
Distance from optic to detector	Z_D	$Z_{tot} - Z_S$
Detector		
CCD size		∼2100 pixels
Pixel size		13.5 μm

As noted in the introduction to §8, we want to determine the true radius of curvature R_C, the throughput of fully focused rays for some "representative" portions of the SMO, and we would like some measure of the expected PSF. We can determine the R_C using the distance between the spots produced by the peripheral holes. We should be able to determine the throughput of the fully focused rays by comparing the number of counts we get in the peripheral spots to the number of counts we get in the center spot. However, we have a fundamental uncertainty here that has not yet been resolved. We do not know the illumination pattern of the source. Thus, we do not know with great certainty what ratio we would expect between the illumination of the central hole and that of the peripheral holes. Finally, we might expect to say something about the size of the PSF from the size of the peripheral spots.

In the following section we will explore a number of complications in the use of the test stand, as well as quantify a number of possible sources of error.

9.2. *The Standard Method*

The standard mask has a circular hole at the optical axis of the MPO, of radius r_c, and four peripheral holes or radius r_p, arranged in a square, that are each $X_M\sqrt{2}$ from the optical axis. The pore walls set the x and y axes, and the peripheral holes have the same distances from the x axis as they do from the y axis. The mask parameters for the LEXI campaign, as shown in Table 14, had been set in the past for other optics but, as can be seen in §8.4, were reasonably well optimized for LEXI. Figure 9.2 shows a typical image from the LEXI campaign. We should note a number of details.

First, the light in the central spot is not uniform. For comparison, Figure 62 shows a simulated image of what we expect from a perfect optic in a perfect test stand, while Figure 63 shows the distribution of the non-, partially-, and fully-focused photons for the central spot,

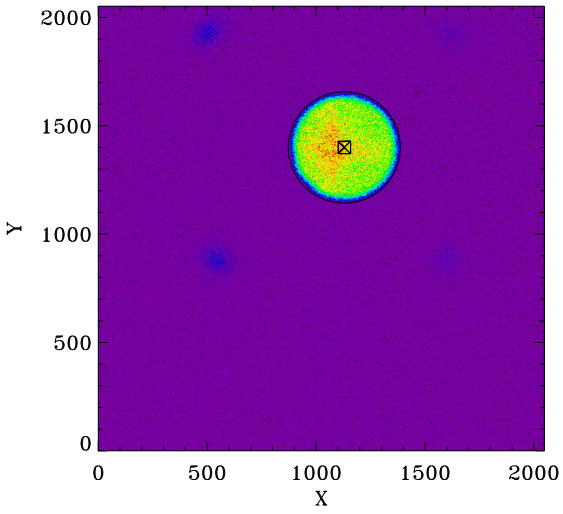

Figure 61. A typical image produced by the current test stand for one of the LEXI optics. Note the *offset* cruciform pattern with the central spot, and the faintness/difference in intensity of the spots produced by the peripheral holes.

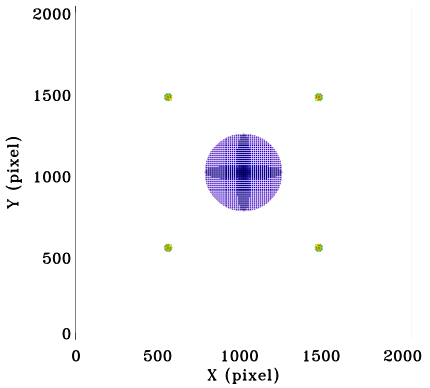

Figure 62. *Top:* Simulation of the image produced by a perfect optic in the test stand. There are a number of issues with this figure caused, in part by the "beating" between pores, and image pixels.

as well as the fully-focused photons from a peripheral spot. (Note that the non- and partially-focused photons from the peripheral spot will not land on the detector.) The central hole is sufficiently large that rays passing through the outer part of it have a reasonable probability of being partially or fully focused, while those at the center are most likely to pass through without reflection. This means that determining the true number of completely non-focused photons is not trivial.

Second, we note that the cruciform pattern from the partially and fully focused photons is not centered on the spot. This suggests a misalignment of the optic (tilt? off center?) or mask (off-center?) with the optical axis of the test stand.

Third, we note that there is a lower-brightness "rim" to the central spot, which can be seen in Figure 64. Since the rays that form the outer regions of the central spot are non-focused, we need not worry about the scattering of rays due to the misalignment of pores, which Willingale has found to produce a Lorentzian distribution

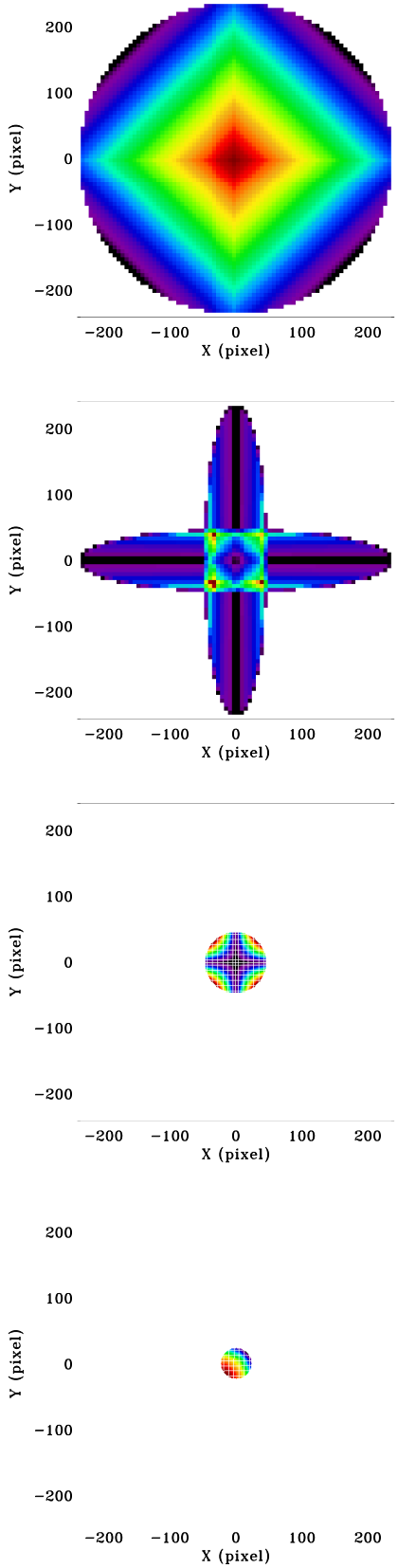

Figure 63. Simulation of the image produced by a perfect in the test stand, separated by focus type. The scalings are arbitrary and the first two images have been cleverly crafted to avoid the pixelization issues. All images have the same pixel scale. *From top to bottom:* Center unfocussed, center partially focussed, center fully focussed, and the upper right peripheral focussed.

rather than Gaussian one. (This distribution should be applicable to the partially and fully focused rays.) What is the effect of the misalignment of pores on the unreflected rays? A tilt of a pore away from the ideal will decrease (or increase) the open area for a given pore, and can change the location of the unreflected rays by only a very small amount. If we look at the measured radial profile of the central spot, we see that there is a *linear* decline between the inner and outer break points. A linear decline is symptomatic of a convolution with a tophat function, and can't be duplicated with a Gaussian or a Lorentzian. Note that if the broadening of the of the image is due to convolution with a tophat, the radius of the true edge of the spot will be the mean of the inner and outer break points.

One possible source for the tophat broadening might be the width of the pores, which was not taken into account in the model. The angular extent of a pore, as seen from the source is $\sim 13.3''$. What is the angular size of the linear decline? In the LEXI campaign we determined the linear distance on the detector over which the linear decline occurred, ΔX_D was 44.7 pixels for Z_S=310 mm.. There was quite a spread of values at each value of Z_S, and there was clear evidence that ΔX_D decreased as Z_S increased. We use the total distance from the source to the detector to determine the angular size of the linear decline: $125.7''$. This is a factor of 9.45 larger than the angle subtended by a pore. Thus while the angular extent of the pores could contribute to the "broadening" of the central spot, it could not explain the broadening seen.

The linear distance between the inner and outer break points, and that that distance decreases as Z_S increases argues that the source, as seen by the optic has a finite and non-negligible extent. Indeed, the emitting spot size on the foil is thought to have a diameter of 400 μm. If the linear extent of the source is

$$X_S = \frac{Z_S}{Z_D}\Delta X_D. \tag{82}$$

For the above data we find that X_S=275 μm, which is reasonably close to the assumed spot size. A spot size of 400 μm should produce a ΔX_D of 65 pixels at the detector. If we assume that the diameter of the central hole, X_M, is correct, the difference between expected and measured would require unreasonably large errors in Z_S (28%) and/or Z_D (21%). We note that the near linear decline from the inner break point to the outer break point implies that the source intensity is relatively uniform within the source radius.

Fourth, we note that the strength of the peripheral spots is not uniform. This is related to the off-center location of the focus (compared to the center of the center spot). However, I have not had the time to model this correctly.

9.2.1. *Measuring R_C*

9.2.2. *Measuring Thoughput*

9.3. *Errors*

9.3.1. *Tilt of the Optic/Mask Assembly*

We want to determine what happens to the peripheral spot spacing if the optic/mask assembly is tilted with respect to the source, optic center, detector axis. Clearly,

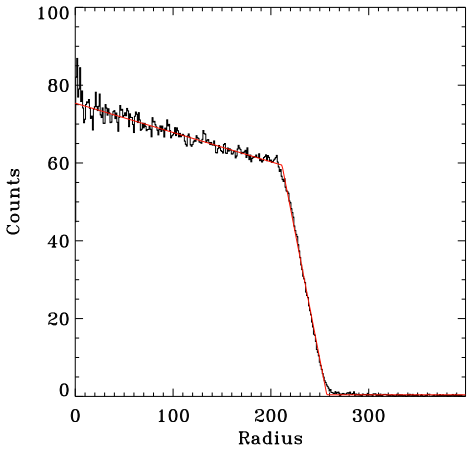

Figure 64. Black: The radial profile of the central spot. **Red:** A fit to that profile. The slope from the center to the break at $\sim$ 210 pixels is due to the structure of the non-, partially-, and fully-focused photons. The slope from the break to the background is due to the finite source size.

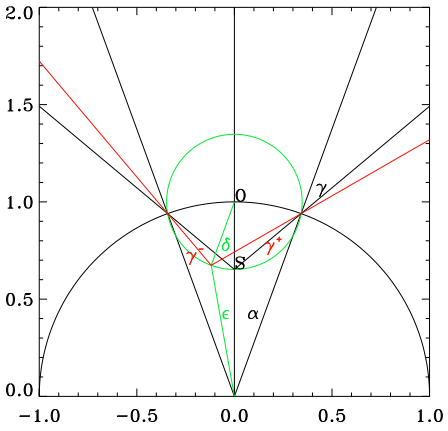

Figure 65. Geometric construction for determining the effect of the tilt of the optic/mask assembly. Here, instead of rotating the optic about its center point, we have rotated the location of the source about the same point.

a tilt will cause the spots will move across the face of the detector. What we are interested in here is the extent to which the movement is different for adjacent spots. The geometry is shown in Figure 66. Here, instead of tilting the optic, we have rotated the source position by an angle δ from the axis of the optic. We wish to determine the angles between a ray from the source and a pore at a fixed distance from the optical axis, γ^- and γ^+, in order to determine how the spots will move with respect to one another. From the geometric construction we see that the distance between the radius of curvature and the source, r' will be

$$r'^2 = R_c^2 + Z_S^2 - 2R_c Z_S \cos\delta \tag{83}$$

The angle ϵ can be seen to be

$$\epsilon = \arcsin\left(\frac{Z_S \sin\delta}{r'}\right). \tag{84}$$

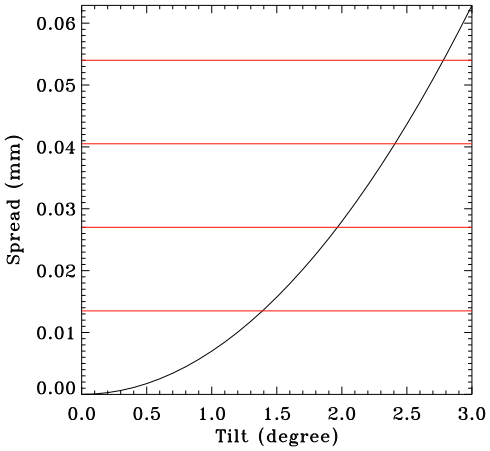

Figure 66. The amount of change of the distance between two (non-diagonal) spots as a function of the tilt in the optic/mask assembly. The red horizontal lines mark increments of a single pixel on the current CCD.

The distances from the source to the fixed spots on the optic are given by

$$L^2 = R_c^2 + r'^2 - 2R_c r' \cos(\alpha \pm \epsilon) \tag{85}$$

Thus, the angles of incidence, γ^- and γ^+ are given by

$$\gamma = \arcsin\left[\frac{\sin(\alpha \pm \epsilon) r'}{L}\right] \tag{86}$$

If γ (without superscipts) is the angle on incidence when the source is on the optical axis, then we are interested in comparing $\gamma^+ - \gamma$ with $\gamma - \gamma^-$, and it is the difference in those two angles that will move the spots with respect to one another. For the LEXI optic, assuming Z_S=300 mm, Figure 66 shows the change in spot distance as a function of the tilt angle.

9.3.2. *Horizontal Translation of the Mask with respect to the Optic*

Here it is assumed that, in one way or another, the center of the mask's center hole is not aligned with the optical axis. This misalignment could, for example, be due to an unrecognized bias in the optic. With the current mask, the central hole is large enough (radius = 1 mm) that a significant fraction of the light passing through the hole is actually reflected once in one or both dimensions; it is not a representative of unreflected emission only. If we displace the central hole from the optical axis, then the circle of unreflected light will move across the detector, but the location of the focussed light will not. Thus, the difference between the circle of unreflected light and the center of the focussed light contains the information required to determine the offset of the hole from the optical axis.

[And the rest of this section is a work in progress.]

9.3.3. *Vertical Translation of the Optic*

9.4. *Summary*

10. OPTICAL TESTING

It has long been suggested that, given the well known Photonis® demonstration showing a SMO focussing optical light, that one might be able to use optical light to characterize the quality of an individual SMO. N. Thomas (and M. Collier?) attempted to use lasers to test optics as part of the TAO project, and found that there were horrible problems. M. Galeazzi is currently finding the same thing. The bottom line is that even a coated SMO operates as a two-dimensional diffraction grating, and we now wonder if the Photonis® demonstration is misleading, as what is shown very well might be the diffraction pattern.

11. INSTRUMENT DESIGN CONSIDERATIONS

11.1. W/L

Although the current suppliers of SMOs provide rather limited options for W, L, and R_c, it is still worthwhile to explore how the effective area varies with W/L. Figure 67 shows the results of a set of simulations for STORM type optics with R_c=100 cm, R_o=20 cm, L=0.1 cm, and a fixed open fraction of 0.6. (This last assumption seems to match Photonis products, and it makes sense for optics that are drawn from the same block but with different stretches.)

Increasing the W while keeping L fixed increases the angle for which rays can pass through the optic undeviated, Γ_0, as well as increasing all the other Γ_n. This will certainly increase the total throughput or effective area, as in shown in the left panel of Figure 67. Changing the coating, for the most part, just scales the entire curve, though by different factors at different energies. Note the curves are less steep than Γ_0^2 due to the reflectivity decreasing with higher incidence angles.

Increasing the throughput provides more counts, but that need not be a good thing if the contrast is reduced. The middle panel of Figure 67 shows the contrast, the flux in the core compared to the total flux, as a function of W/L. The effect of the reflectivity as a function of energy and incidence angle is apparent, and different coatings can show rather different curves. Similarly, the plot the flux in the arms compared to the total flux shows a dependence upon the coating of the optic.

From the plot of the contrast as a function of W/L it is clear that the optimal W/L depends upon the coating of the optic and the energy range of importance. It is clear that for Ni, W/L=0.02 is more favored for typical soft applications, while for Ir, W/L=0.04 might be better. Typically, the W/L available (at least from Photonis) are 0.02 and 0.04, which are both within the useful range.

Interesting, as increasing the W/L increases the effective acceptance area (compared to a fixed facet size), devices with larger W/L have stronger vignetting than devices with smaller W/L. The converse statement is that devices with smaller W/L have a flatter vignetting function. This is important for the region for which the throughput is $\gtrsim$80% of the on-axis throughput; the W/L does not significantly change the off-axis angle at which the vignetting function is 50% of the on-axis value. (As noted above, the 50% vignetting angle is set by simple geometry, the maximum angle at which a ray can pass directly through a pore without reflection.) [Still need to produce the plots of vignetting as a function of W/L for a STORM type device.]

11.1.1. *Contrast: Point Sources vs. Diffuse Emission*

TBD

11.2. *Tiling Geometry*

See § **??**.

11.3. *Facet Size*

Tiling means that there must be support structures that obscure parts of the device, which reduces the effective area. It should be noted that even if the support structure did not obscure any of the optic by, for example supporting them only by their edges, spreading the facets apart (and blocking the area between the facets) also reduces the total throughput. However, considering the total throughput obscures some important issues.

In Figure **??** we demonstrated that the contribution of a ray to the focus depends upon the distance it falls from the optical axis. If we assume that the facets are butted, and that a 2 mm wide support runs under each seam, obscuring 1 mm of each side of each facet, then for the STORM optic the reduction in total throughput is 10.0% while the active optic area has been reduced 9.75%.

Even though SMOs are typically used to be wide-field imagers, it is useful to consider the way the support structure effects different parts of the FOV. For the STORM optic, the individual facets are 4 cm by 4 cm, which, for R_c=100 cm, means that the facet has a radius of 1.145 deg, which is roughly Γ_0, where the contribution to the focussed image is highest.

Consider the difference between placing the optical axis in the center of the facet (centered) and placing it at the crossing of the supports (crossed). If we consider just the throughput of the focussed core of two-reflection PSF, we find that the centered image has $\sim$ 20% lower throughput than the crossed image. In the crossed image, the obscuration removes primarily the low Γ rays, which are not strongly focussed, while the obscuration in the centered image falls right on the source of the greatest contribution to the focussed image. Conversely, considering just the throughput of the non-reflected component of the PSF, it is reduced in the crossed image by $\sim$ 20% compared to the centered image.

Reducing the focussed component compared to the unfocussed component increases the point source detection threshold and will make structures in the diffuse emission more difficult to detect. This lack of detectability will be periodic across the FOV. This reduction is bad, and the variation is problematic. However, this exploration may be the worst case scenario because of the scale of the obscuration.

For comparison, consider a STORM created with 8 cm by 8 cm facets and the same size supports. (Not currently feasible, but potentially possible in the future.) If we consider just the throughput of the focussed core of two-reflection PSF, we find that the centered image has $\sim$ 1% lower throughput than the crossed image. This is due to the fact that the obscuration falls outside the region contributing to the focussing. Conversely, the unfocussed throughput is $\sim$ 20% lower in the crossed image than in the centered one. Thus, the larger facets provide a more uniform throughput for the focussed light.

Since Γ_n is a function of W/L, for a given R_c we might adjust the pore width so that edge of a 4 cm by 4 cm facet falls at Γ_1 (a relative null for the contribution to the focussed light) rather than at Γ_0. This would require changing W from 20 μm to 10 μm, which would reduce the throughput significantly (see Figure 67). Conversely, increasing W to 40 μm places Γ_0 at 2.29°, the center of the adjacent facet. Depending upon the coating of the optic this might mean lack of contrast, or not.

This is clearly a topic that should be revisited, perhaps in partnership with Photonis.

11.4. *Facet Coating*

TBD

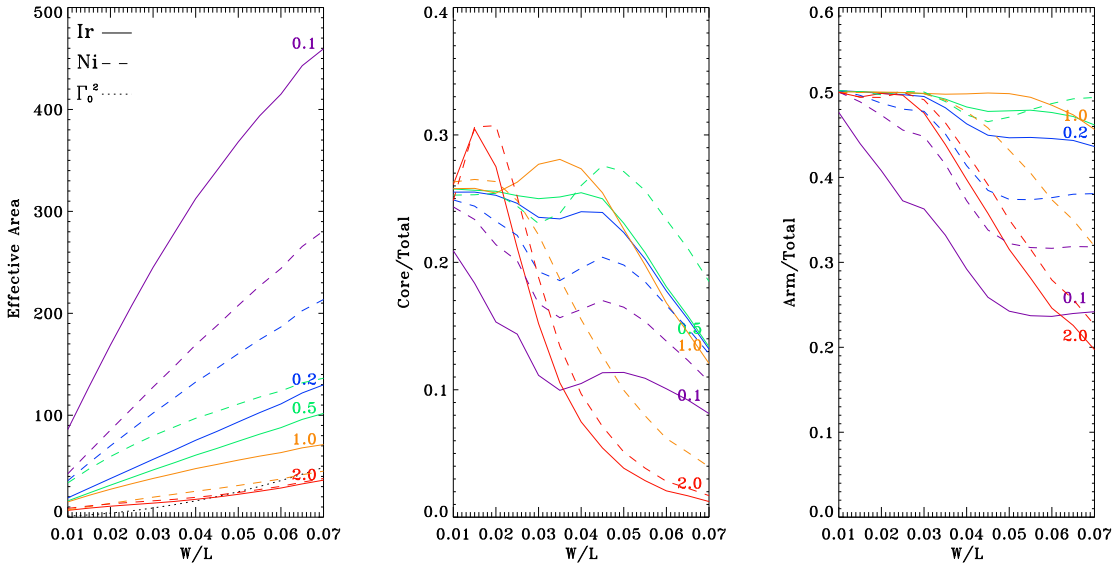

Figure 67. Total effective area and contrast as a function of W/L. All are shown as a function of photon energy in keV. All were calculated on-axis for an optic with R_c=100 cm, R_o=20 cm, L=0.1 cm, and a fixed open fraction of 0.6. *Left:* The effective area as a function of W/L. The solid lines are for an Ir coated optic, the dashed lines are for a Ni coated optic. The dotted line is a scaled plot of $\Gamma_0^2 = \arctan(W/L)^2$. *Middle:* The ratio of the flux in the core to the total flux. *Right:* The ratio of the flux in the arms to the total flux. [Since the behavior changes above 2 keV, I should extend this to higher energies.]

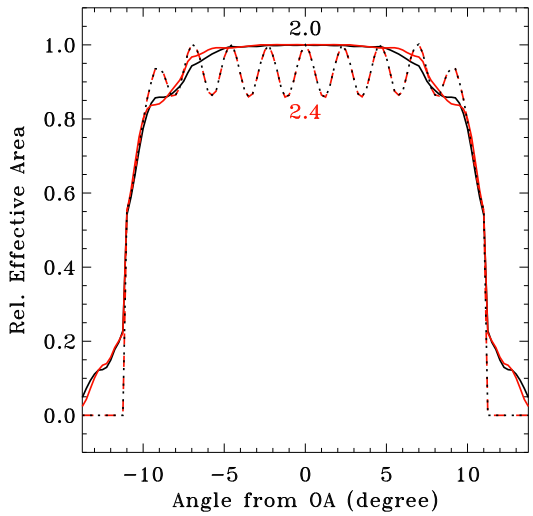

Figure 68. The vignetting functions for a non-STORM optic with W=40 μm and L of either 2.0 mm (black) or 2.4 mm (red). The solid lines are the vignetting for the total throughput. The dotted lines are the vignetting for just fully focussed photons. Note that all vignetting functions were normalized to unity on axis.

11.4.1. *Uncoated Optics*

The first problem confronting those seeking to simulate an uncoated optic is the composition of the glass. Since the glass composition is a proprietary recipe, we'll never know for sure. However, optical testing of LEXI at PANTER provides a certain amount of insight to this question.

Figure **??** shows the effective area curve determined for the LEXI optic (with optical blocking filters) at PANTER with the TRoPIC camera, which has a line spread function of ∼75 eV. The curve has been binned to 25 eV in order to improve the signal to noise. The absorption edges have been marked. We expect absorption edges from C (284.2 eV), N (407.9 eV), O (543.1 eV), and Al (72.95, 72.55, and 1559.6 eV) from the optical blocking filters, and at least O (543.1 eV) and Si (99.82, 149.7, and 1839 eV) from the bare glass. Other ingredients of the glass would create absorption edges at other energies. Willingale has suggested Pb (2484, 2586, 3066, and 3554 eV), K (297.3 and 3608 eV), Na (1070.8 eV), and Bi (2688 and 3177 eV). The same figure shows the simulated LEXI optic for SiO_2 and more complex glass (provided by Willingale) without blocking filters, with blocking filters, and with blocking filters smoothed by the TRoPIC line spread function.

The Si (1839 eV) edge, which is quite apparent in the sims, is detectable in the data mostly as a change in slope. The Pb edge (2484) ought to be detectable in the same way but does not appear in the data. Most of the other edges in the complex lead glass would not be visible in our data. Thus, as outlined in Kuntz et al (2022), we don't have a good simulation for a bare glass SMPO.

11.5. *Detector Placement*

11.6. *Modularization*

There are a number of wide-field missions that have considered building multiple small modules rather than a single large module. There are at least two situations in which this trade is of interest. The first is when one desires to cover a large area which need not be contiguous, such as for surveys. The second is when the modules are to be coaligned in order to get a greater effective area. In both cases we consider n modules of m by m facets with a set radius of curvature, where the radius of the one reflection effective acceptance area (Γ_1) is smaller than the radius of the optic. The number m is set by engineering constraints, usually the physical size of the dtector, and we wish to compare the performance of a larger number of smaller modules with a smaller number

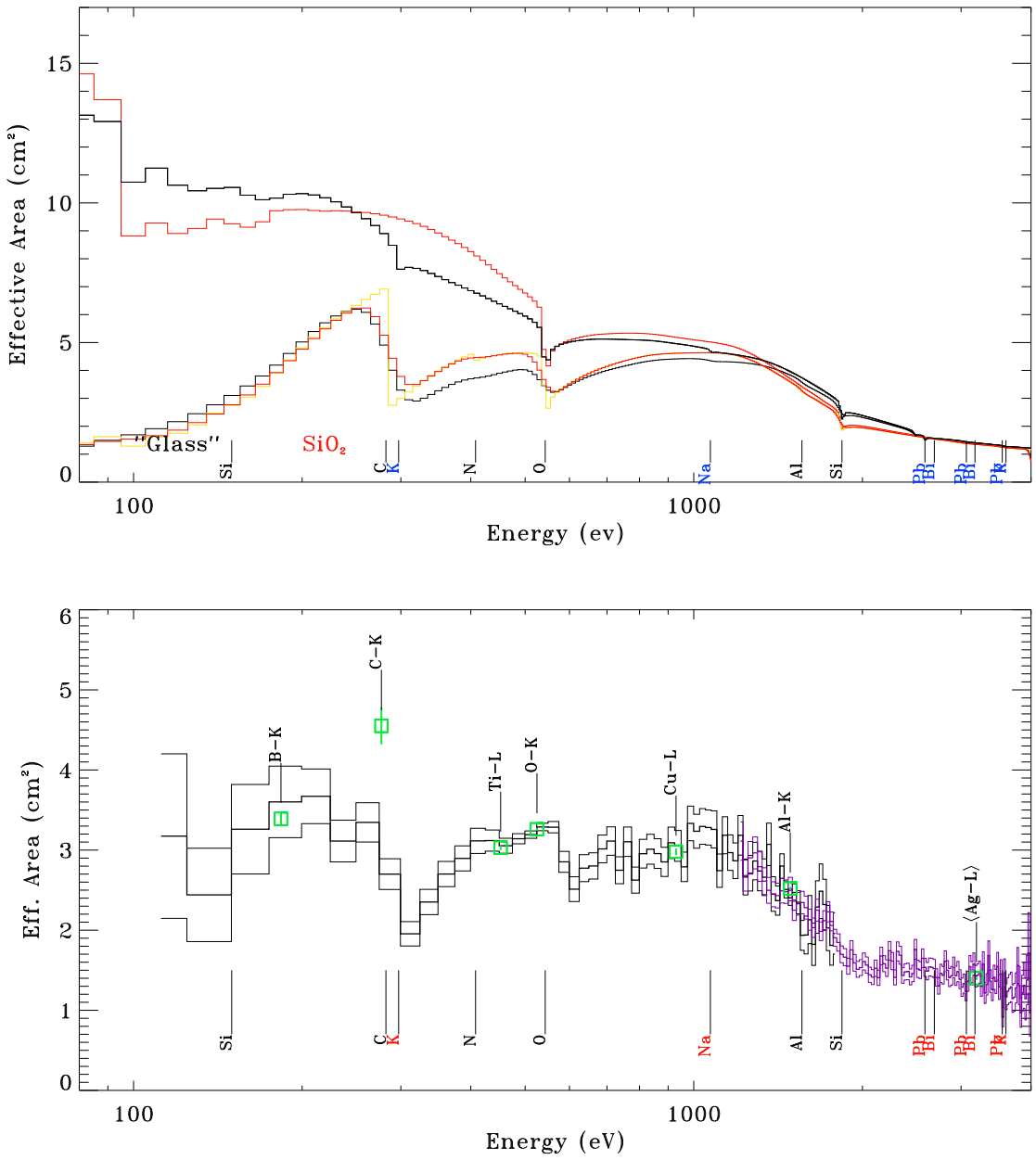

Figure 69. Top: Simulations for LEXI using SiO_2 (red) and a more complex lead glass (black). The higher pair of curves is without the optical blocking filter, while the lower pair of curves is with the optical blocking filter and smoothed to match the TRoPIC line spread function. Edges are marked. **Bottom:** The LEXI effective area curve on the optical axis.

of larger modules where, in both cases, the total number of facets is the same.

11.6.1. *Co-aligned Modules*

Here the consideration is primarily one of the FOV. However, it should be remembered that while n modules will cover the same area n times, it also incurs n times the instrumental background and n times the cosmic background. Thus, having n modules may not gain the S/N needed. However, since this depends upon the relative strengths of the emission and the instrumental noise, there is not much sense in exploring that in this more general setting.

11.6.2. *Non-aligned Modules*

We will compare the FOV and effective area of 3 by 3 array of 2×2 facet modules with that of a 2 by 2 array of 3×3 facet modules, and will determine the equivalent monolithic $m \times m$ facet instrument.

Before one can really address this problem, one must decide how uniform the FOV needs to be. One possible solution is to adjust the relative module pointings so that the 50% vignetting function of one module lies in the same direction as the 50% vignetting function of the next module. That way, at the module boundaries one should get the same number of counts as at the center (though with twice the instrumental noise). A second possible

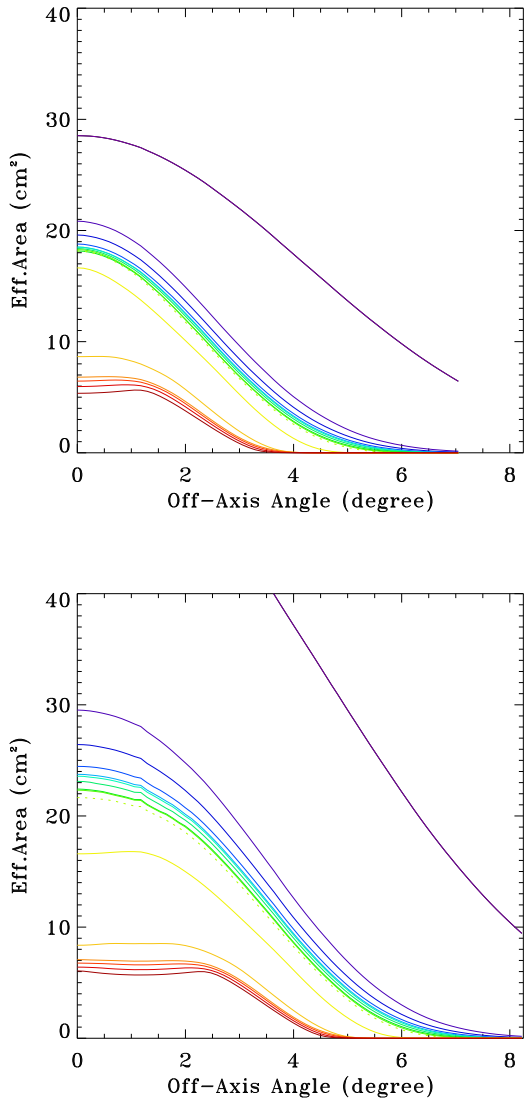

Figure 70. Top: Vignetting function for a 2×2 facet module. The energies are listed in Table 15 and run from low at the top to higher at the bottom. **Bottom:** Vignetting function for a 3×3 facet module. The energies are listed in Table 16 and run from low at the top to higher at the bottom.

solution is to adjust the relative module pointings so that the 90% vignetting function of one module lies in the same direction as the 90% vignetting function of the next module. This is probably closer than one would ever want the modules, but it serves as a useful *terminus ad quem*. Given how the vignetting function changes with energy, it is clear that the solution will depend upon the energy of interest. Tables 15 and 16 show the linear size of a 3 by 3 array of 2×2 facet modules with a 2 by 2 array of 3×3 facet modules for energies from 0.1 to 4 keV.

Compare the linear size of the FOV for the "total" vignetting function between Tables 15 and 16. It is clear that "butting" the modules at the 50% vignetting function produces a larger FOV for the 3 by 3 array of 2×2 facet modules. However, that advantage is greatest at lowe energies, it's a small advantage at 1 keV (14.′80 vs. 14.′09), and at higher energies the 2 by 2 array of 3×3 facet modules has a slight advantage. If, however, we are butting at the 90% vignetting function, the 2 by 2 array of 3×3 facets has the advantage for energies $\gtrsim 0.5$ keV. Thus, so long as the butting is at vignetting values $> 50\%$, the 3×3 facet modules have a slight advantage for energies $\gtrsim$1 keV.

Now, if we are concerned about point sources, we can "butt" the modules based on the vignetting function for just the fully focussed photons. [This is a crude thing to do, and it is not yet clear whether doing this correctly will get a different result.] In this case, butting at the 50% vignetting provides some advantage for 2×2 facet modules at lower energies. For higher values of the vignetting function, the 2×2 modules have the advantage.

The above comparison, however, is not fair, as the linear FOV size for 3 by 3 array of 2×2 modules is at a lower effective area than 2 by 2 array of 3×3 modules. So we have taken the peak effective area (measured from the entire PSF) for the 2×2 modules, determined the FOV at that effective area for a 3×3 module, and again calculated the linear FOV size. For a given effective area at the boundary between modules, the 3×3 facet modules usually have the larger FOV. At 2 keV the modules are relatively equivalent, but the 3×3 facet modules perform better at both lower and(!?!) higher energies.

11.6.3. *Point Sources*

We assume that each detector has a constant intrinsic noise level D and quantum efficiency Q. We assume a flat cosmic background of C photons/cm^2/s/arcmin^2. Upon this background, we wish to detect a point-like source with a flux of F photons/cm^2/s. To understand the detectability of such a source, we really need to simulate the image carefully, calculating the PSF at every pixel for a region that is as wide as the PSF at the location of the point source. This remains TBD. Presumably, this would allow us to determine, at least to some extent, the amount by which one does need to butt the modules.

Table 15
2×2 Modules

E	Core[a]				Total[b]			
	50% P.E.A.[c]		90% P.E.A.[c]		50% P.E.A.[c]		90% P.E.A.[c]	
keV	E.A.[d] (cm^2)	FOV[e] (°)	E.A. (cm^2)	FOV (°)	E.A. (cm^2)	FOV (°)	E.A. (cm^2)	FOV (°)
0.1	4.32	28.89	7.77	3.52	14.27	28.89	25.68	11.28
0.2	3.32	16.91	5.98	2.82	10.42	16.91	18.76	6.34
0.3	3.14	16.91	5.66	2.82	9.80	16.21	17.63	6.34
0.4	3.02	16.21	5.44	2.82	9.39	15.50	16.90	6.34
0.5	2.98	16.21	5.37	2.82	9.26	15.50	16.66	6.34
0.6	2.99	16.21	5.38	2.82	9.25	15.50	16.66	5.64
0.7	2.97	16.21	5.35	2.82	9.19	15.50	16.54	5.64
0.8	2.94	15.50	5.30	2.82	9.08	14.80	16.34	5.64
0.9	2.97	15.50	5.34	2.82	9.14	14.80	16.45	5.64
1.0	2.96	15.50	5.32	2.82	9.08	14.80	16.35	5.64
1.5	2.79	14.09	5.02	2.82	8.32	14.09	14.98	4.93
2.0	1.39	14.09	2.49	3.52	4.33	14.09	7.80	7.05
2.5	0.92	14.09	1.65	2.82	3.43	13.39	6.17	8.46
3.0	0.84	14.09	1.52	3.52	3.27	13.39	5.89	8.46
3.5	0.73	14.09	1.32	3.52	3.06	13.39	5.50	8.46
4.0	0.60	14.09	1.07	2.82	2.82	13.39	5.08	9.16

[a] For these calculations, we used the vignetting function for the fully focussed photons.
[b] For these calculations, we used the total vignetting function.
[c] Peak Effective Area.
[d] Effective Area at edge for this component of the PSF.
[e] Linear size of the FOV for a 3 by 3 array of 2 facet by 2 facet modules.

Table 16
3×3 Modules

E	Core[a]				Total[b]			
	50% P.E.A.[c]		90% P.E.A.[c]		50% P.E.A.[c]		90% P.E.A.[c]	
keV	E.A.[d] (cm^2)	FOV[e] (°)	E.A. (cm^2)	FOV (°)	E.A. (cm^2)	FOV (°)	E.A. (cm^2)	FOV (°)
0.1	6.64	18.32	11.95	6.11	27.81	20.67	50.05	7.99
0.2	3.44	15.03	6.19	6.11	14.76	14.56	26.57	6.11
0.3	3.09	15.03	5.56	6.11	13.21	14.09	23.78	6.11
0.4	2.87	15.03	5.17	6.11	12.23	14.09	22.01	6.11
0.5	2.79	15.03	5.03	6.11	11.87	14.09	21.37	6.11
0.6	2.77	15.03	4.99	6.11	11.79	14.09	21.22	6.11
0.7	2.72	14.56	4.90	5.64	11.56	14.09	20.80	6.11
0.8	2.64	14.56	4.76	5.64	11.21	14.09	20.18	6.58
0.9	2.63	14.56	4.74	5.64	11.16	14.09	20.09	6.58
1.0	2.56	14.56	4.61	6.11	10.82	14.09	19.48	6.58
1.5	2.23	14.09	4.01	6.58	8.40	14.09	15.11	7.52
2.0	1.09	14.09	1.96	7.05	4.26	14.09	7.67	9.40
2.5	0.74	14.09	1.33	6.58	3.54	13.62	6.37	9.87
3.0	0.68	14.09	1.22	6.58	3.38	13.62	6.09	10.34
3.5	0.60	14.09	1.08	6.58	3.20	13.62	5.76	10.34
4.0	0.50	14.09	0.91	6.58	3.03	13.62	5.45	10.34

[a] For these calculations, we used the vignetting function for the fully focussed photons.
[b] For these calculations, we used the total vignetting function.
[c] Peak Effective Area.
[d] Effective Area at edge for this component of the PSF.
[e] Linear size of the FOV for a 3 by 3 array of 2 facet by 2 facet modules.

Table 17
Comparison of Modules

Energy	50%P.E.A.[a]			90%P.E.A.[a]		
	2×2 (°)	3×3 (°)	$m \times m$ (facet)	2×2 (°)	3×3 (°)	$m \times m$ (facet)
0.1	28.89	28.97		11.28	22.05	
0.2	16.91	17.42		6.34	12.27	
0.3	16.21	16.72		6.34	11.62	
0.4	15.50	16.30		6.34	11.22	
0.5	15.50	16.12		6.34	11.03	
0.6	15.50	16.03		5.64	10.91	
0.7	15.50	15.88		5.64	10.72	
0.8	14.80	15.69		5.64	10.48	
0.9	14.80	15.59		5.64	10.32	
1.0	14.80	15.39		5.64	10.03	
1.5	14.09	14.22		4.93	8.02	
2.0	14.09	14.04		7.05	9.49	
2.5	13.39	14.17		8.46	10.66	
3.0	13.39	14.15		8.46	10.85	
3.5	13.39	14.15		8.46	11.10	
4.0	13.39	14.15		9.16	11.32	

[a] Peak Effective Area, measured for the entire PSF.

APPENDIX

The main text is ordered in a pedagogical way, starting from some simple principals and working towards complexity. The main text contains the mathematical derivations. The appendices, however, are arranged more in the order required for computation and may contain pseudocode.

A. FACET CENTERS

The first quantities that must be determined are the centers of each of the facets, assuming that the optic has n_x by n_y facets, each of which is F wide. It is assumed here that F includes more than the physical dimension of the glass facet, but also the minimum space between facets.

Constant-Longitude Packing: For the constant longitude packing, the most extreme line of latitude will be $\phi_{ext} = (n_y/2)F/R_c$. The longitudes of the centers of the facets is set by the closest possible packing on the rows furthest from the equator:

$$\phi_i = (i + 1/2 - n_x/2)F/R_c \cos(\phi_{ext}) = (i + (1 + n_x)/2)F/R_c \cos(\phi_{ext}) \tag{A1}$$

while the latitudes of the centers of the facets will be

$$\theta_j = (j - (1 + n_y)/2)F/R_c \tag{A2}$$

where the indices run from 0 to n. The (x, y) position of the center of the facet (i, j) will be

$$R_c \cos\theta_j \sin(\phi_i), R_c \sin(\theta_j) \tag{A3}$$

Close-Packed Packing: For each row i, the extreme latitude that sets the closeness of the packing will be $\phi_{ext} = iF/R_c$. Thus

$$\phi_i = (i + 1/2 - n_x/2)F/R_c \cos(iF/R_c) = (i + (1 + n_x)/2)F/R_c \cos(iF/R_c) \tag{A4}$$

while the latitudes of the centers of the facets will be

$$\theta_j = (j - (1 + n_y)/2)F/R_c. \tag{A5}$$

The (x, y) position of the center of the facet (i, j) is found from the longitudes and latitudes as for the constant-longitude packing.

B. REFLECTIVITY

From the LBL site (http://http://henke.lbl.gov/optical_constants/) one can get the index of refraction as a function of energy for many materials. The data is provided in the form of δ and β where the index of refraction,

$$n = (1 - \delta) - i\beta. \tag{B1}$$

Then, for the reflectivity one need only apply the Fresnel equations

$$R_s = \left| \frac{n_1 cos\theta_i - n_2 \left(1 - \left(\frac{n_1}{n_2} sin\theta_i\right)^2\right)^{\frac{1}{2}}}{n_1 cos\theta_i + n_2 \left(1 - \left(\frac{n_1}{n_2} sin\theta_i\right)^2\right)^{\frac{1}{2}}} \right|^2 \tag{B2}$$

and

$$R_p = \left| \frac{n_1 \left(1 - \left(\frac{n_1}{n_2} sin\theta_i\right)^2\right)^{\frac{1}{2}} - n_2 cos\theta_i}{n_1 \left(1 - \left(\frac{n_1}{n_2} sin\theta_i\right)^2\right)^{\frac{1}{2}} + n_2 cos\theta_i} \right|^2 \tag{B3}$$

where R_s is the reflectance for s-polarized light and R_p is the reflectance for p-polarized light. For unpolarized light

$$R = \frac{(R_s + R_p)}{2}. \tag{B4}$$

Animadversions on the optical constants for compound substances such as lead glass.

C. SURFACE ROUGHNESS

It should be noted that those constants are for perfectly smooth surfaces. There will be some surface roughness, but it is unclear how much. It is unclear how to implement surface roughness. Doing so requires real physical optics, and that study has simply not yet been done.

The roughness considered thus far has been implemented merely by relying on the henke.lbl.gov. That site implements a Nevot-Croce approximation.

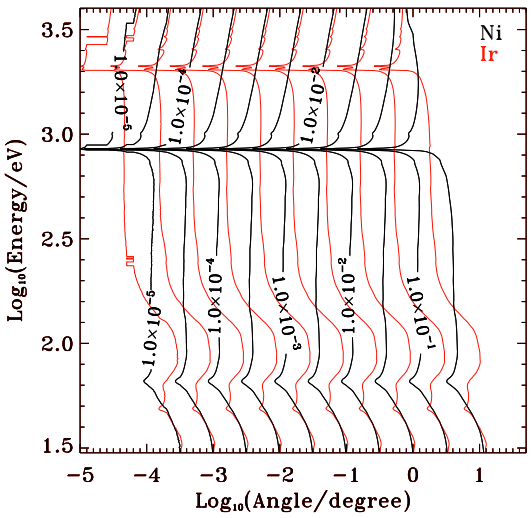

Figure 71. The reflectivity as a function of energy and angle of incidence. What is plotted is actually contours of 1-R. The black contours are for Ni and the red contours are for Ir.

D. PORE DEFORMATION

D.1. *Given Three Pore Corners, Find the Fourth*

We can calculate the effect of pore deformation simply, but only at scales rather larger than our pores. However, such a calculation demonstrates the functional form.

For a given pore, assume that we know the location of the pore corner closest to the optical axis (Q_{00}), and the length of the pore walls, d. Assume also that we know the location of the two adjacent corners: $\vec{Q_{01}}$=[x_{01},y_{01},z_{01}] and $\vec{Q_{10}}$=[x_{10},y_{10},z_{10}]. The task is to determine the location of the last corner, $\vec{Q}$=[x,y,z]. (Technically, this should be $\vec{Q_{11}}$, but we'll stick with $\vec{Q}$ to reduce the subscript confusion, at least for this subsection.) We have three equations to solve simultaneously:

$$(x - x_{01})^2 + (y - y_{01})^2 + (z - z_{01})^2 = c^2 \tag{D1}$$

$$(x - x_{10})^2 + (y - y_{10})^2 + (z - z_{10})^2 = c^2 \tag{D2}$$

$$x^2 + y^2 + z^2 = R_c^2 \tag{D3}$$

where

$$c = \sqrt{2R_c^2(1 - \cos(R_c/d))}. \tag{D4}$$

is just the length of the chord of the curve running from $\vec{Q_{01}}$ or $\vec{Q_{10}}$ to $\vec{Q}$. The first two equations are just setting the lengths from $\vec{Q_{01}}$ and $\vec{Q_{10}}$ to $\vec{Q}$ on the surface of the sphere, which we render as the length of the chords connecting $\vec{Q_{01}}$ or $\vec{Q_{10}}$ to $\vec{Q}$. The third equation is just the equation of the sphere.

If we take the first two equations and eliminate z, we obtain an equation for the plane that is equidistant from the two known corners:

$$y = \frac{\left((R_c^2 - c^2)(z_10 - z_01) + (x_0{1}^2 z_10 - x_1{0}^2 z_01) + (y_0{1}^2 z_10 - y_1{0}^2 z_01) + (z_0{1}^2 z_10 - z_1{0}^2 z_01)\right)}{2(y_01 z_10 - y_10 z_01)} - \frac{(x_01 z_10 - x_10 z_01)}{(y_01 z_10 - y_10 z_01)} x \tag{D5}$$

which can be summarized as $y = ax + b$. One can then substitute this expression for y into the last equation to solve for z in terms of x:

$$z = \sqrt{R_c^2 - b^2 - 2abx - (1 + a)x^2}. \tag{D6}$$

At this point one can use the expression of $z = f(x)$ and $y = f(x)$ and, substituting into either of the first two equations, solve for x:

$$(x - x_i)^2 + (ax + b - y_i)^2 + ((R^2 - b^2 - 2abx - (1 + a^2)x^2)^{\frac{1}{2}} - z_i)^2 = c^2 \tag{D7}$$

where i is either 01 or 10. This clearly does not solve in a trivial manner, so one can use a root-finder.

D.2. *Building a Mesh*

We can now calculate the node positions for a square mesh draped over a spherical surface. We will calculate this for a single quadrant. We can designate the location of each node as (n_x, n_y) where, for convenience, counting starts

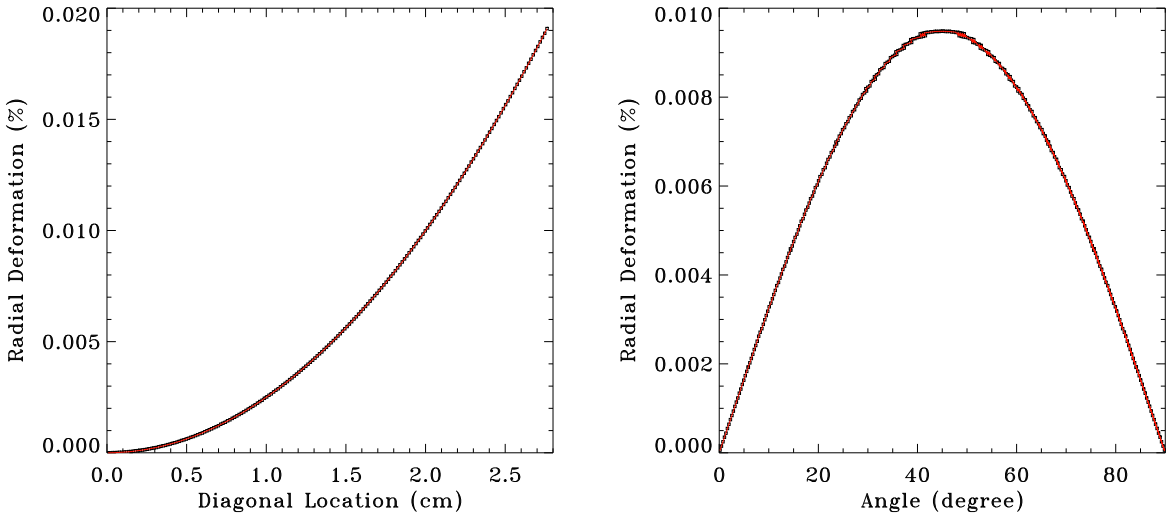

Figure 72. The functional form of the deformation as a function of location. In both plots the squares show deformation as the percentage change in the direction of the pore's more radial diagonal. *Left:* The squares show deformation as measured along the optic's diagonal. The red line is the function $1.5(1 - R_c \sin(D/R_c)/D)$. *Right:* The deformation as a function of azimuth along the maximal inscribed circle. The red line is a $\sin(2\phi)$ function scaled by $1.5(1 - R_c \sin(D/R_c)/D)$ for the appropriate D. Understanding the scaling factor of 1.5 remains a work in progress.

at 0. The node positions along the boundaries are given by

$$[R_c \cos(n_x d/R_c), 0, R_c \sin(n_x d/R_c)] \tag{D8}$$

along the $\hat{x}$ axis, with a similar expression along the $\hat{y}$ axis. We can then start calculating the coordinates of the remainder of the points starting with (n_x, n_y)=$(1, 1)$, which is calculated from the locations for $(0, 1)$ and $(1, 0)$. The calculation then proceeds to the next node for which a solution is possible which, incidentally, is always the unsolved node closest to the optical axis.

One can run the root-finder on for either i=0 or i=1. In practice the difference in solutions is quite small[20]. In implementing this, I take the average of the two solutions. In an attempt to impose the known symmetry upon the solution, I also calculate the solutions for both node (n_x, n_y) and node (n_y, n_x), average those solutions properly, and then apply that solution to both (n_x, n_y) and (n_y, n_x).

Clearly, such a solution can quite easily have cumulative precision problems which usually manifest themselves as imaginary returns from the root-finder. The prime nuisance is the quantity d/R_c. So long as that ratio is > 0.01, then one can calculate meshes of 401 by 401 (or greater, I haven't tried it yet) without imaginary roots.

D.3. *Results & Scaling Relations*

Using a calculation of a mesh with R_c=100 cm, d=0.0104, and max(n_x)=193, we can calculate the location of the nodes in the upper left quadrant of the mesh. This is the equivalent of grouping the pores by 16 (i.e., 4 by 4). We can characterize the deformation of a given pore by measuring the distance on the radial diagonal, between the corner closest to the optical axis and that furthest from the optical axis. That is, we want to measure the distance between $\vec{Q_{00}}$ and $\vec{Q_{11}}$. We will make the further simplification that we are only interested in the *chord* distance rather than the distance measured on the surface of the sphere. Figure 25 shows the variation of this distance as a function of location.

It should be kept in mind that if you take a square with its diagonals in the $\hat{x}$ and $\hat{y}$ directions, then compressing the square's diagonal in $\hat{x}$ by Δ, expands the square's diagonal in $\hat{y}$ by Δ. Thus, the change in the $\vec{Q_{00}}$ to $\vec{Q_{11}}$ distance is directly anti-correlated with the change in the $\vec{Q_{01}}$ to $\vec{Q_{10}}$ distance.

In the main text we attempted to motivate a $\sin(2\phi)$ dependence of the deformation, as well as the functional form of the radial dependence. The right-hand panel of Figure 72 shows the deformation as a function of angle around the optical axis for a radius of $\sim$ 2 cm. This plot shows that the deformation is indeed well described by the $\sin(2\phi)$ function. However, our back-of-the-envelope calculation of the amplitude is off by a significant amount. On the third hand, the function that should describe the amplitude of the deformation has the right functional form for the deformation as a function of radius, as can be seen in the left-hand panel of Figure 72. These two plots suggest that, with some more careful thought, we may be able to figure out the necessary fudge factors and their derivations.

[20] Using the "fx_root" routine in IDL® and running double precision, the typical difference between i=01 and i=10 is $< 10^{-9}$.

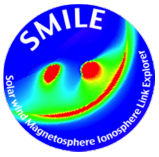

This work was developed under the aegis of the DXL, CuPID, LEXI, SMILE, STORM, LXT, and OWL-EYE missions, as well as NASA grant 0S00001220, X-Ray Micropore Optics Fabrication with Micro-3D Printing.

REFERENCES

Angel, J. R. P. 1979, ApJ, 233, 364
Chapman, H. N., Nugent, K. A., & Wilkins, S. W. 1991, Review of Scientific Instruments, 62, 1542
Chapman, H. N., Nugent, K. A., & Wilkins, S. W. 1993, Appl. Opt., 32, 6316
Hartline, B. K. 1980, Science, 207, 47
Hudec, R., Pina, L., Inneman, A., & Tichy, V. 2015, in EUV and X-ray Optics: Synergy between Laboratory and Space IV, ed. R. Hudec & L. Pina, Vol. 9510 (SPIE), 95100A
Land, M. F. 1978, Scientific American, 239, 126
Mutz, J.-L., Bonnet, O., Fairbend, R., Schyns, E., & Seguy, J. 2007, in Quantum Sensing and Nanophotonic Devices IV, ed. M. Razeghi & G. J. Brown, Vol. 6479 (SPIE), 64790F
Peele, A. G. 1999, Review of Scientific Instruments, 70, 1268
Priedhorsky, W. C., Peele, A. G., & Nugent, K. A. 1996, MNRAS, 279, 733
Schmidt, W. K. H. 1975, Nuclear Instruments and Methods, 127, 285
Schmidt, W. K. H. 1981, Space Sci. Rev., 30, 615
Vogt, K. 1975, Zeitschrift fur Naturforschung, 33c, 691
Willingale, R., et al. 2016, in Society of Photo-Optical Instrumentation Engineers (SPIE) Conference Series, Vol. 9905, Space Telescopes and Instrumentation 2016: Ultraviolet to Gamma Ray, ed. J.-W. A. den Herder, T. Takahashi, & M. Bautz, 99051Y

Contents